University of Alberta

Measurement and Analysis of Changes in Drop Size Distribution during Bitumen Clarification using Image Analysis

by

Shaun S. Leo

A thesis submitted to the Faculty of Graduate Studies and Research
in partial fulfillment of the requirements for the degree of

Master of Science in Chemical Engineering

Department of Chemical and Materials Engineering

Fall 2013
Edmonton, Alberta

Measurement and Analysis of Changes in Drop Size Distribution during Bitumen Clarification using Image Analysis

Abstract

The impact of mixing on demulsifier performance is studied using image analysis. Three experimental campaigns based on fractional factorial designs were performed in a CIST (Confined Impeller Stirred Tank), varying demulsifier bulk concentration (BC) and injection concentration (IC), mixing time (t_m) and mixing intensity (ε). The first campaign shows that BC and IC had significant effects on demulsifier performance and that t_m and ε were insignificant. The second campaign shows that mixing had a much more significant effect when the BC and IC are at the optimal values. The last campaign showed that good mixing is a solution for overdosing of a system.

Table of Contents

List of Tables

List of Figures

Nomenclature

H_{IMP}	Impeller height (m)
N_P	power number
V_{IMP}	impeller volume (m^3)
V_{TANK}	tank volume (m)
V_s	settling velocity (m/s)
X_{BC}	coded bulk concentration
X_{IC}	coded injection concentration
X_t	coded mixing time
X_ε	coded mixing intensity
X_J	mixing energy/mixing factor
d_p	droplet diameter (m)
g	gravity, (m/s^2)
s	standard deviation
n_i	number of drops in a size class i
C	off-bottom clearance (m)
D	impeller Diameter (m)
H	tank height, (m)
M	mass (kg)

N	shaft rotational speed, (s^{-1})
P	energy dissipation (W)
Q	volumetric flow rate (m^3/s)
Re	Reynolds' number
S	impeller submergence (m)
T	tank width, (m)
T	total number of pixels
t	time (s)
β	regression coefficient
ε	local energy dissipation rate (W/kg)
η	kolmogorov length scale (m)
μ	viscosity, (Pa*s)
ν	kinematic viscosity (m^2/s)
ρ	density, (kg/m^3)
ε_{IMP}	local maximum energy dissipation rate (W/kg)

Chapter 1: Optimization of the Diluted Bitumen Clarification Process

Canada possesses the world’s largest known oil sand. Oil sands formations are composed of mostly sand, clay, water and bitumen with trace amounts of salts and heavy metals. These formations date back to as far as the Devonian Period. Formation of oil sands starts when proteins and carbohydrates are broken down into kerogen (Masilyah, 2011). The kerogen decomposes to form liquid petroleum which then flows through the rocks and sands till it forms an oil reservoir. Bitumen is an unconventional form of petroleum which is upgraded into synthetic crude oil with comparable characteristics to the conventional crude oil obtained from oil wells.

This thesis looks at optimization of the diluted bitumen clarification process, which is one of the key steps in converting bitumen into usable energy, mainly focusing on the effects of mixing on the quality of product produced.

1.1 Extraction

Oil sands consist of mostly solids with ~6-15% bitumen and some water. These solids are sand, clays and fines. The water present in the Athabasca oil sands is what makes it processable. The water forms a thin film between the sand and the bitumen. This film facilitates the separation of the bitumen from the sand grains. Oil sand deposits can either be mined or extracted in situ. Mining operations are performed on relatively shallow oil sands formations while in situ recovery is used when the overburden covering the formation is too deep for mining to be economical.

1.1.1 Mining

Mining operations are performed on oil sands formations with an overburden thickness less than 75m (ERCB 2008). The truck-and-shovel method is used to mine the oil sands ores. The ores are then crushed into smaller particles and treated with hot water, forming slurry. This facilitates the liberation of the bitumen from the sand grains for future processing and also makes the oil sands transportable via hydro-transport. The slurry is then transported to an extraction plant where the bitumen is extracted from the slurry mixture.

1.1.2 In situ

In situ bitumen recovery is used when the overburden above the oil sands formations are too thick for mining operations. Steam Assisted Gravity Drainage (SAGD) is used to extract the bitumen in situ. In this process, two parallel horizontal wells are drilled into the lower part of the formation. Steam is injected into the formation through the upper well. This heats up surrounding oil sands and liberates the bitumen from the sand grains. The bitumen then flows down into the lower well, along with the condensed steam, which is then pumped to the surface where further processing occurs.

1.2 Bitumen Froth

During bitumen extraction from the oil sands, warm water is used to extract the bitumen from the oil sands. Bitumen gets attached to air bubbles present in the water. The air bubbles carrying the bitumen then rise to the top of a gravity settling vessel, forming a layer of bitumen froth. This layer of froth contains approximately 60% bitumen, 30% water and 10% solids by mass. The only desirable component amongst these three is the bitumen, which is to be enhanced during froth treatment. It is important to remove the water in the froth due to the corrosive nature of the chloride ions present in the water. These chloride ions would cause damage to the downstream upgrading equipment (Feng, 2009). The solids in the froth classified into two groups, sand and fines ($D_{fine} < 44$ μm). The majority of the sand settles out easily by gravity, leaving the fines behind which do not settle that easily due to their small size. Solids present in the froth are also undesirable as they cause fouling and catalyst poisoning. A bitumen upgrader requires a feed that contains less than 0.5 wt. % water and solids (Walker, 2008).

1.2.1 Froth Treatment

The main goal of froth treatment is to remove the unwanted solids and water present in the froth. De-watering of the froth by droplet sedimentation is based on Stokes Law of terminal settling velocity,

$$V_s = \frac{1}{18}\frac{(\rho_p - \rho_f)}{\mu} g d_p^2 \tag{1}$$

where V_s is the terminal settling velocity of the particle

ρ_p and ρ_f are the densities of the particle and the fluid media respectively

μ is the continuous fluid viscosity

g is gravity

and d_p is the diameter of the particle.

Two methods are currently applied in industry for commercial froth treatment, the naphtha-based treatment and the paraffinic treatment. Hot solvent would first be added to the bitumen froth to reduce the viscosity and density of the continuous phase. This allows for faster settling of the particles according to Stokes Law. The diluted bitumen is then allowed to settle on inclined plate settlers (IPS) or centrifuged, separating out the tailings.

1.2.1.1 Paraffinic Treatment

Paraffinic treatment uses a paraffinic solvent at solvent-to-bitumen ratio of 2 or higher. Two different types of asphaltenes also precipitate out during paraffinic treatment, increasing the oil losses to tailings as the asphaltenes would be separated out along with the solids. However, the water-soluble asphaltenes act as flocculants for the emulsified water and solids (Gu et al. 2002), allowing for easier separation of the unwanted solids and water. As paraffinic treatment operates above critical dilution, there is a rigid oil-water interface and the droplets flocculate, making it easier for tailings removal. As a result, the bitumen produced from paraffinic treatment is dry and clean. However, due to the large volumes of paraffinic solvent required (S/B wt. ratio >2), larger vessels are needed for the plant, increasing the cost of operation. Paraffinic solvents are also costlier compared to naphtha solvents, which is the other treatment method. This means that although paraffinic treatment produce higher quality products, its cost is also higher.

1.2.1.2 Naphtha-based-treatment

In a naphtha-based froth treatment operation, naphtha is added at a solvent-to-bitumen of ratio of 0.65-0.70 by weight (Masilyah et al, 2011). This treatment uses naphtha as a froth diluent and operates below critical dilution. As a result, emulsions are formed easily and this lowers the quality of the diluted bitumen. Naphthenic froth treatment usually reduces the water content from 30 wt. % to ~1.5 to 2.5 wt. % and 10 wt. % solids to ~0.4 to 0.8 wt. %. The remaining water and solids are kinetically stable and will not settle out. Water is present in the form of a stable water-in-oil emulsion. The stability of this emulsion is due to the formed interfacial film (Rosen, 2004), making it difficult for coalescence or flocculation of the water droplets to occur naturally. As a result, solvent dilution and the use of demulsifiers are required to break the emulsion and allow for the water to settle out.

As mentioned before, a bitumen upgrader requires a feed that contains less than 0.5 wt. % of water and solids. Another step is required to further prepare the diluted bitumen for upgrading. Diluted bitumen clarification is the process in which the remaining water and solids are removed down to a level whereby the diluted bitumen can be fed into a bitumen upgrader. This is done by breaking the stable emulsions with the aid of chemicals in order to induce settling.

1.3 Water in Oil Emulsions

A naphtha-based treatment was used to obtain the diluted bitumen in this study. During the process of bitumen extraction from the oil sand ores, surfactants and bi-wettable solids mixtures are produced. These stabilize the water-in-oil emulsion. This is due to the layer of inorganic-organic material that coats the surfaces of the emulsified water droplets, forming a steric barrier to coalescence.

Studies have been done on emulsion stability; Bancroft (1913) stated that the stability of the emulsion is affected by the nature of the adsorbed layer and interfacial properties such as surface tension and interfacial viscosity. The adsorption of a surfactant onto the dispersed drop surface also affects the emulsion stability.

Natural surfactants are present in the bitumen. A study by Bhardwaj and Hartland (1994) concluded that the natural surfactants present in the bitumen system slowly migrate to the surface of the dispersed water droplets. This means that the emulsion stability is dependent on the emulsion age. Fine solids also produce a stabilizing effect for water-in-oil emulsions in bitumen (Yeung et al.

1999). A later study done by Yan (2001) also concluded that fine solids of intermediate hydrophobicity produce stable water-in-oil emulsions. Gu (2002) concluded in his study that the formation of emulsions in the system is not due to the natural surface active species, but rather the water-insoluble asphaltenes which precipitate during the naphtha-based treatment.

The stability of the water-in-oil emulsions can be credited to the presence of a complex adsorbed layer at the surface of the dispersed water droplets which acts as a steric barrier. The solution to this is to destabilize the emulsion with the use of a chemical additive, also known as a demulsifier.

1.3.1 Demulsifiers

Demulsifiers, also known as emulsion breakers, are chemicals which promote flocculation or coalescence of droplets. This helps in the removal of emulsified objects such as the water-in-oil emulsion present in diluted bitumen. Different demulsifiers have different effects and each demulsifier is customized to address specific systems.

Demulsifiers are amphiphilic compounds which destabilize emulsions by altering the interfacial properties such as interfacial tension, mechanical strength as well as the thickness of the interfacial films (Feng et al. 2009). An example of how a demulsifier works would be by displacing the surfactants coating the surface of the emulsion drops. This would remove the steric barrier and destabilize the emulsion, allowing for coalescence or flocculation to occur upon droplet collisions.

1.3.2 Demulsifier Performance

Studies on demulsifier performance for water-in-oil emulsions have been widely performed. There are many factors which affect the demulsifier performance. One of the more obvious factors would be the demulsifier bulk concentration (Bhardwaj 1994). Bhardwaj and Hartland (1994) carried out their study with synthetic 1:1 water/oil emulsions in 600 mL beakers at 332 rpm. They observed that large mixing times are not necessary as droplet coalescence occurred in the first few minutes (< 5 minutes). It also showed that the coalescence rate is dependent on the demulsifier bulk concentration.

Temperature is also a factor in demulsifier performance. Long (2004) observed that operating at a higher temperature range of 50 – 120 ^{o}C produces larger aggregates and increased settling rates. Bhardwaj and Hartland (1994) also concluded that temperature was a factor in demulsifier performance.

Demulsifiers can either be oil-soluble or water-soluble and the solubility of the demulsifiers can be classified by their partition coefficient. A partition coefficient greater than unity indicates a water soluble demulsifier and a partition coefficient less than unity represents an oil soluble demulsifier. Kim and Wasan (1996) concluded in their study that a demulsifier with an intermediate level of partitioning is the most effective for the destabilization of a water-in-oil emulsion. The demulsifier type also determines whether it destabilizes the system and promotes coalescence or flocculation. Peña (2005) concluded that a combination of both coalescing and flocculating demulsifiers allows for a faster rate of water separation.

In addition to partitioning of the demulsifier, the molecular weight is also a factor in demulsifier performance. Bhardwaj and Hartland (1993) concluded that a higher molecular weight demulsifier performs better than a low molecular weight demulsifier. Low molecular weight demulsifiers were found to be completely ineffective in destabilizing an water-in-oil emulsion.

One of the objectives of this study is to study the effects of mixing on demulsifier performance by measuring the water droplet distributions of the system. Image analysis was chosen as an alternative to the Karl Fischer Titration, which measures the water wt. % in the system, as it provides a deeper understanding of not just the water content, but also the size and structure of the water droplets and their aggregates.

1.3.3 Water Droplet Dynamics

Emulsions are composed of two immiscible or partially miscible liquids, one being the continuous phase and the other being the dispersed phase. The water-in-oil emulsion present in the diluted bitumen is stabilized by surface forces. Surfactants stabilize the emulsions by providing a charge to the droplets or by forming a steric stabilization layer. Both of these prevent droplet-droplet interactions. The fines present may also act as a stabilizing agent due to their affinity to both liquids (i.e. hydrophobic and hydrophilic solids). As mentioned earlier, demulsifiers promote flocculation and/or coalescence of droplets. One of the factors that prevent the emulsified water droplets from settling is their small size. Flocculation and coalescence increases the effective size of the water droplets which makes it easier for the water droplets to settle. These two mechanisms assist in the separation of emulsified water from the bitumen and it is important to understand the water droplet dynamics during froth treatment in order to optimize demulsifier performance.

Particle and droplet coalescence and flocculation play an important role in industrial processes such as precipitation or for solid-liquid separation in water treatment. Together with breakup, coalescence and flocculation control the evolution of drop/particle size distributions in liquid-liquid or liquid-solid dispersions.

1.3.3.1 Coalescence

Droplet coalescence is the process whereby two droplets collide and combine to form a bigger droplet. It is generally assumed that only binary collisions would result in coalescence and collisions involving more than two drops can be ignored (Kusters 1996). Droplet coalescence consists of three steps. Figure 1 shows the coalescence process of two droplets.

(1) Collision of two droplets
(2) Film Drainage
(3) Film Breakage and coalescence of droplets.

In order for coalescence to occur, there has to be a collision of two droplets with sufficient energy to stay in contact. While the two droplets are in contact, there will be drainage on their interface film. When this film is drained to a critical thickness and breaks, the two droplets would coalesce and form a bigger drop.

Water droplets are stabilized by repulsive forces which arise from electrostatic and steric forces. Coalescence occurs when these forces are depressed and the Van der Waals forces become the dominant force, bringing the droplets together and allowing the particles to overcome the energy barrier for particle attachment.

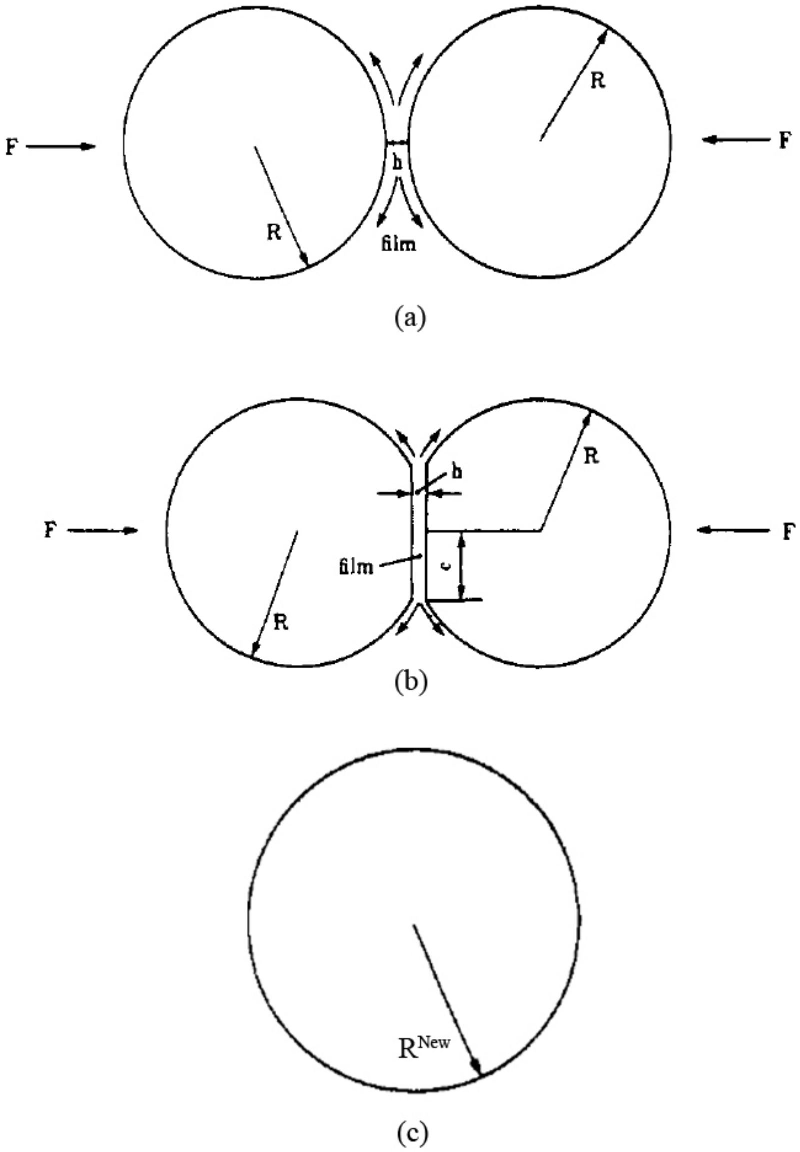

Figure 1: Droplet Coalescence Mechanism; (a) Droplet Collision; (b) Film Drainage; (c) Film Rupture and Coalescence (Edited from original image from Muralldhar 1986)

1.3.3.1 Flocculation

Flocculation is the process whereby particles adhere to one another after collision, forming an aggregate of particles/droplets called a floc. There are many aspects to a floc, such as floc size, floc strength (strength of adhesion between droplets/particles) and floc structure (closely packed, loosely packed, segregated etc). An improved understanding of flocculation behavior allows for better manipulation of floc properties so as to obtain desired product specifications.

Flocculation is a two-step process, with its first step similar to coalescence.

(1) Particles must be brought together by a transport mechanism
(2) Attractive or repulsive inter-particle forces determine whether the particles adhere or separate.

There are many different kinds of transport mechanisms which result in different collision velocities. There is Brownian motion, spatial velocity variations as well as a difference in particle inertias. Brownian motion is the key contributing transport mechanism for particles in the submicron length scale. As a particle grows larger than the length scale of the smallest eddies given by the Kolmogorov length scale, collisions due to Brownian motion are less important and turbulent forces take over. Figure 2 shows the flocculation mechanism of two droplets. Flocs grow primarily through the addition of single particles/droplets into an already existing floc rather than through the collision of flocs. This is represented by Everett (1988) with the following equation:

$$\begin{gathered} \mathrm{A} + \mathrm{A} = \mathrm{A}_2 \\ A_2 + \mathrm{A} = A_3 \\ \vdots \\ A_i + \mathrm{A} = A_{i+1} \end{gathered} \tag{2}$$

where A_i is a floc containing i number of particles/droplets

and A is a single particle/droplet.

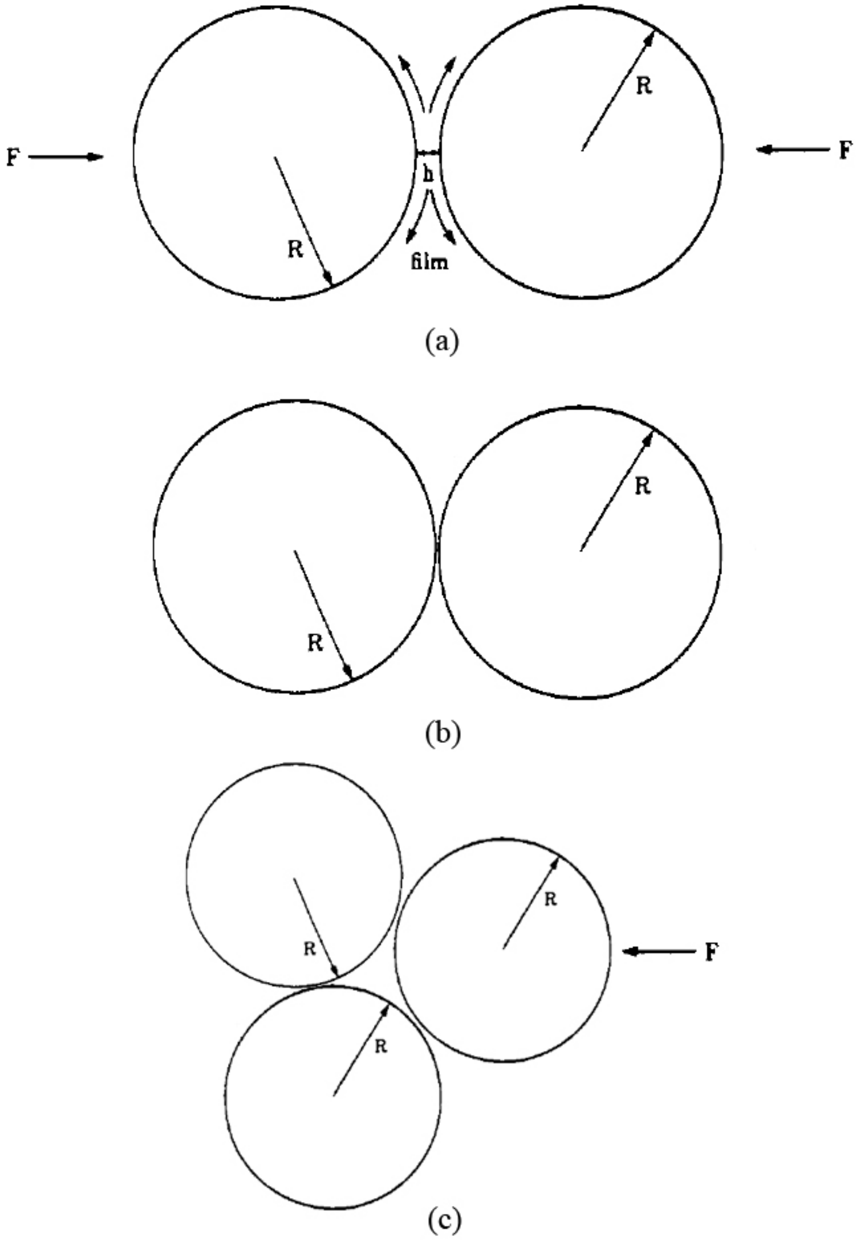

Figure 2: Droplet Flocculation Mechanism; (a) Collision of two droplets; (b) Adhesion of two droplets; (c) Collision and Adhesion of a single droplet with a doublet

1.4 Mixing

Mixing is a diverse field and the definition for fully mixed mixture varies from system to system. Mixing has a wide range of uses, from mixing of two miscible fluids to the destabilization of a stable emulsion. Many parameters have been used to define mixing. A recent review by Kukukova et al. (2009) classified mixing as a breakdown of three parameters, the intensity of segregation, scale of segregation and exposure of the dispersed phase. Figure 3 describes the three parameters.

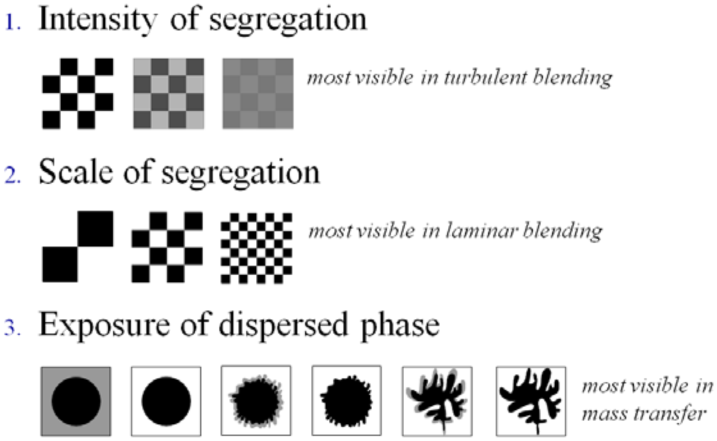

Figure 3: Mixing parameters as defined by Kukukova

Based on these definitions, the injection concentration of the demulsifier can easily be viewed as a mixing parameter. The more dilute the injection concentration, the more segregated the demulsifier is prior to entering the diluted bitumen system. In a sense, it can be viewed as the pre-mixing of the demulsifier. Based on that, it would be logical to assume that a more dilute demulsifier dosage would provide more exposure compared to a concentrated demulsifier dosage provided the overall bulk concentration is the same.

The energy consumption of an impeller is characterized by the power number (Paul et al. 2004) and as defined by the formula:

$$P = N_P \rho N^3 D^5 \tag{3}$$

where P is the shaft power consumed by the impeller (W)

N_P is the power number of an impeller

ρ is the density of the mixture (kg/m^3)

N is the shaft rotation speed (s^{-1})

and D is the impeller diameter (m)

The power numbers of commonly used impellers have been quantified by Paul et al. (2004) and vary based on the Reynolds number, which represents the level of turbulence in the system. The Reynolds number is represented by the following equation:

$$Re = \frac{\rho N D^2}{\mu} \tag{4}$$

where Re is the Reynolds' Number

and μ is viscosity of the fluid (Pa·s)

Laminar mixing occurs at Re < 10 and fully turbulent mixing occurs at Re > 20,000. In a fully turbulent flow regime, the bulk flow characteristics become independent of viscous forces.

Howarth (1967) developed a model for coalescence frequency based on impeller speeds. Impeller speeds affect the energy dissipation in the system as well as the size of the turbulence eddies. Droplets breakup if the shear force from the eddies are greater than the surface tension force on the drop surfaces. He stated that there was a stable drop size for each system which was dependent on the impeller speed. A decrease in impeller speed meant an increase in the maximum stable drop size as according to Kolmogorov's smallest eddie length scale given by:

$$\eta = \left(\frac{\upsilon^3}{\varepsilon}\right)^{1/4} \tag{5}$$

where η is the length scale of the eddie

υ is the kinematic viscosity of the continuous phase

and ε is the energy dissipation.

As a result, when a system in equilibrium has the mixing intensity (ε) decreased, the maximum stable drop size would increase. The results obtained from his experiments did support his theory as the maximum stable drop size is indeed correlated to the impeller speed. Howarth (1967) had three simplifying assumptions when he performed this study. He assumed that the turbulent field is homogeneous and isotropic, that drops grow by coalescence until they exceed the maximum stable drop size, after which drop break up occurs, and that the decay of turbulence in the system is instantaneous after the impellers speed is decreased. It was observed that the coalescence frequency was dependent on the impeller speed raised to the power of 1.3 – 1.65.

At the Kolmogorov length scale, the viscous forces in the eddy are equal to the inertial forces due to turbulent velocity fluctuations (Paul et. al, 2004). The energy dissipations (ε) of some commonly used impellers have been quantified by Zhou and Kresta (1996). For all other impellers, it is possible to obtain an estimate of the energy dissipation with the assumption that all energy will be dissipated into the impeller volume, resulting in the equation:

$$\varepsilon_{IMP} \sim \frac{P}{\rho V_{IMP}} = \frac{N_P N^3 D^3}{H_{IMP}} \tag{6}$$

where ε_{IMP} is maximum energy dissipation

V_{IMP} is the impeller volume

and H_{IMP} is the impeller height.

1.4.1 Effect of Mixing on Water Droplet Dynamics

The early stages of drainage-coalescence depend on three factors.

1. Magnitude of collision energy and frequency of collisions (from mixing)
2. Droplet-droplet interaction potential (surface forces)
3. Hydrodynamics of drainage of inter-droplet film

Studies on droplet coalescence have been done on a macroscopic scale, looking mostly into the first factor, magnitude of collision energy. However, the second and third factors affecting droplet coalescence occur on a much smaller scale and attempting to model it in a macroscopic scale results in some irregularities present only in the macroscopic scale. Even if the collision energy was at an optimal value, if the droplet-droplet interaction potential is high due to steric stabilization, the droplets would not coalesce. This would result in a stable emulsion.

Flocculation is similar to coalescence in that they are both coagulation processes. There are some similarities between them too as their efficiencies are both affected by the shear rate and turbulence eddies in the system. The factors that determine flocculation efficiency are similar to those for coalescence. The determining factors as to whether a droplet collision would lead to flocculation or coalescence is dependent on the particle-particle interaction forces, viscosity and collision time.

The presence of demulsifiers removes the steric layer surrounding the water droplets, allowing for easier droplet coagulation. By studying the water droplet dynamics during the diluted bitumen clarification process, a relationship between mixing effects and demulsifier performance can be established.

Not only does mixing affect the water droplet dynamics, but also the dispersion of the demulsifier. The demulsifier dispersion plays a role in the water droplet dynamics as well. Mixing is an important factor in process of bitumen de-watering as it affects the dispersion of the demulsifier as well as the coalescence and flocculation frequency of the water droplets.

1.5 Current Analysis Techniques for Drop Size Distributions

There are many analysis techniques being used to study the drop size distribution in multi-phase systems. A common analysis technique is microscopy. Bhardwaj (1994) studied the kinetics of water droplet coalescence in water-in-oil emulsions using microscopy. Mason (1995) studied petroleum emulsion separation using microscopy as well as a radiation scanning technique. Zhang (2003) characterized the Langmuir and Langmuir-Blodgett films of mixed asphaltenes and demulsifiers with the use of Atomic Force Microscopy. Liao (2004) studied the droplet interactions in the presence of a surfactant with high-speed imaging. Feng (2009) studied the demulsification of water-in-bitumen emulsions using microscopy. It can be seen that microscopy is still being used even though new technologies have allowed for different measurement techniques such as the use of lasers.

Zhou (1998) studied the effects of different impellers on drop size distributions for liquid-liquid dispersions using a phase Doppler particle analyzer. Desnoyer (2003) analyzed the drop size distributions in high phase ratio liquid-liquid dispersions with a laser granulometer. Boxall (2011) studied water droplet dynamics for water-in-oil emulsions using a particle microscope probe and a focused beam reflectance probe in-situ.

As mentioned before, many analysis techniques rely on microscopy, however, there is no image analysis software that would allow for the detection of water droplets in a complex multi-phase system such as diluted bitumen. Some studies present data obtained from those images but did not provide the methodology in which the data were extracted from the micrographs.

Kruis (1994) characterized agglomerated and aggregated aerosol particles using image analysis. He broke this procedure down into four steps, image acquisition, preprocessing, segmentation and feature extraction. Image acquisition was performed using a TEM and processed by the computer into a two-dimensional array of gray values. The image is then corrected for any defects, such as lack of sharpness, exposure imbalances, etc. After the image is preprocessed, a segmentation method would be implemented to separate particles that may be attached to one another. This is done through an erosion and dilation method where a layer of pixel is removed which allows the computer to recognize the touching particles as two separate particles.

The majority of droplet detection image analysis algorithms follow these first three steps, with minor differences along the way. However, for the feature extraction step, many different authors use different techniques. Tohno and Takashi (1988) identified the arcs on the outer contour of a circle by making use of the abrupt change of curvature on the outer contour. Hasegawa (1990) identified small particles through the Walsh power spectrum in which high frequency components corresponded to small particle sizes. This allows for a particle size distribution, but does not provide the individual particle data. Another common method used would be the Hough Transform, which uses an accumulator array to represent all pixels on the image. For each pixel, it identifies the elements that correspond to a shape that goes through the point. The shape detected depends on the variation of the Hough Transform that is being used (Ballard et al. 1982).

The image analysis algorithms discussed so far in this section were all used for simple two-phase systems and would not work for a diluted bitumen system. One of the objectives of this study is to develop a robust image analysis algorithm capable of extracting data from micrographs of the diluted bitumen system. An automated batch processing capability would be desirable due to the large quantity of data that has to be analyzed.

Chapter 2: Water Droplet Detection Image Analysis Algorithm

Manual measurement of water droplet sizes is subject to human error which cannot be properly accounted for as the degree and type of error is operator dependent. A systematic standardized image analysis protocol would eliminate the potential of human errors and ensures that any possible errors are random without subjective bias, as well as reducing processing time.

Two image analysis protocols were studied in this report. While both image analysis protocols had unique strengths, they were incomplete as a whole. A new Water Droplet Detection Image Analysis Protocol was developed with these two protocols in mind, with the idea of extracting the individual strengths of the protocols and combining them together to obtain a new protocol which has the strengths of both protocols while retaining none of their weaknesses. This new protocol was then further optimized to allow for batch processing of images as well as reduced operation time. The final protocol has a droplet count detection accuracy of 93.2%, droplet size measurement accuracy of 95.1%, and an average processing time of 5.5 seconds per image.

2.1 Introduction

Image analysis is a powerful tool that is being used in multiple fields of study to analyze multiphase systems, such as behavior of water droplets as they coalesce. Many computational programs have been developed over the years in attempts to fully harness the potential of image analysis. However, there are many different algorithms which differ from one another and there has been a lack of experimental data on real industrial systems. This limits the use of image analysis in industrial settings. In this study, a novel image analysis protocol for the analysis of a diluted bitumen system (provided by Syncrude Canada Limited) during the bitumen clarification process was developed.

There are three critical steps required when extracting data from a system using image analysis. The first step is obtaining the image, which in this study was done via microscopy. The second step involves the use of a protocol to process the image to optimize the data. The last step is to extract the necessary information from the image. This report discusses how the images were obtained from the diluted bitumen samples and the development of the image analysis protocol.

2.1.1 Microscopy

In order to obtain accurate results from image analysis, it is important to be able to obtain high quality micrographs. Image quality is dependent on many factors, such as the brightness levels and color values of the image. When an image is compressed, part of this information is lost and as a result, image quality is reduced. A high quality image allows for more accurate analysis as the image analysis algorithm extracts the data from individual pixels in the image. A high quality image has a high resolution which translates to having more pixels in the image, hence reducing the possible loss of data.

In this study, a Zeiss Axio Scope A1 Light Transmission Microscope was used along with a Zeiss Axio Cam ICc 1 (1.4-megapixel CCD camera) attachment. In order to obtain a “perfect” micrograph, it is important that the microscope gets calibrated before every run. Light, exposure, lenses and filter settings for the microscope and the exposure settings for the Axio Cam are all set at the optimal values. The required exposure settings on the microscope differ for each of the lenses on the microscope and can be adjusted. This is extremely important as the microscope is sensitive to the exposure settings and that determines the quality of micrographs taken. At 100 and 400 times magnification, it was much easier to obtain a good quality micrograph and the focus does not have to be adjusted constantly when taking micrographs at different locations on the microscope slide. At 1000 times magnification, the microscope becomes really sensitive to the focus and the focal range reduces significantly. Finding the right focus in order to display an image on the screen was a time-consuming process and additional effort was required to obtain the correct focus for a sharp image. It was also observed that there were multiple layers present on the microscope slides and this overlap presented some difficulties when trying to obtain data from the micrographs. As a result, micrographs were taken at both 100 times magnification with a pixel to micron ratio of 0.4557 µm/pixel and at 400 times magnification with a pixel to micron ratio of 0.1157 µm/pixel. Micrographs were taken at 30 random locations per microscope slide at each magnification in order to accurately represent the system. This covered approximately 80% of the sample surface on the microscope slide.

2.2 Image Analysis

Presently, there are many algorithms out there claiming to be able to perform population balances on multi-phase systems. Most of these image analysis algorithms are applied to simple two-phase systems (i.e. water in oil emulsions). The images obtained from those systems are relatively simple and as a result, image analysis algorithms are able to extract data from them. However, the diluted bitumen system (a real industrial system) that is being examined in this study is of a much higher complexity. There are multiple types of solids of different shapes and sizes as well as two different types of liquids, along with occasional air bubbles. Hence, a robust image analysis algorithm that takes into account the possible variations in each sample is required.

In this study, the efficiencies of several image analysis protocols for analyzing diluted bitumen systems were studied. Two promising image analysis algorithms were identified and their results compared. A final image analysis protocol was then developed based on the two different protocols, optimizing the desirable parts of both protocols and improving the undesirable parts. This resulted in a new image analysis protocol for complex multiphase diluted bitumen systems which was used to study the effects of mixing on additive performance (Chapter 4). An overview of the two methods is presented first, followed by a more detailed description of each step in the process.

2.2.1 Fovea Pro 4.0 Image Analysis Protocol

Initially, Fovea Pro 4.0, which is a series of filter add-ons developed by Reindeer Graphics for Adobe Photoshop, was the image analysis algorithm of choice. Some preliminary analysis on the diluted bitumen micrographs was attempted with unsatisfactory results.

Figure 4 shows the step by step procedure using Fovea Pro 4.0's capabilities. The code has promising pre-processing capabilities. The processing time for each image ranges from 1 to 2 seconds per image and is usually negligible. The pre-processing capabilities in Fovea Pro 4.0 are desirable as it allows for the removal of noise and some artifacts present in the micrograph while maintaining the information on the water droplets. It also corrects for any exposure issues that may be present and standardizes all micrographs. Figure 4 (b)-(e) shows the pre-processing steps.

The tool that Fovea Pro 4.0 had for drop size measurement was a filter called "Features Detection". However, the results obtained do not explain what “features” were detected were and the results obtained were insignificant. Figure 4(f) shows the Features Detection step.

The Fovea Pro 4.0 Image Analysis Protocol has strong capabilities in image standardization but lacks the critical ability to extract useful data from the image.

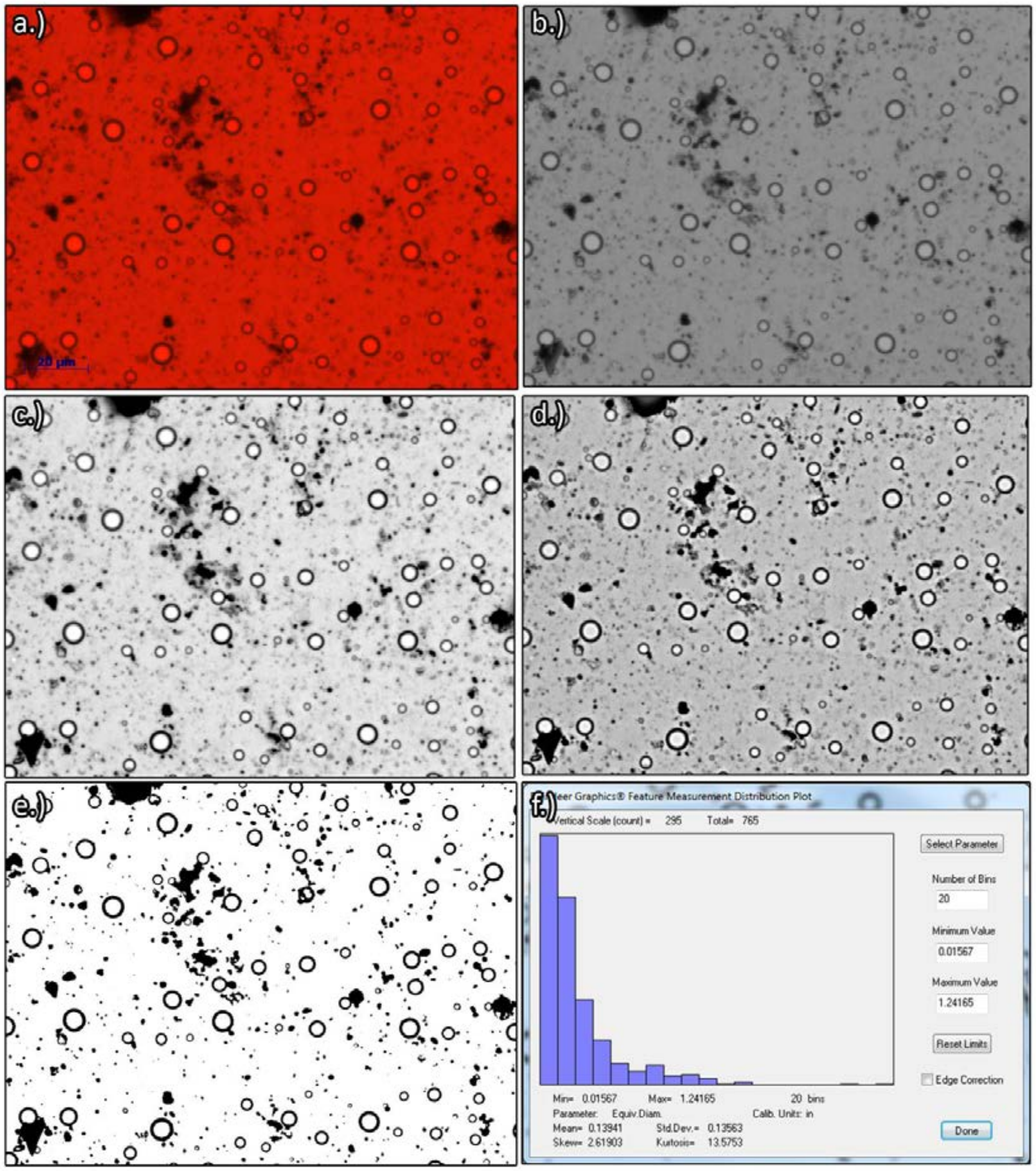

```
eer Graphics® Feature Measurement Distribution Plot
Vertical Scale (count) =    295      Total=   765

Min=  0.01567        Max=  1.24165                 20  bins
Parameter:    Equiv.Diam.                     Calib. Units: in
Mean=  0.13941       Std.Dev.=   0.13563
Skew=  2.61903       Kurtosis=    13.5753
```

Number of Bins: 20

Minimum Value: 0.01567

Maximum Value: 1.24165

☐ Edge Correction

Figure 4: Overview of Fovea Pro 4.0 Image Analysis Protocol. (a)-(e) Pre-processing; (e)-(f) Features Detection

2.2.2 Purwar’s Hough Circle Detection Protocol

As mentioned earlier, an image analysis algorithm that possesses the ability to extract water droplet sizes in the diluted bitumen system was required. Purwar’s (2011) work was in image analysis for the detection of malaria cells in red blood cells. His image analysis algorithm is based on the Hough Circle detection algorithm and comprises the pre-processing step as well as the critical function to extract the physical data on red blood cells based on their shapes.

Seeing that red blood cells and water droplets share similar geometrical shapes (circles in a 2-Dimensional image), the possibility of using the Hough Circle Detection image analysis algorithm was discussed and subsequently tested. This algorithm works based on circle detection (more in-depth explanation to follow in the later sections of this chapter).

Figure 5 shows the step by step procedure of this protocol. The starting image in Figure 5(a) is identical to that in Figure 4(a), however steps (b) – (e) in this protocol differ from those in Figure 4. It can be seen that this protocol is unable to accurately pre-process the micrographs of diluted bitumen due to the complexity of the system. The biggest flaw of this program would be from step (d) to (e), where the gray-scale image is converted to a binary image. This results in an extremely inaccurate circle detection step, step (f). Another unsatisfactory part of this algorithm was the processing time and intensity. It takes approximately a minute to process each image (Intel® Core™ i7-2600K CPU @ 3.40 Ghz with 16.0 GB DDR3 RAM, Windows 7 Enterprise 64-Bit OS). This causes some hardware restrictions when it comes to using the algorithm. It also lacked the capability to process images in batches and the algorithm would have to be run for each individual image. It should be noted that this program was not developed to work for diluted bitumen systems but rather on red blood cell micrographs, where it performs excellently.

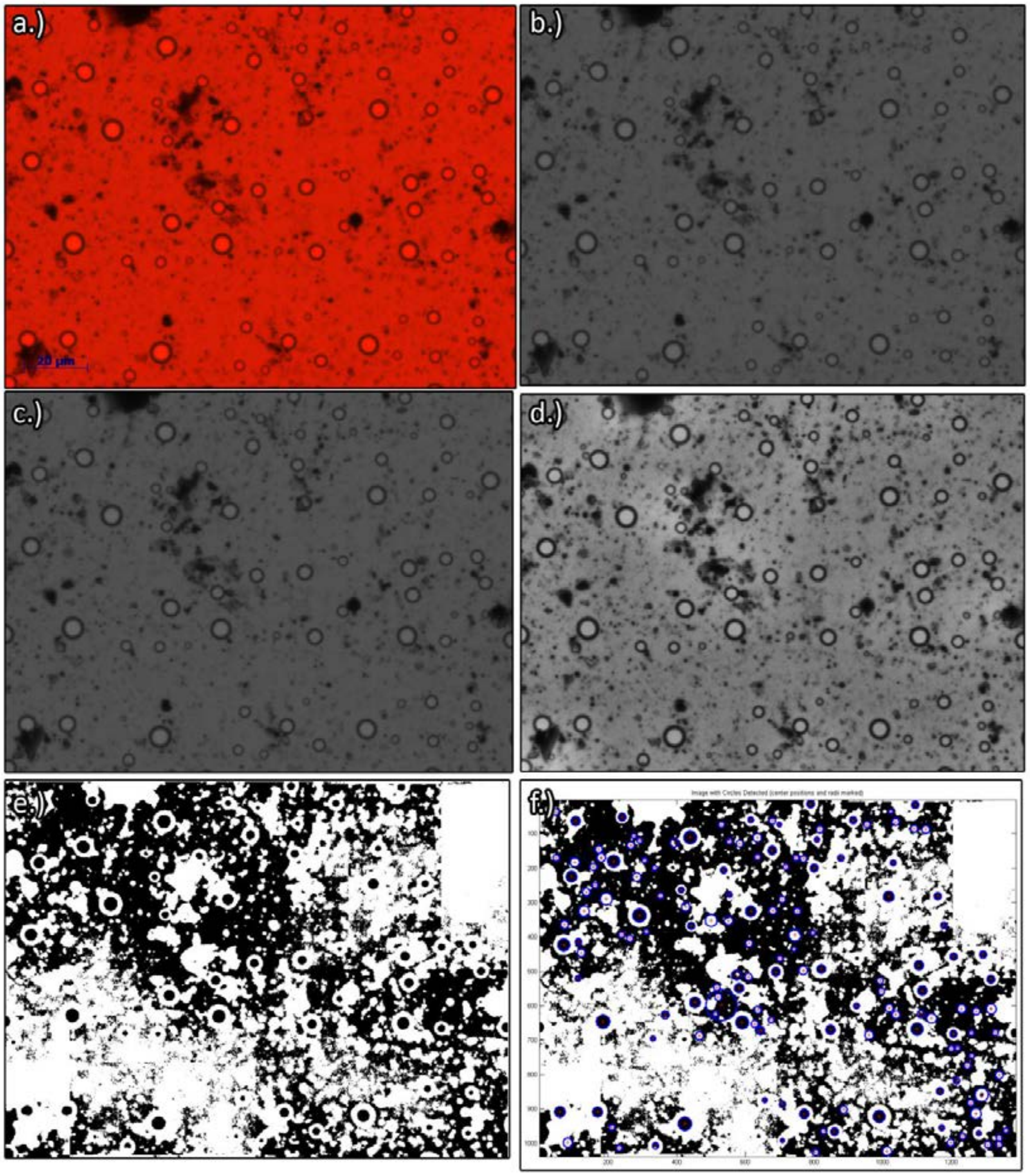

Figure 5: Overview of Hough Circle Detection Image Analysis Protocol. (b)-(e) Pre-processing; (e)-(f) Circle Detection

After testing and comparing the two different image analysis protocols, it was observed that both algorithms happened to be lacking in some areas in which the other algorithm excelled. The Hough Circle Detection image analysis algorithm was extracted and used after pre-processing the images using Fovea Pro 4.0. This resulted in a new image analysis protocol for diluted bitumen systems, which is the highlight of this chapter. This image analysis protocol was then optimized to lower processing time, increased detection accuracy, and to incorporate the capability for batch processing.

2.2.3 Water Droplet Detection Image Analysis Protocol

Figure 6 shows the step by step procedure for the final image analysis protocol that was developed at the end of this study. This protocol has two steps, the pre-processing stage, which prepares the image for analysis, and the analysis stage, where the circle detection algorithm is used to extract the population balance data from the image. The pre-processing stage is broken up into four steps and the analysis stage consists of one step.

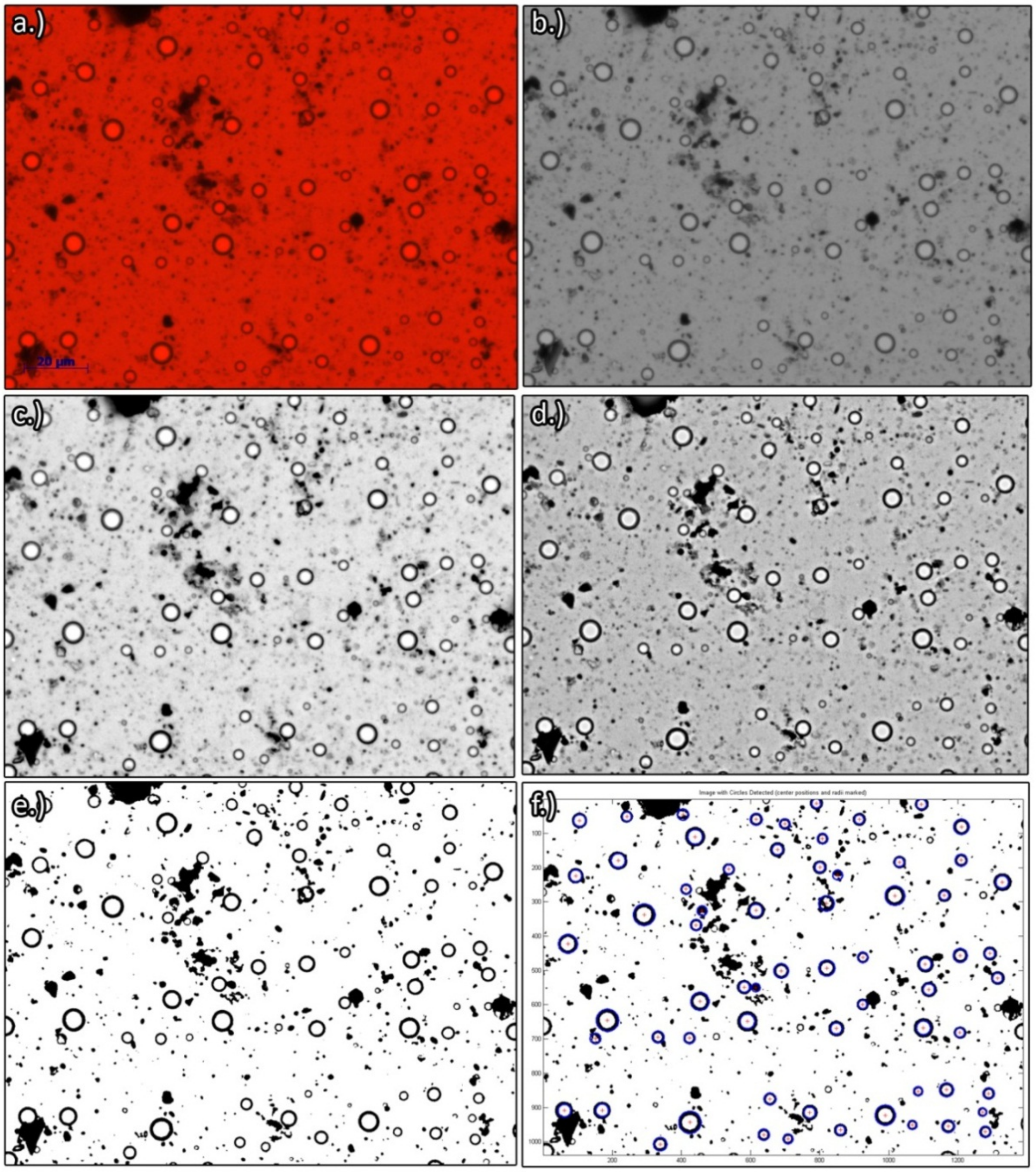

Figure 6: Overview of Water Droplet Detection Image Analysis Protocol. (a)-(e) Pre-processing; (f) Hough Circle Detection

2.2.3.1 Pre-processing

The purpose of the pre-processing stage is to prepare the image for analysis in order to obtain clear and accurate data. Pre-processing the image “cleans” the image by removing noise from the image. This pre-processing stage also fixes exposure issues that may be present on a poor sample, preserving the data. The most important effect of pre-processing the images is the standardization of the images. This allows for the image analysis algorithm to be run in automated batch processes without the need for an operator to manually adjust the parameters in the algorithm for each individual image. The four steps required for this process are as follows (*for more detailed descriptions, please refer to Appendix A)*:

1) Conversion from raw image to grayscale. This is represented by Figure 6 (a)-(b).
2) After a grayscale image has been obtained, leveling is done on the image via histogram equalization to correct for any exposure differences. This is represented by Figure 6 (b)-(c) and Figure 7.
3) After the image has been corrected for exposure issues, homomorphic range compression is carried out on the image. This enhances the image contrast and prepares it for the next step in the pre-processing stage. This is represented by Figure 6 (c)-(d) and Figure 8.

4) The final step in the pre-processing stage is the conversion of the gray-scale image into a binary image. This is performed using bi-level thresholding and is represented by Figure 6 (d)-(e).

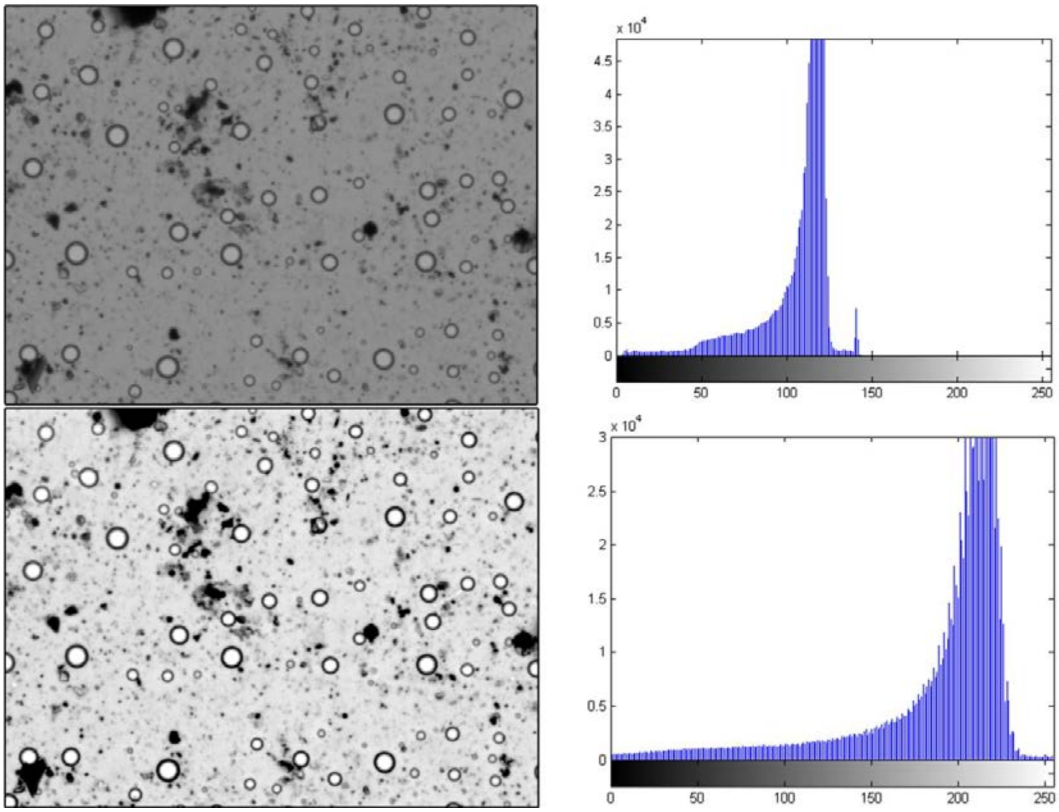

Figure 7: Images (b) & (c) from **Figure 6** and their respective histogram profiles

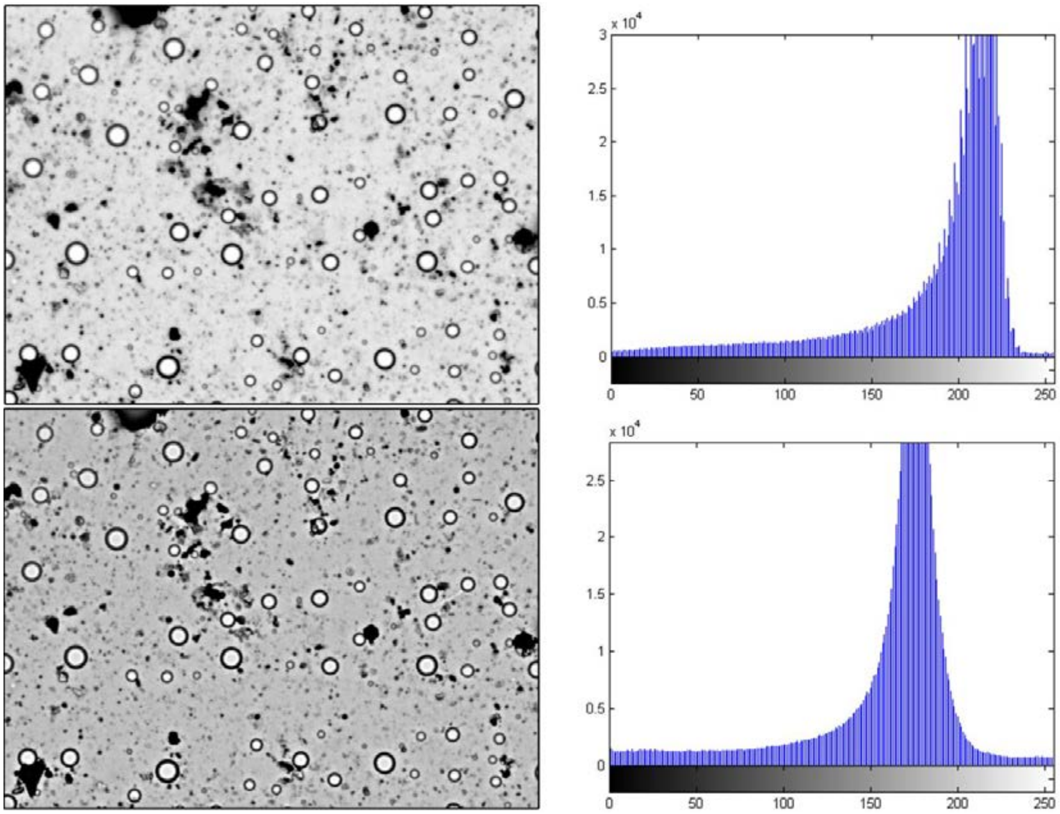

Figure 8: Images (c) & (d) from Figure 6 and their respective histogram profiles

2.2.3.2 Water Droplet Detection

The motive behind this study was to produce an image analysis protocol to obtain data of water droplets in diluted bitumen during bitumen clarification so as to understand the water droplet dynamics. This information will allow us to study the effects of mixing on demulsifier performance. One of the major challenges faced in this process is that the diluted bitumen is a multiphase system with bitumen, water droplets, air bubbles, fines and minerals. This causes the images to be cluttered with artefacts, as compared to a simple water-in-oil emulsion. Fines are present in the micrographs and contribute towards the noise in the micrographs. As a result, it is even more important that high quality images are taken in order to make the image analysis protocol even feasible.

Water droplets generally maintain a spherical shape due to their surface properties. Using this fact, it was concluded that the best way to perform water droplet detection on the diluted bitumen images would be to identify and count the number of circles present in the image, as well as obtaining a droplet size distribution of these circles. This procedure is called Circle Detection. As mentioned earlier, air bubbles are also present in the system and might appear in some micrographs. Air bubbles are also spherical and it was a concern that the circle detection algorithm will not be able to differentiate between the air bubbles and water droplets. Further studies were done and it was concluded that air bubbles were of a different size range than the water droplets, much larger than the 1~12 μm range for water droplets, and can be easily identified and differentiated on images.

As mentioned earlier in this chapter, the circle detection algorithm used in this water droplet detection protocol was developed by a MSc. student from the University of Alberta. In his protocol, he employed a pre-processing algorithm as well as a circle detection algorithm. It was determined that the pre-processing procedure of Fovea Pro 4.0 was more efficient when it comes to handling the diluted bitumen systems. As a result, only the circle detection segment of his algorithm was extracted and implemented in this protocol. The fifth step in this image analysis protocol, after the initial pre-processing steps, would be circle detection.

5) The final piece to this image analysis protocol is the Hough Circle Detection Algorithm (Purwar, 2011). It takes the binary image from

Figure 6(e) and detects for circles within a specified sensitivity. The result of this algorithm is represented by Figure 6(f).

After the following 5 steps are performed, data regarding the number of water droplets, water droplet sizes as well as the x-y coordinates of the droplet centers are recorded for further processing. Automation capabilities were also incorporated into this protocol for batch processing. Further details regarding the algorithms used are discussed in Section 2.3.

2.3 Algorithms used in the Water Droplet Detection Image Analysis Protocol

Image enhancements and defect corrections are often required when preparing an image for analysis. This can be done in either the Spatial Domain, which is the array of pixels that represents the image, or in other domains such as the Frequency Domain. Operations in the Spatial Domain directly modify the pixel values. Therefore, when an operation is performed on an image in the Spatial Domain, every single pixel in the image would have to be processed. As a result, operations in the Spatial Domain will generally require more computational power, while similar operations can be done in the Frequency Domain with much ease. Also, operations made in the Spatial Domain are irreversible and there is no option to reconstruct the image in order to retain the original image data. The Frequency Domain is used as a means to compress the image (forward transform) while having the option to reconstruct the image back into the Spatial Domain (reverse transform). This allows for the preservation of image quality and data. Operations performed in Spatial Domain include the Histogram Equalization while the Forward Fourier Transform and the Hough Transform are performed in the Frequency Domain.

2.3.1 Histogram Equalization

Figure 9 & Figure 10 shows the effects of histogram equalization in correcting any exposure defects present on a grayscale image. Figure 9 shows the brightness histogram of an image with exposure issues and the brightness histogram of the image after histogram equalization has been performed. Figure 10 shows the cumulative distribution plot for the brightness values for the same image before and after histogram equalization.

Each grayscale image has a brightness histogram which shows the frequencies of the 256 shades of gray, with each shade of gray representing the brightness value of a pixel. Peaks in the histogram represent more common brightness values (a higher peak means more pixels having that brightness level), while valleys in the histogram represents the less common brightness values.

The purpose of histogram equalization is to attempt to spread out the brightness values in the peak areas and compress them in the valleys as evenly as possible, attempting to fit a cumulative linear plot as closely as possible. In theory, this would allow for the same number of pixels at each possible brightness level. This is often not the case and histogram equalization often just ends up spreading out the brightness values as much as possible while retaining the image data. This process is called leveling as it “levels” out the image brightness histogram. This removes the uneven background light which “contaminates” the image and causes error in the later stages of image processing.

The redistribution of pixels to different brightness values is made possible by reassigning new brightness levels to each individual pixel. However, the brightness order of the pixels, which is the relative brightness of each pixel to another pixel darker and brighter than it, is retained during this process, which in turn retains the data in the image. The reassigned brightness value can be calculated with the following equation:

$$\mathrm{k} = 256 \cdot \sum_{i=0}^{j} \frac{N_i}{T} \tag{7}$$

where j is the brightness level in the original image, ranging from 0 to 255

k is the reassigned brightness value

T is the total number of pixels

and N_i is the number of pixels with brightness value equal to or less than j

It can be seen from Figure 9 that the brightness values in (d) are much more spread out than in (b) and from Figure 10 that the cumulative distribution plot in (d) is more evenly spread out compared to (b).

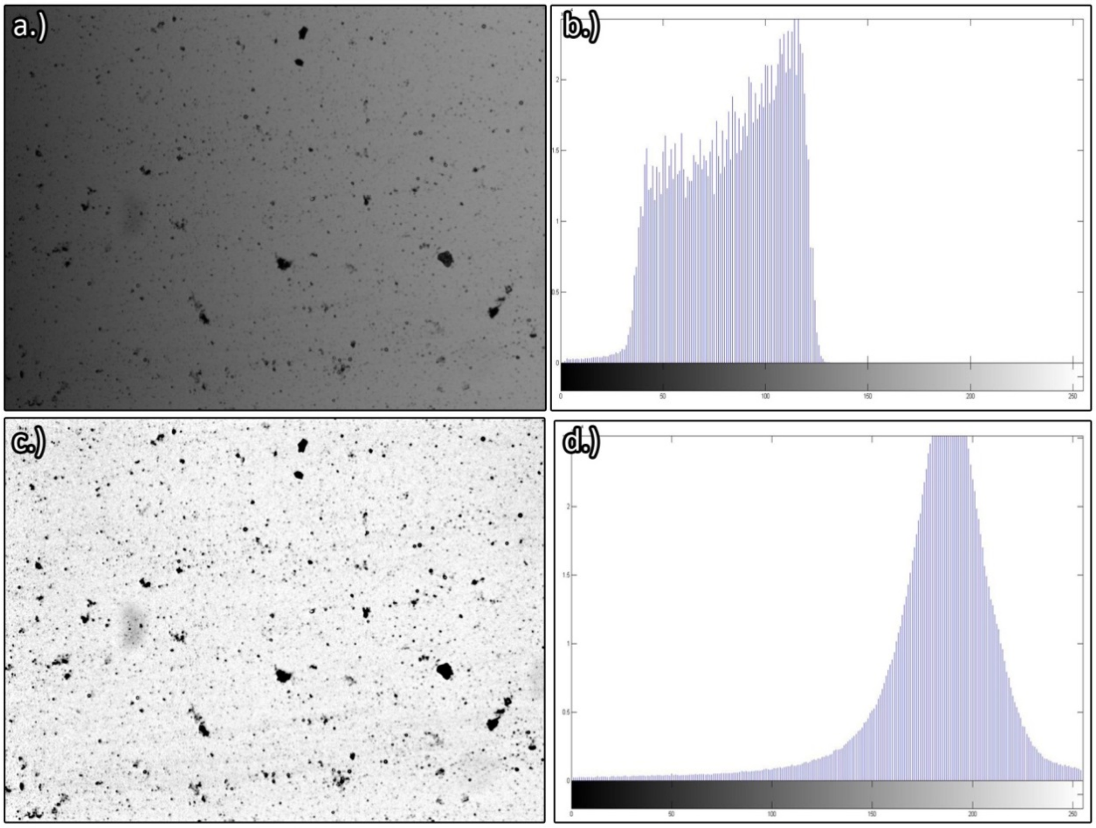

Figure 9 : Effects of Histogram leveling on Image with Exposure Defections. (a)-(b) Original Image and Histogram; (c)-(d) Corrected Image and Histogram

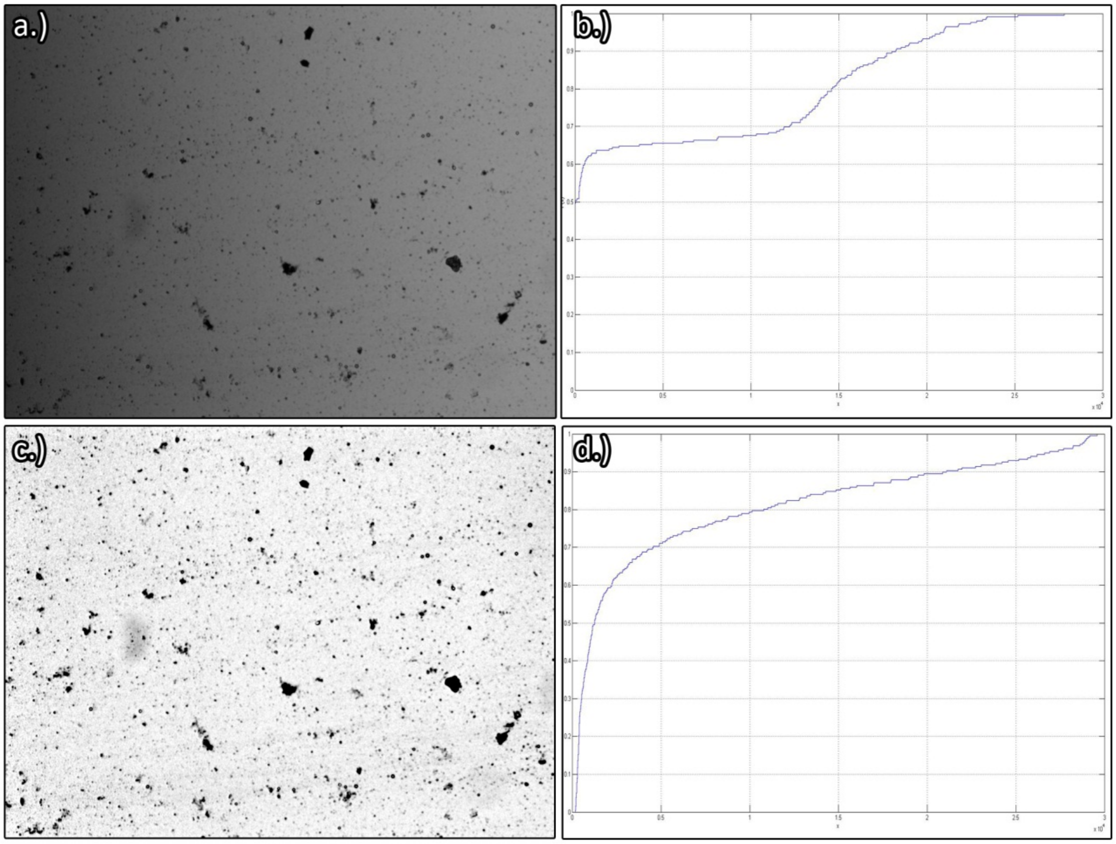

Figure 10: Effects of Histogram leveling on Image with Exposure Defections.
(a)-(b) Original Image and Cumulative Distribution Plot; (c)-(d) Corrected Image and Cumulative Distribution Plot

2.3.2 Fourier Transform

The Fourier Transform states that it is possible to fit any one dimensional function to a summation of a series of sine and cosine terms of increasing frequency. The continuous Forward Fourier Transform of the function *f(x,y)* will be written as *F(u)*, which is written as:

$$F(u) = \int_{-\infty}^{\infty} f(x, y) \cdot e^{-i2\pi(ux)} dx \tag{8}$$

where $e^{-2\pi i(ux)}$ is the mathematical identity from Euler's Formula:

$$e^{-2\pi iux} = \cos 2\pi ux - \mathrm{i} \cdot \sin 2\pi ux \tag{9}$$

The function *f(x)* is a real function, however the Fourier Transform function *F(u)* is generally a complex function and can be expressed in polar coordinates as:

$$F(u) = |F(u)| \cdot e^{i\varphi(u)} \tag{10}$$

where $|F(u)|$ is the amplitude and $\varphi(u)$ is the phase. The square of the amplitude $|F(u)|^2$ is the power spectrum of the function *f(x)*. The integral from minus infinity to infinity can be approximated as a summation of terms:

$$F(u) = \frac{1}{n} \cdot \sum_{x=0}^{N-1} f(x) \cdot e^{\frac{-2\pi iux}{n}} \tag{11}$$

where n is the number of sample points in the image for a finite number of points. The terms in this series are independent and a higher number of terms improve the quality of the fit (i.e. higher resolution image produces a better fit).

For a two dimensional function (i.e. a two dimensional image), it is possible to perform the Fourier Transform separately in each dimension (x and y) and obtain the desired two-dimensional transform. The Fourier Transform transforms the image into frequency space, assigning complex values to each pixel in the image. This provides the amplitude for each pixel and the square of the amplitude is the image's power spectrum. The power spectrum shows frequency values and orientation of each pixel, this is used for detecting and isolating periodic structures (such as water droplets) or noise. The function *f(x)* for an image would be a step function, expressing the spatially varying image brightness. Step functions are important in images as a step in brightness levels corresponds to the edge of an object in the image. Two types of filtering can be applied using the Fourier Transform, namely low pass filtering, which suppresses the amplitudes at higher frequencies, and high pass filtering, which suppresses the amplitudes at lower frequencies. The homomorphic range compression filter used in this study applies high pass filtering to define the features present in the image, while removing the noise present in the image at the same time by reducing the magnitude of the low frequency components to zero. The frequency range is usually specified based on the power spectrum display of the Fourier Transform Image but is pre-determined by the filter that was set in the Homomorphic Range Compression filter in Fovea Pro 4.0 in this study.

The Fourier Transform requires images to have dimensions that are an exact power of 2 (i.e. 64 pixels by 64 pixels, 128 pixels by 128 pixels, 256 pixels by 256 pixels, 512 pixels by 512 pixels, 1024 pixels by 1024 pixels, etc.). However, if the image dimensions are not an exact power of 2, the image will be embedded in a larger image (which has dimensions that are an exact power of 2) consisting of either zero amplitudes or an average brightness values of the pixels.

This process is called padding and it allows for the Fourier Transform to be applied on images of different dimensions. This would increase the processing time due to the increase in image size.

The Fourier Transform also assumes that the functions being transformed are continuous. This means that the image has matching left and right or top and bottom edges. This is generally not the case. As a result, the edges of the image are no longer sharp due to a loss in frequency.

As mentioned earlier in this chapter, one of the factors affecting the quality of the image would be the focus of the image. For a well-focused image, the average amplitude as a function of frequency (radial) gradually decreases but decreases abruptly for un-focused images due to the lack of high frequencies. This reduces the efficiency of the Forward Fourier Transform.

2.3.3 Bi-level Thresholding

Each image has 256 gray scale values, each value corresponding to a brightness value. Thresholding works by setting a range of brightness values to be considered as “important”, such that pixels that have brightness values within this range will be set as the foreground of the image, while the pixels with brightness values outside of this range will be deemed as “un-important” and will be set as the background of the image. In this case, the foreground pixels will be black and the background pixels will be white, this creates a binary image. This allows for the removal of noise in the original image by setting it to be the background as the brightness values of the noise pixels are generally in a different range as the objects in the image.

The one thing that would make or break the process of producing a binary image through thresholding is the range of brightness values which represent the foreground/objects of the image. There are many methods to adjust threshold settings, with the basic being a manual adjustment, where the operator will select the range of brightness values based on visual inspection. However, this method is unreliable and inefficient when large numbers of images are required to be processed. As a result, a number of algorithms have been developed for the automation of the thresholding procedure. The simplest method would be to locate the peaks in the histogram and to set the thresholds in between them. Another method would be to select a fixed percentage of the brightest or darkest pixels to produce a binary image. The more popular Thresholding algorithms are the Trussel algorithm (Trussel, 1979), Yager algorithm (Yager, 1979) and Otsu (1979).

The Trussel Algorithm operates by using the Student's t-test for unequal sample sizes and unequal variance, where *t* is expressed by the following equation:

$$\mathrm{t} = \frac{|\bar{x}_B - \bar{x}_D|}{\sqrt{\frac{s_B^2}{n_B} + \frac{s_D^2}{n_D}}} \qquad (12)$$

where $\bar{x}_B$ and $\bar{x}_D$ are the means for the brighter pixel population and the darker pixel population respectively

s_B and s_D are the standard deviations for the brighter and darker populations respectively and n_B and n_D are number of pixels in the brighter and darker populations respectively

This adaptation of the Student's t-test is also known as the Welch's t-test, which is used for two samples which have unequal variances.

The Trussel Algorithm sets a threshold setting that would result in the largest possible value of *t*. This produces the desired separation of the two groups of pixels. It works on the assumption that the two populations are accurately represented by their means and standard deviations (i.e. populations are normally distributed). The normal probability plot of the micrographs of diluted bitumen samples were linear for approximately 50% of the graph but completely deviated from the normal line at certain points. This meant that the Trussel Algorithm could not be used in this study.

Further research was done into the available algorithms in Fovea Pro 4.0 and an algorithm written by Johannsen (Johannsen, 1982) proved to be promising. This algorithm is based on the entropy of the brightness level histograms. This entropy is also referred to as Shannon's Entropy.

A probability distribution of n-terms can be expressed by the following equation:

$$0 \leq P_i \leq 1; \sum_{i=1}^{n} P_i = 1 \tag{13}$$

where P_i the probability mass function of outcome i (where i refers to brightness values in this case).

The Shannon Entropy of this probability distribution can be expressed by the following equation:

$$\mathrm{H}(\mathrm{P}_i) = -\sum_{i=1}^{n} P_i \log_b P_i \tag{14}$$

where b is the base of the log (common values are 2, e & 10. Each value produces a different unit for entropy.)

When all P_is are equal, $H(P_i)$ would be at its maximum value and at its minimum when all P_is, with the exception of one, are zero. This means that the more non-uniform the distribution is (i.e. multiple peaks), the smaller its entropy. For brightness values, we can define P_i with the following equation:

$$P_i = \frac{N_i}{N} \tag{15}$$

where N_i is the frequency in which the brightness value i *(*$1 \leq i \leq 256$*)* appears in the image

and N is the number of pixels in the image

$$\mathrm{N} = \sum_{i=1}^{n} P_i \tag{16}$$

Johannsen assumed in his paper that all P_i had to be greater than zero. The pre-processing of the micrographs with Steps 1, 2 & 3 ensures that this assumption is true. In his algorithm, Johannsen defines his two sets of brightness values by minimizing their interdependence to each other. The following section briefly explains how that can be done.

As mentioned earlier, thresholding an image is the same as splitting the brightness values into two different groups, foreground/object group and the background group. This can be expressed with the following equations:

$$G_k = \{1, \cdots, k\} \; and \; \bar{G}_k = \{k+1, \cdots, n\} \tag{17}$$

$$and$$

$$N_k = \sum_{i=1}^{k} P_i \; and \; \bar{N}_k = \sum_{k+1}^{n} P_i \tag{18}$$

where G_k and $\bar{G}_k$ represent the two different groups.

and N_k and $\bar{N}_k$ represent the number of pixels in each group

The entropies of both these sets can be represented with the following set of equations:

$$\mathrm{H}_k = H\left[\frac{P_1}{N_k}, \cdots, \frac{P_k}{N_k}\right] \tag{19}$$

$$and$$

$$\bar{\mathrm{H}}_k = H\left[\frac{P_{k+1}}{\bar{N}_k}, \cdots, \frac{P_n}{\bar{N}_k}\right] \tag{20}$$

In Johannsen's algorithm, he defined the interdependence of the two sets with the following equation:

$$\delta_k = S_k + \bar{S}_k \tag{21}$$

where δ_k represents the interdependence between the two sets and the algorithm converges when δ_k is minimized.

S_k and $\bar{S}_k$ represents the percentage the gray level k contributes towards the set (G_k and $\bar{G}_k$) respectively. They can be represented with the following equations:

$$S_k = H_k - P(G_{k-1}|G_k)H_{k-1} \tag{22}$$

and

$$\bar{S}_k = \bar{H}_{k-1} - P(\bar{G}_k|\bar{G}_{k-1})\bar{H}_k \tag{23}$$

The bi-level thresholding algorithm would attempt to define the two sets of brightness values so as to reduce their interdependence which can be calculated from Equation (21).

Figure 11 shows an example of how bi-level thresholding works. In this example, the threshold range was set to have the outline of the tree deemed as the foreground of the image, creating a black outline of the tree, which the other brightness values were set as the background of the image, rendering them white.

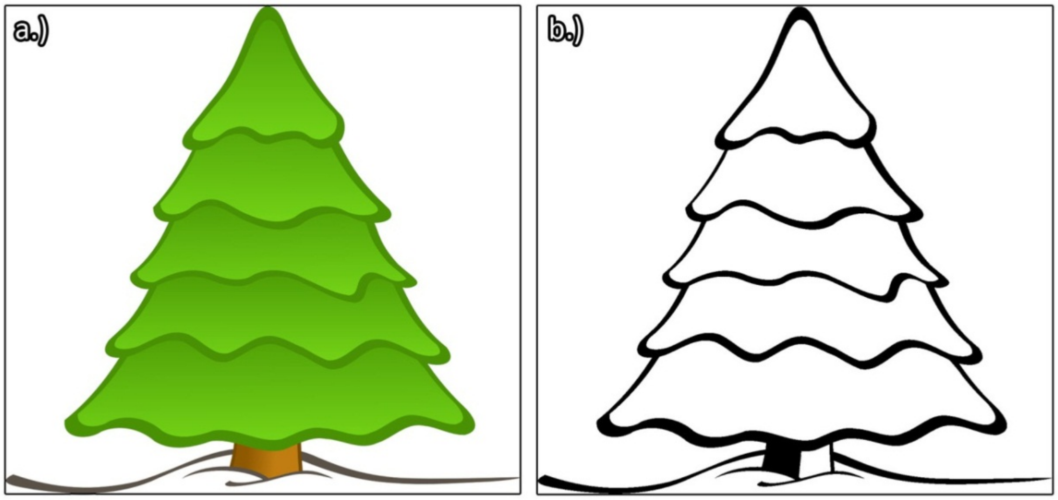

Figure 11: Example of Bi-Level Thresholding. (a) Original Stock Image; (b) Binary Image

Stock photo obtained from http://www.clipartist.net

2.3.4 Hough Transform

Each individual pixel in an image can be represented by a sinusoidal line in Hough Space. The most basic application of Hough Transform is to identify straight lines in an image, but it has the potential to identify other shapes in the image as well (i.e. circle detection). How it works is that an intersection of two sinusoidal lines in Hough Space represents a line that passes through those two points in the real space (Gonzalez et al., 2001). Each point on the sinusoidal line represents a straight line that passes through the point in the real space, with the orientation of the straight line changing as we move along the sinusoidal line.

The Hough Space is an accumulator space and it translates each pixel in the real image into an array of cells with coordinates of angles ϕ and radius r. It sums up the number of sinusoidal lines which intersect in the Hough Space (based on the pre-determined shape) at different points and these intersection points represent the pre-determined shape in the real image, with the intersecting lines representing the pixels that fall within this pre-determined shape. For example, all the points/pixels in the real image which intersect at certain points (defined by the shape that is being fitted for) in the Hough Space can be fitted to a pre-determined shape present on the image, such as a circle. Each of these intersection points will receive a “vote” for each passing sinusoidal line. The intersection points with the most “votes” will be interpreted as the lines that pass through multiple pixels in the real space image.

A modified version of Hough Transform called Circular Hough Transform was used in this protocol. This fits the pixels in the real image to a circle based on the intersection points of the sinusoidal lines. These intersection points represent the edge of a circular object in the real image space. The conventional Hough Transform for straight lines is in a two-dimensional space, with the variables being the radius r and the angle ϕ. For the Circular Hough Transform, a three-dimensional space is required as three variables are required to define a circle, x-y coordinates of the circle origin and the circle radius r. This modifies the parameter equation for the Circular Hough Transform to the following:

$$a = x - r\cos\phi \tag{24}$$

$$\mathrm{b} = \mathrm{y} - \mathrm{r}\sin\phi \tag{25}$$

where for each angle ϕ and a given radius range, we can calculate the values of ‘a’ and ‘b’ for every given point (x, y). These ‘a’ and ‘b’ values represent the x-y coordinates of the circle origin.

The edge pixels that lie on the same circle (rather than a line as compared to a conventional Hough Transform) are assigned to one accumulator array (based on the ‘a’ and ‘b’ values) and this process is repeated for every pixel in the image. The accumulator arrays would contain the information regarding the x-y coordinates of the center of the circle along with its corresponding radius.

2.4 Comparison Between Protocols

As mentioned earlier, the Water Droplet Detection Image Analysis Protocol used in this study is a combination of two pre-existing algorithms along with some modifications to optimize performance efficiency. A study was run to compare the efficiency, pros and cons of each protocol. Table 1 shows the comparison between these two protocols against data obtained by physically counting the water droplets and measuring the water droplet sizes and Table 2 shows the accuracy of the protocols. The five images were chosen at random and the manual data extraction was performed prior to running the programs so as to remove subjective bias. Appendix B shows the sample procedure in which the benchmark tests were run. One of the protocols (Fovea Pro 4.0) was unable to produce any sensible data and could not be compared against the other two.

Table 1: Summary of Benchmark Tests performed on Two Protocols

	Water Droplet Detection Image Analysis Algorithm			Hough Circle Detection Program			Manual Data Extraction		
Run #	# of Droplets	Average Droplet Size (µm)	Processing Time (s)	# of Droplets	Average Droplet Size (µm)	Processing Time (s)	# of Droplets	Average Droplet Size (µm)	Processing Time
1	51	4.37	5.59	77	2.91	49.84	55	4.34	20 min
2	15	5.89	5.59	152	2.67	39.44	15	5.96	5 min
3	157	3.33	6.04	281	2.69	38.29	179	N/A	N/A
4	55	4.04	5.81	288	2.41	39.24	62	3.75	20 min
5	66	4.05	5.74	77	2.91	40.38	64	3.68	20 min

Table 2: Percent Error of Data obtained from Protocols compared to Manual Measurements

	Water Droplet Detection Image Analysis Algorithm		Hough Circle Detection Program	
Run#	Droplet Detection Percent Error	Droplet Size Percent Error	Droplet Detection Percent Error	Droplet Size Percent Error
1	7.27%	0.69%	-40.00%	32.95%
2	0.00%	1.17%	-913.33%	55.20%
3	12.29%	N/A	-56.98%	N/A
4	11.29%	7.71%	-364.52%	35.73%
5	3.13%	10.05%	-20.31%	20.87%
Average	6.80%	4.91%	-279.03%	36.19%

2.4.1 Fovea Pro 4.0 Image Analysis Protocol

The Fovea Pro 4.0 Image Analysis Protocol has strong capabilities in image standardization but lacks the critical ability to extract drop size from the image. As a result, this image analysis was not suitable for the purposes required in this study and a comparison could not be drawn between this protocol and the other two protocols.

2.4.2 Purwar's Hough Circle Detection Protocol

It can be seen from Table 2 that this protocol is extremely inaccurate and has an average droplet detection error of 279%, which meant that it frequently detected water droplets that did not exist on the actual image, and a processing time ranging from 38 to 50 seconds per image along with a droplet size accuracy of 64%. This meant that the protocol had a much lower accuracy and a higher processing time, compared to the newly developed Water Droplet Detection Image Analysis Protocol. This protocol is a two stage protocol with the pre-processing stage and the circle detection stage. However, as seen from Figure 5, the pre-processing stage in this protocol, steps (b) - (e), is weak and requires major improvements to compensate for the complexity of diluted bitumen systems. As a result, this image analysis protocol was not suitable for the purposes required in this study.

2.4.3 Water Droplet Detection Image Analysis Protocol

This protocol is the final image analysis protocol produced from this study. It consists of two main stages, the pre-processing stage, where images are calibrated to a certain standard, and the droplet detection stage, where the water droplets are identified and their data extracted. The standardization of images allows for batch processing of images, allowing for a larger sampling size and statistically accurate results, the only limitation of the size of the batch would be the processing capabilities of the computer used. As can be seen from Table 2, when compared to manual measurements, this protocol has an average accuracy of 93.2% in detecting water droplets present in the image and a processing time ranging from 5.5 to 6.0 seconds per image. It also has a droplet size measurement of 95.1% accuracy. These benchmarking results verify that this algorithm is an accurate and convenient tool for obtaining water droplet size distributions.

This protocol is much more time efficient compared to manual measurement of water droplets while maintaining a good accuracy. It is also able to perform in conditions when manual measurement is not feasible. This can be seen from Run #3, where it was unfeasible to obtain the water droplet data manually due to the high number of drops present.

2.4.4 Automated drop detection for online particle size monitoring in multiphase system

Part way through the study, a new image analysis algorithm was discovered. This image analysis algorithm was designed for multiphase systems by Sebastian Maaβ (Maaβ et al. 2012). A comparison was made between the

Water Droplet Detection Image Analysis Protocol and Maaβ's drop detection algorithm. Both algorithms followed the same pre-processing stage to minimize the misleading information present on the images. The difference between the two programs lies in the pattern recognition stage. In the Water Droplet Detection Image Analysis Protocol, the circular Hough transform was used to identify the circular droplets. In Maaβ's algorithm, it is "trained" to recognize the droplets by compiling the patterns of the droplets of varying sizes. The algorithm would then proceed to identify patterns present on all images being processed and match them with the compiled database of patterns. These patterns include the intensity signature curves unique to the droplets. Some sample images went sent to Dr. Maaβ for analysis and the results provided were compared against the results obtained from the Water Droplet Image Analysis Algorithm. It was found that the Water Droplet Image Analysis Algorithm provided more accurate results when compared to the manually obtained data, with Dr. Maaβ's algorithm identifying some of the fines as droplets. However, further tuning of Dr. Maaβ's algorithm is required in order to fully utilize its capabilities so this comparison may not be fully representative of Dr. Maaβ's algorithm.

2.5 Conclusions

Manual measurement of the water droplet sizes is subject to operator error which cannot be properly accounted for as the degree of error produced depends on each individual. By having a standardized image analysis protocol, human error and random bias are eliminated. It also reduces the processing time required.

Both Fovea Pro 4.0 and Purwar's Hough Circle Detection Image analysis protocol have unique strengths, but are incomplete.

The Water Droplet Detection Image Analysis Protocol was developed from these two protocols, with the idea of extracting the individual strengths of the protocols and combining them together to obtain a new protocol which has the strengths of both protocols but none of the weaknesses. This new protocol was then further optimized to allow for batch processing of images and also reduced operation time. The final protocol has a droplet count detection accuracy of 93.2% and a droplet size measurement accuracy of 95.1%. In addition, the newly developed protocol has an average processing time of 5.5 seconds per image, which is significantly faster than the manual measurements and the protocols proposed earlier.

This newly developed image analysis protocol was used in the study the effects of mixing on the water droplet dynamics during diluted bitumen clarification.

Chapter 3: Effects of Mixing on Water Droplet Dynamics in Diluted Bitumen Clarification

Two experimental campaigns were performed to study the effects of bulk demulsifier concentration, demulsifier injection concentration, mixing intensity and mixing time on water droplet dynamics in bitumen clarification. These experiments were carried out in a novel confined impeller stirred tank (CIST) to provide a solid foundation for subsequent scale-up (Laplante, 2011). The purpose of this study is to provide an understanding of the significance of the different variables on the performance of the demulsifier in diluted bitumen clarification. Understanding the effects these variables have on demulsifier performance would allow for the optimization of this process. This was done by analyzing the number of water droplets present per microscope slide, as well as the average water droplet diameter. These data were obtained through the Water Droplet Detection Image Analysis Protocol discussed in Chapter 2. The results are compared with Karl-Fisher water titration results from Jeng Yi Chong (Chong, 2013).

3.1 Experimental Setup

Figure 12 shows the experimental setup that was used in this study. Two Confined Impeller Stirred Tanks (CISTs) were used in the two experimental campaigns. The experimental procedure consisted of three stages, sample preparation (pre-mixing), demulsifier dispersion and batch settling. The sample is pre-mixed to ensure a homogeneous system before being transferred into the CISTs. The samples are then agitated in the CISTs and demulsifier is added through a sampling port, this allows for the dispersion of the demulsifier. Finally, agitation is stopped and the sample is allowed to settle in the CISTs. Diluted bitumen samples from the commercial froth treatment inclined plate settler (IPS) and demulsifier from Champion Technologies were provided by Syncrude Research.

Table 3 shows the composition and water droplet data for the diluted bitumen samples after the pre-mixing phase. These data were obtained from image analysis and averaged over 30 experimental runs. The diluted bitumen sample had a naphtha to bitumen ratio of 0.7 by weight. The viscosity and density of the diluted bitumen sample were measured at 80^{o}C using a Fenske viscometer and a pygnometer respectively.

The diluted bitumen was heated and premixed before being transferred into the CISTs, after which demulsifier dispersion and batch settling were carried out. Samples were obtained before and after demulsifier dispersion to obtain the water droplet data.

Table 3: Properties of diluted bitumen from Campaign 1

Average water content ± σ	2 ± 0.2
Average Hydrocarbon content ± σ	96.9 ± 0.3
Average # of droplets/slide ± σ	38 ± 9
Average Droplet Sizes ± σ (μm)	3.79 ± 0.13
N/B	0.7
Density, 80°C (kg/m^3)	860
Viscosity, 80°C (cSt)	6.1

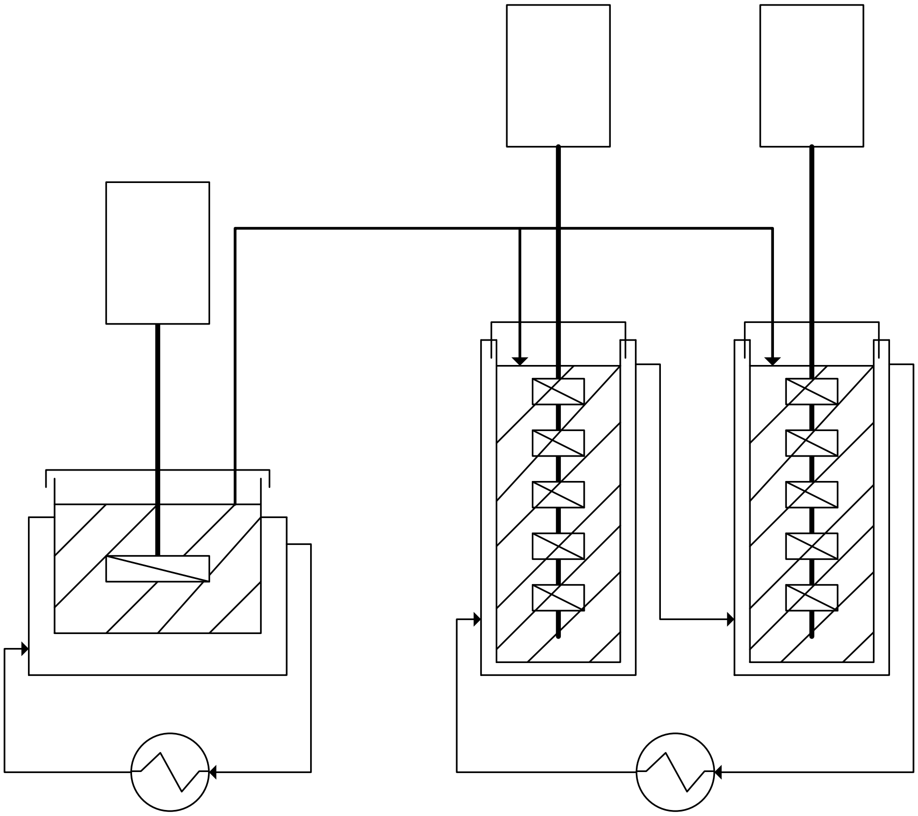

Step 1: Pre-Mixing
- Heating for 30 minutes to 60 °C
- Agitation at 1000 rpm for 15 minute while heating to 76.5 °C

Step 2: Demulsifier Dispersion
- Add diluted demulsifier into CIST 1 and 2.
- Mix for time t and specified agitation level.

Step 3: Settling
- Batch gravity settling for 60 minutes
- Sample water content at 1, 3, 5, 7, 10, 30 minutes into settling

Figure 12: Schematic of Experimental Setup and Procedure*

**Reproduced with the permission from Laplante (2011)*

3.1.1 Pre-Mixing

4L cans of diluted bitumen samples from Syncrude Research were stored upside down in a fridge at 5 ^{o}C. These paint cans contained approximately 2.7L of diluted bitumen per can. The diluted bitumen was re-agitated prior to demulsifier dispersion so as to accurately represent the behavior of diluted bitumen in the industrial process. Pre-mixing was found to have a substantial effect on the initial water content as it re-suspends the solids and water which may have settled during storage (Laplante, 2011). Pre-mixing was done by pre-heating the diluted bitumen to 60 ^{o}C without mixing, followed by mixing at a speed of 1000 RPM till the temperature of the diluted bitumen reaches 76.5 ^{o}C. The pre-mixing stage was carried out in the 4L cans.

Table 4 shows the pre-mixing tank dimensions and mixing parameters. A 45^{o} pitch blade turbine down pumping (PBTD) was used and standard T/10 baffles were attached to the paint can to promote turbulence. At the end of pre-mixing, a sample was obtained using silanzed glassware and used for microscopic analysis. The pre-mixed diluted bitumen was then pumped into the two CISTs using a Masterflex Pump for the next phase in the experiments.

Table 4: Pre-mixing tank dimensions and mixing parameters

Impeller Type	45^{o} PBTD
Tank diameter, T (m)	0.16
Impeller diameter, D (m)	0.08
Liquid height, H (m)	0.11
Off-bottom clearance, C (m)	0.04
Total Impeller Volume, V_{IMP} (m^3)	8.04E-05
Power Number, N_P	1.30
Impeller speed, N (rpm)	1000
$P/\rho\ V_{TANK}$ (W/kg)	9.20
$P/\rho\ V_{IMP}$ (W/kg)	245
Reynolds Number, Re	17558
Mixing time (min)	15

3.1.2 Demulsifer Dispersion

Figure 13 shows the design schematic of the CIST and Table 5 shows the CIST geometry and mixing specifications of the impellers. The CIST has T/12 baffles and was agitated with either 6 Intermig impellers, 5 A310 impellers or 5 Rushton impellers to provide different levels of mixing. The impellers were installed on a 63.5 mm shaft with an off-bottom clearance of 1/3D and a submergence of 1D, where D is the diameter of the impellers. The impellers were staggered successively at 60^o, 30^o and 90^o to one another for the A310s, Rushtons and Intermigs respectively. The impeller shaft was supported by a steady bearing at the bottom of the CIST. The CISTs were also jacketed to allow for the circulation of ethylene glycol, which served as a heating fluid. Stainless steel 3/8” sampling and injection ports protruded from the tank lid as part of the CIST design. These ports allowed for accurate sampling and demulsifier injection into the system.

The demulsifier was diluted to the desired concentration using xylene. The demulsifier was injected into the CIST 5mm above the upper impeller blade tip (33mm below liquid surface) during mixing to promote a high initial dispersion of demulsifier. This was done using either a syringe or pipette or a 1/8” polyethylene tubing connected to a syringe pump, depending on the bulk concentration of the demulsifier and the injection concentration required for the experimental run.

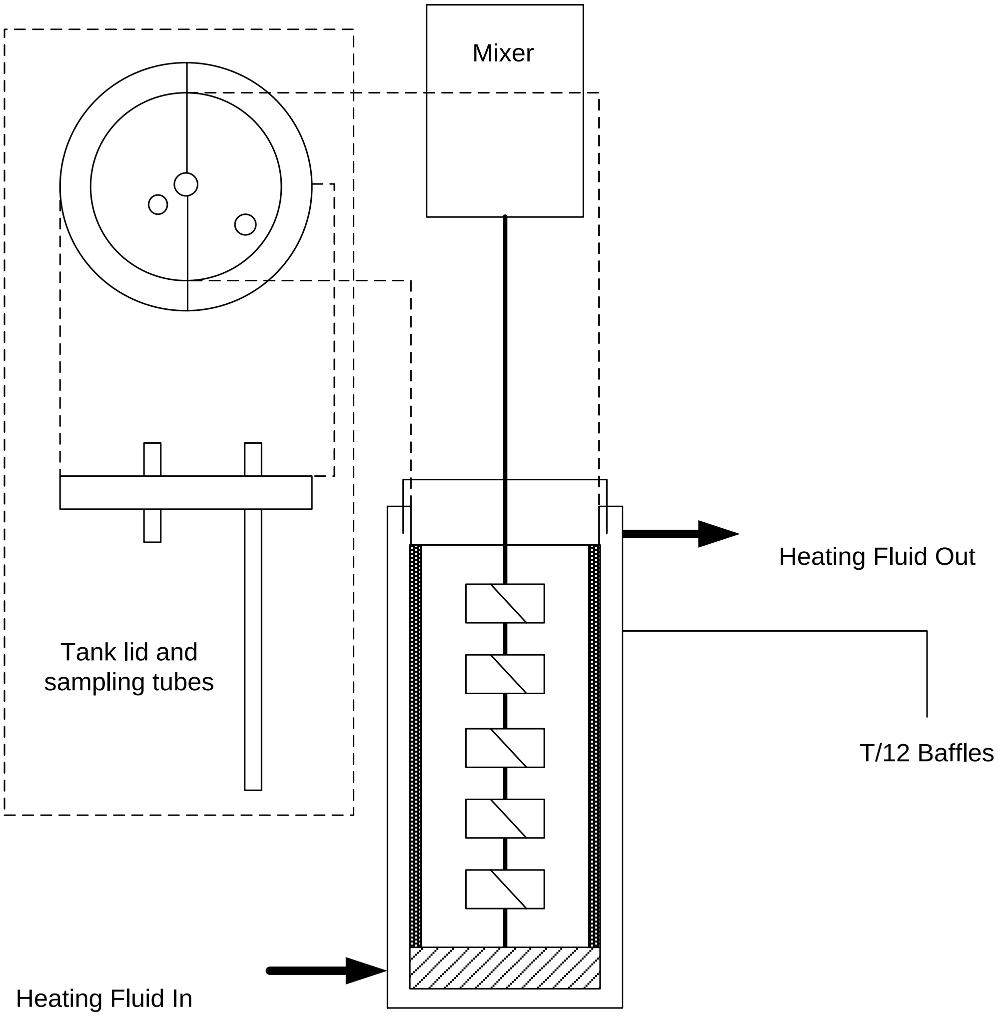

Figure 13: Design Schematic of the Confined Impeller Stirred Tank (CIST)*

**Reproduced with the permission of Laplante (2011)*

Table 5: CIST geometry and mixing specifications

Impeller Type	**Intermig**	**A310**	**Rushton**
Tank diameter, T (m)	0.075	0.075	0.075
Number of impellers	6	5	5
Impeller diameter, D (m)	0.050	0.038	0.038
Impeller speed, N (rpm)	250	1000	600
Liquid height, H (m)	0.225	0.225	0.225
Off-bottom clear of bottom impeller, C (m)	0.017	0.013	0.013
Submergence of top impeller, S (m)	0.038	0.038	0.038
Tank volume, V_{TANK} (m^3)	9.94E-04	9.94E-04	9.94E-04
Total impeller vol, V_{IMP} (m^3)	1.68E-04	5.23E-05	4.31E-05
Reynolds number, Re	1715	3858	2315
Transition Flow Np per impeller*	1.3	0.65	4.6
$P/\rho\ V_{TANK}$ (W/kg)	0.18	1.13	1.71
$\varepsilon \sim P/\rho\ V_{IMP}$ (W/kg)	1	21	40

**Power number for the CIST was measured using a Torque Transducer and Ethylene glycol at 20° C with a kinematic viscosity of 6 cSt.*

3.1.3 Sampling Glassware

It is important to select a sampling tool which would avoid applying shear stresses on the water droplets, individual or flocs, which would modify their sizes and flocculation behaviour. 1/8” polyethylene tubing was used along with an auto-pipette to withdraw samples from the CIST. As the water droplets that are present in the system are approximately 2-40 μm in diameter, a standard 1mL glass pipette has a tip diameter of 1.5 mm, which provides enough clearance at the pipette tip and was selected as the sampling tool to withdraw the samples from the CIST. A chemically treated (silanized) 1 mL glass pipette was then used to transfer a small amount of the sample onto a silanized microscope slide. Samples were obtained 33 mm below the liquid surface at different time intervals throughout the experiment. Table 6 shows the details of the sampling intervals.

Table 6: Summary of Sampling Times

Label	Time
A	After Pre-mixing
C	30s before mixing ends
1,3,5,7,10,30	Minutes into settling

3.1.3.1 Silanization

Glassware used throughout this study was treated chemically by immersing them in a series of chemicals which rendered them hydrophobic, this process is called silanization. This allowed for accurate sampling of the diluted bitumen as the hydrophobicity of the glassware prevents the water droplets from undergoing any coalescence on the glassware as a result of the movement of water droplets.

Two tests were performed to determine the effect of silanization. Figure 14 shows a series of images taken from a standard microscope slide at one second intervals and Figure 15 shows the differences between samples obtained using a silanized glass pipette and a standard glass pipette.

The images in Figure 14 were taken at one-second intervals, it can be seen that the water droplet was moving on the microscope slide. This would be unacceptable for sampling as the movement of droplets on the microscope slide would not be representative of the system in the CIST.

It can be observed from Figure 15 that there were differences between samples taken using a silanized glass pipette and a standard glass pipette. Figure 15 (a) & (b) have many more water droplets than Figure 15 (c) & (d). Flocs of water droplets are present in Figure 15 (a) & (b) but not present in Figure 15 (c) & (d). Water droplets were attached to the hydrophilic walls of the glass pipette in Figure 15 (c) & (d), which results in inaccurate sampling. Samples from Figure 15 were subjected to the same sampling technique, and the only variable was the hydrophobicity of the pipettes. These four images were only a sample of the entire set of images taken and are representative of the behaviour of the entire set. It is possible for water droplets to be retained by the hydrophilic walls of the glass pipette which would result in inaccurate sampling. It should be noted that the same sample was used for all four images in Figure 15 and that the difference in contrast is due to different exposure settings and is unrelated to the pipette used.

As a result of these two tests, all glassware used in this experiment was silanized prior to use.

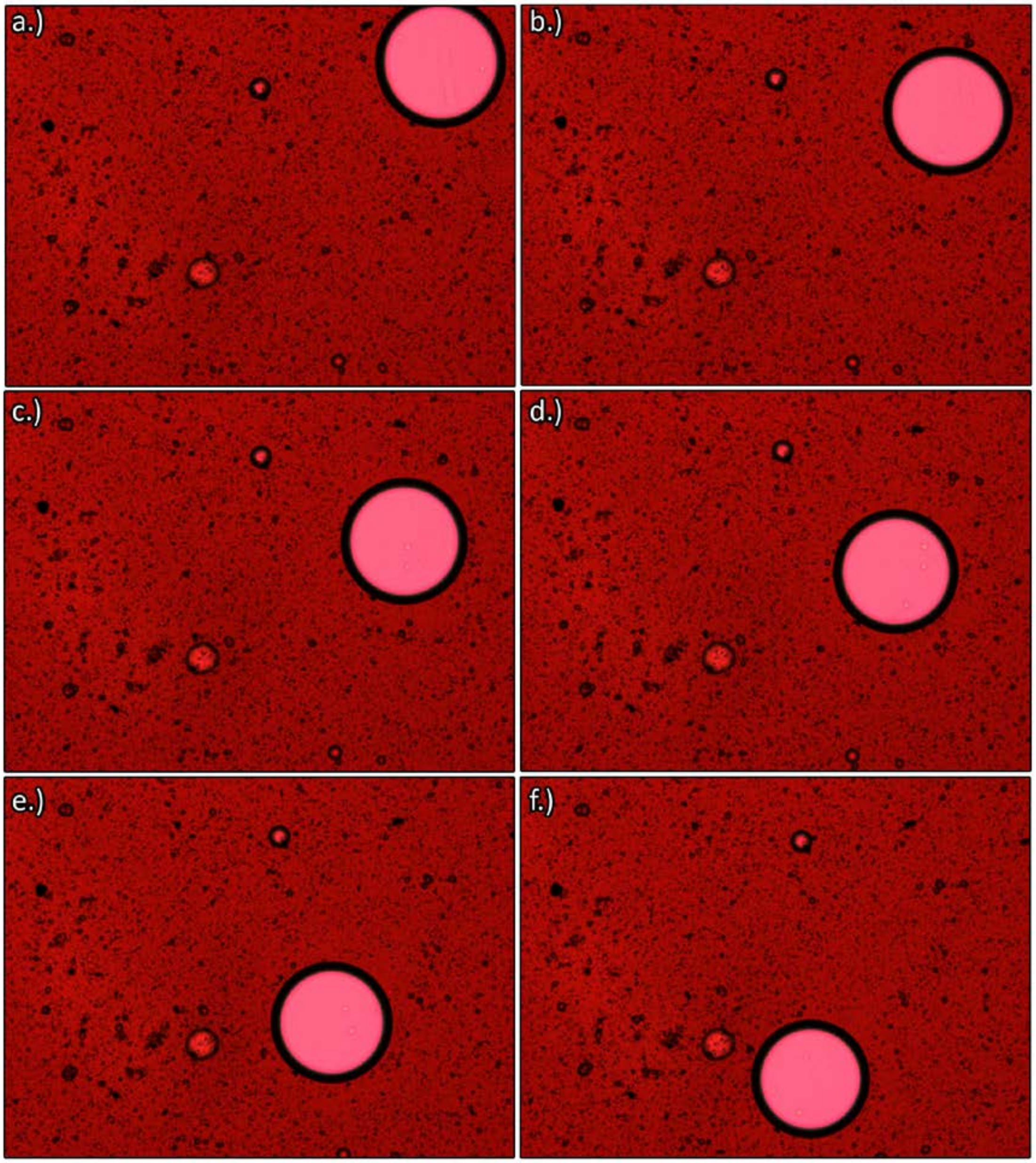

Figure 14: Images of a sample on a standard microscope slide taken at one second intervals

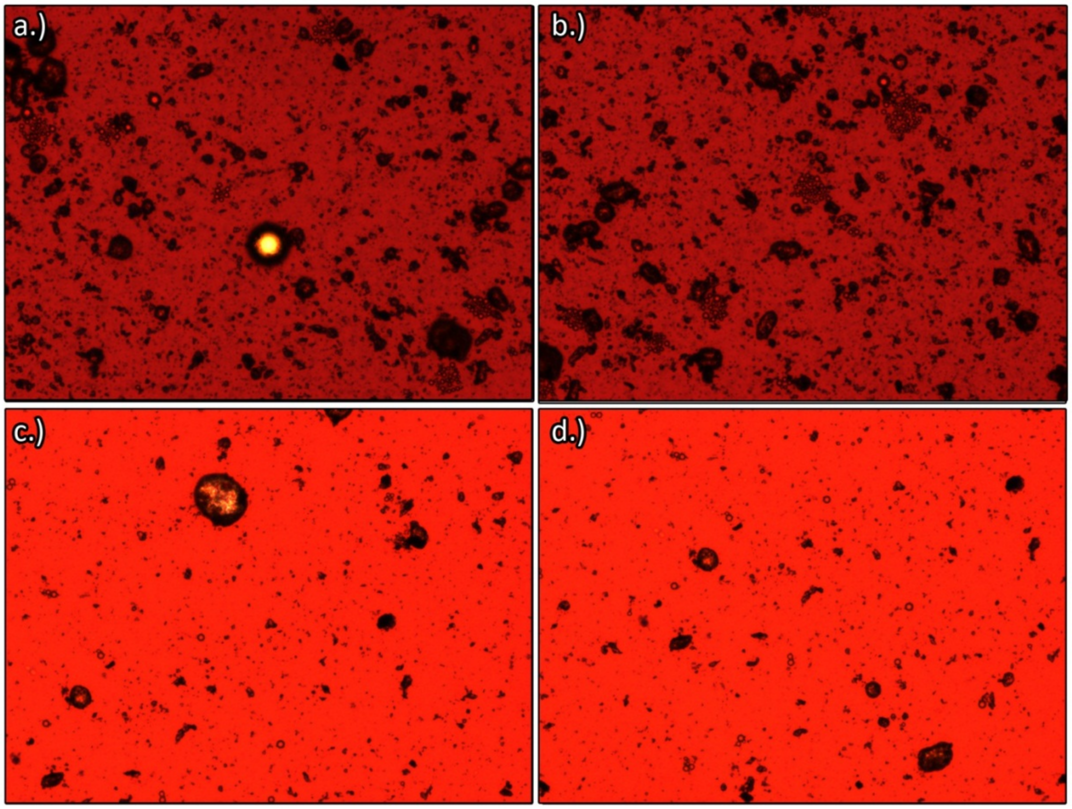

Figure 15: Effects of Silanization on Glass Pipettes. (a) - (b) Silanized Pipettes; (c) - (d) Regular Pipettes

3.1.3.2 Silanization Procedure

As mentioned before, the glassware used in this study had to be silanized prior to use. The step by step procedure for silanization is as follows:

1. Immerse surface of glassware in contact with the sample in Dicholorodimethylsilane solution ($C_2H_6Cl_2SI$) for five minutes. *Also known as silanization solution*
2. Remove glassware from silanization solution and allow to air dry
3. Immerse surface of glassware in contact with sample in toluene (C_7H_8) and remove it completely from the toluene, dipping it in a up and down motion five times.

4. Allow glassware to air dry.
5. Immerse surface of glassware in contact with sample in Acetone (C_3H_6O), dipping it in a up and down motion five times. *Similar to step 3*
6. Allow glassware to air dry and store in a fumehood

All procedures were performed in a fume hood. Silanized glassware can last up to three months and still maintain its hydrophobic properties. Caution: dicholorodimethylsilane is extremely hazardous, proper personal protective equipment must be used.

Microscope slides were silanized using the same procedure. Glass pipettes were silanized by drawing the silanization solution into pipettes and immersing the pipettes in a beaker of silanization solution and then rinsing the pipettes with toluene and acetone after.

3.2 Design of Experiments: Campaign 1

Four variables were studied, the bulk demulsifier concentration (BC), mixing intensity (ε), mixing time (t) and demulsifier injection concentration (IC). The bulk concentration and injection concentration are calculated on a mass basis. An estimate of the mixing intensity ε is obtained through the following formula:

$$\varepsilon \propto \frac{P}{\rho V_{impeller}} \tag{26}$$

where ε is the mixing intensity

P is the power supplied by the motor

ρ is the density of the diluted bitumen

and V_{IMP} is the volume of the impeller.

A Box-Behnken fractional factorial design was used to determine the number of experiments required to accurately model the effects of these four variables. Table 7 shows the variable coding for the Box-Behnken fractional factorial design and the range over which the variables were tested.

Table 7: Variable Coding for Box-Behnken

Variable	-1	0	1
Demulsifier Bulk Concentration, BC (ppm)	5	50	95
Mixing Intensity, ε (W/kg)	1	21	40
Mixing Time, t (min)	2	6	10
Injection Concentration, IC (wt. %)	3	21	39

Each variable was varied at three levels so as to observe the quadratic and interaction effects. The different levels were coded according to equally spaced intervals using this equation:

$$X_A = 2 \cdot \frac{(A - A_{Min})}{(A_{Max} - A_{Min})} - 1 \tag{27}$$

where X_A represents the level for variable A (BC, ε, t or IC)

and A_{MIN}, A_{MAX} and A represent the minimum, maximum and experimental values for A respectively.

This formula results in three coded levels of -1, 0 and +1 for each of the three design coordinates (min, central, max) for each variable as seen in Table 7.

Demulsifier was added to the diluted bitumen system to obtain a bulk concentration range of 5, 50 or 95 ppm, which is the commercial application range of the demulsifier. The mixing intensity was obtained by changing the CIST mixing configuration and N to obtain the maximum energy dissipations of 1, 21 and 40 W/kg as shown in Table 5. This range was selected to cover the different energy dissipation levels from agitation in an open pipe to agitation with a static mixer (Laplante, 2011). Different impellers were used in order cover a large range of energy dissipations. The mixing time for demulsifier dispersion was varied from 2, 6 or 10, with two minutes being the shortest possible mixing time in this experimental configuration. The injection concentration was varied from 3 wt. %, 21 wt. % or 39 wt %, with 39 wt % being the stock concentration of the demulsifier as provided. The demulsifier concentration is the wt % of active agent diluted in xylenes.

Table 8 shows the detailed Box-Behnken factorial design runs. The experiments were conducted in one full design block and the order of all the experiments within the block was randomized.

3.2.1 Water Droplet Detection Image Analysis Protocol

The water droplet detection image analysis protocol discussed in Chapter 2 was used as a means to measure the water content in the diluted bitumen. This image analysis protocol provided the droplet diameter and droplet counts in each image analysed. As a result, two measures of the water droplet in the diluted bitumen were available, the average # of droplets/slide and the numerical average droplet diameter. 30 images were taken of each sample (refer to Table 6) at random locations on the microscope slide, covering approximately 80% of the sample surface on the microscope slide.

Table 8: Box-Behnken factorial design: 30 runs

Block/Variable	Bulk Concentration X_{BC}	Mixing Intensity X_{ε}	Mixing Time X_t	Injection Concentration X_{IC}
X_{BC}, X_{ε}	−1	−1	0	0
	−1	1	0	0
	1	−1	0	0
	1	1	0	0
X_{BC}, X_t	−1	0	−1	0
	−1	0	1	0
	1	0	−1	0
	1	0	1	0
X_{BC}, X_{IC}	−1	0	0	−1
	−1	0	0	1
	1	0	0	−1
	1	0	0	1
X_{ε}, X_t	0	−1	−1	0
	0	−1	1	0
	0	1	−1	0
	0	1	1	0
X_{ε}, X_{IC}	0	−1	0	−1
	0	−1	0	1
	0	1	0	−1
	0	1	0	1
X_t, X_{IC}	0	0	−1	−1
	0	0	−1	1
	0	0	1	−1
	0	0	1	1
Central Design Control Runs	0	0	0	0
	0	0	0	0
	0	0	0	0
	0	0	0	0
	0	0	0	0
	0	0	0	0

3.3 Results and Discussion: Campaign 1

Figure 16 shows the normalized droplet size distribution plot for a central design run. This droplet size distribution is representative of all 30 runs conducted in Campaigns 1 & 2. It can be observed that the peak distribution for all sampling points lies at a 4 µm droplet diameter. This is a result of dynamic settling and coalescence rates that are occurring in the system. The rate of coalescence of the droplets is higher than the settling rate of the larger droplets, as a result, the peak distribution remains at 4 µm throughout all 30 minutes of settling. Table 9 shows the terminal settling velocities calculated for different sized water droplets. It can be seen that a 4 µm droplet will require approximately 3 minutes to settle 32 mm (i.e. water droplet from liquid surface settling out of sampling range). This means that the smallest droplets require less than 3 minutes to coalescence into 4 µm droplets, maintaining the peak distribution throughout the entire experiment. These settling velocities are calculated assuming unhindered settling of individual water droplets.

Due to equipment limitations, droplets smaller than 2 µm could not be detected and as a result, there is no information regarding the population of the smaller droplets. It is highly possible that there is another peak in the droplet diameter distribution lying further down in the smaller diameter range. This would account for the formation of larger droplets through coalescence, maintaining the peak distribution at 4 µm throughout the experiment.

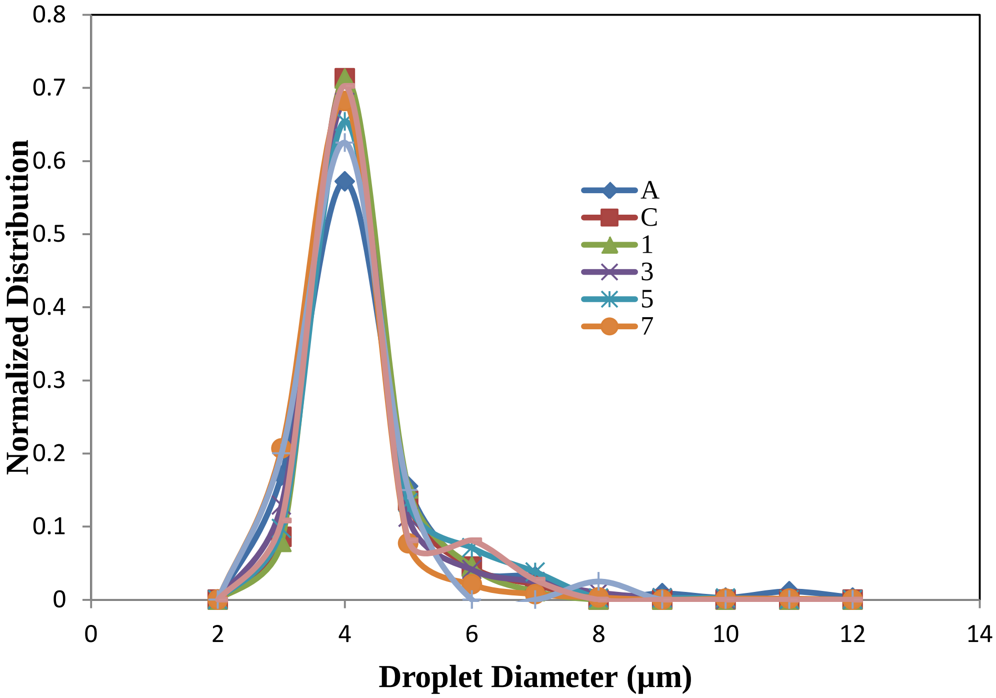

Figure 16: Normalized Droplet Size Distribution Plot; Variable order: (BC, ε, t, and IC); Sampling time: (refer to **Table 6**)

Table 9: Theoretical Settling Velocities for Water Droplets

Water Droplet Diameter (μm)	Re	Flow Regime	C_D	v_s (mm/min)	32 mm Settling Time (min)	230 mm Settling Time (min)
2	0.0171	Stokes	1410	2.77	11.56	83.10
3	0.0576	Stokes	416	6.23	5.14	36.94
4	0.137	Stokes	176	11.1	2.89	20.78
5	0.267	Stokes	90.0	17.3	1.85	13.30
6	0.416	Intermediate	56.6	25.4	1.26	9.06
7	0.651	Intermediate	36.8	34.0	0.94	6.76
8	0.955	Intermediate	25.5	43.7	0.73	5.26
9	1.34	Intermediate	18.6	54.3	0.59	4.24
10	1.79	Intermediate	14.1	65.7	0.49	3.50
20	11.2	Intermediate	2.89	205	0.16	1.12
30	29.3	Intermediate	1.43	357	0.09	0.64
40	55.3	Intermediate	0.95	506	0.06	0.45
50	89.0	Intermediate	0.72	651	0.05	0.35

**Calculated using* ρ_B*=860 (kg/m3),* ρ_w *=971 (kg/m3),* μ_B*= 5E-06 Pa·s*

Figure 17 shows the numerical average droplet diameter for the experimental runs with a low demulsifier injection concentration (X_{IC} = -1). It can be seen that the average droplet diameter stays relatively constant, as can be seen from Figure 16. This is the same for all experimental runs performed in Campaigns 1 & 2. This means that the average # of droplets/slide is representative of the water content in the diluted bitumen.

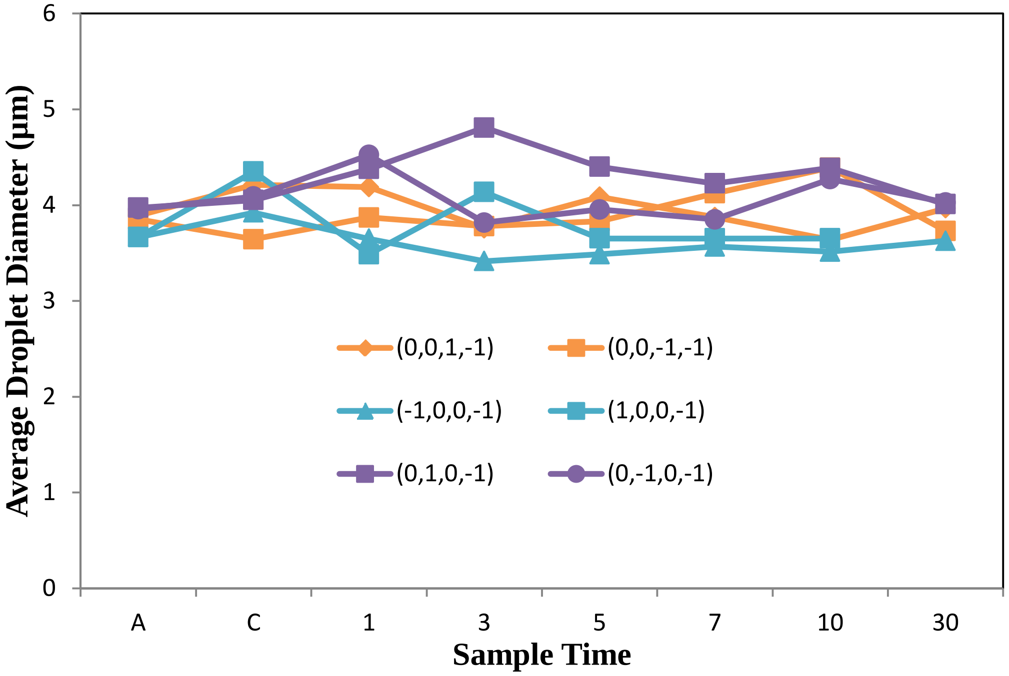

Figure 17: Average Droplet Diameter for low injection concentration runs; Variable order: (BC, ε, t, and IC); Sample time: (refer to **Table 6**)

Figure 18 shows the coefficients of the main effects (β_{BC}, β_{ε}, β_t and β_{IC}) obtained from the fractional factorial design. These coefficients are obtained by subjecting the droplet data to the following 4-factor multiple linear regression analysis equation:

$$
\begin{aligned}
\mathrm{C}(t) &= \beta_0 + \beta_{BC}X_{BC} + \beta_{\varepsilon}X_{\varepsilon} + \beta_t X_t + \beta_{IC}X_{IC} \\
&+\beta_{BC^2}X_{BC}^2 + \beta_{\varepsilon^2}X_{\varepsilon}^2 + \beta_{t^2}X_t^2 + \beta_{IC^2}X_{IC}^2 \\
&+\beta_{BC\cdot\varepsilon}X_{BC}X_{\varepsilon} + \beta_{BC\cdot t}X_{BC}X_t + \beta_{BC\cdot IC}X_{BC}X_{IC} \\
&+\beta_{\varepsilon\cdot t}X_{\varepsilon}X_t + \beta_{t\cdot IC}X_tX_{IC} + \beta_{\varepsilon\cdot IC}X_{\varepsilon}X_{IC}
\end{aligned}
\tag{28}
$$

where C(t) represents the number of average # of droplets/slide

β_A represents the regression coefficients for the variables BC, ε, t and IC

and X_A represents the coded levels of the variables BC, ε, t and IC

It can be seen from Figure 18 that the injection concentration has a very strong positive impact on C(t), meaning that a higher IC will produce a higher # of droplets/slide and a lower IC will mean otherwise. On the other hand, BC has a very strong negative impact, so a high BC will produce a lower # of droplets/slide and a low BC will produce a higher # of droplets/slide. It can also be observed from Figure 18 that IC has a larger impact on the # of droplets/slide in the early stages of settling compared to the other three variables. The regression coefficients of the other two variables, ε & t, are insignificant as their 95% confidence intervals include the zero value.

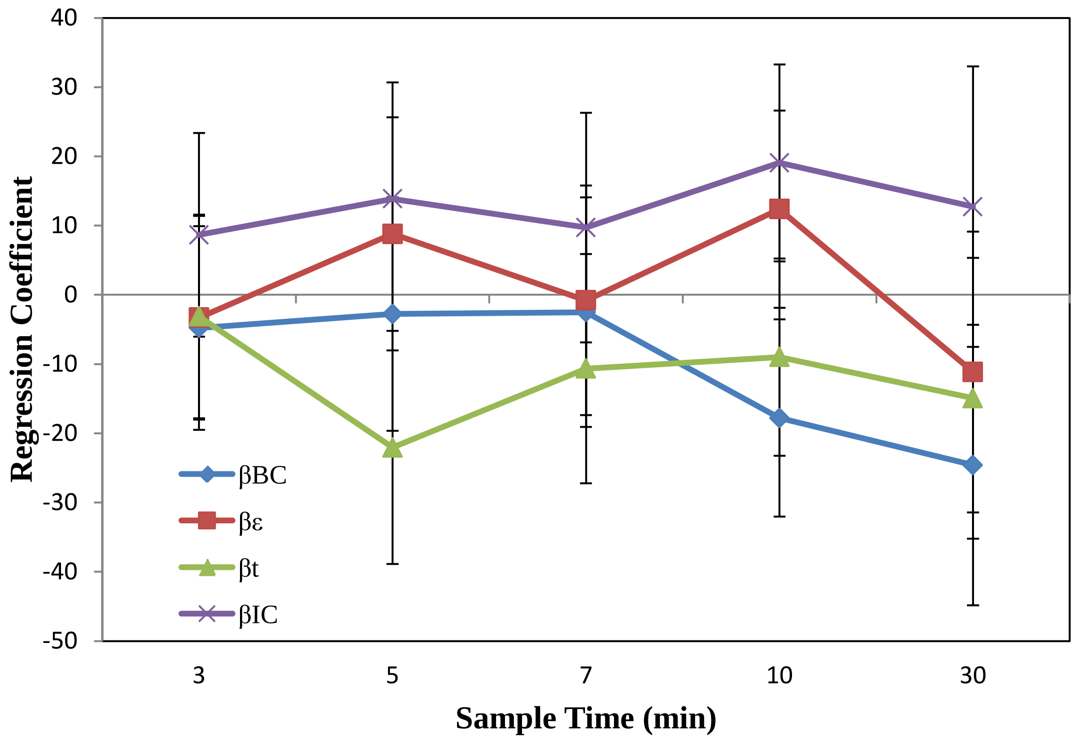

Figure 18: Main Effects Regression Coefficients for Campaign 1; Sample time: (refer to **Table 6**)

Figure 19 shows the regression coefficients for the quadratic effects (β_{BC^2}, β_{ε^2}, β_{t^2} and β_{IC^2}) and Figure 20 shows the regression coefficients for the interaction effects ($\beta_{BC\cdot\varepsilon}, \beta_{BC\cdot t}, \beta_{BC\cdot IC}, \beta_{\varepsilon\cdot t}, \beta_{t\cdot IC}$, and $\beta_{\varepsilon\cdot IC}$). It can be seen that there is no noticeable trend and that both the quadratic effects and interaction effects are insignificant when compared to the main effects. These results agreed with those found by Chong in a similar study performed where the water wt. % in the samples were measured (Chong, 2012).

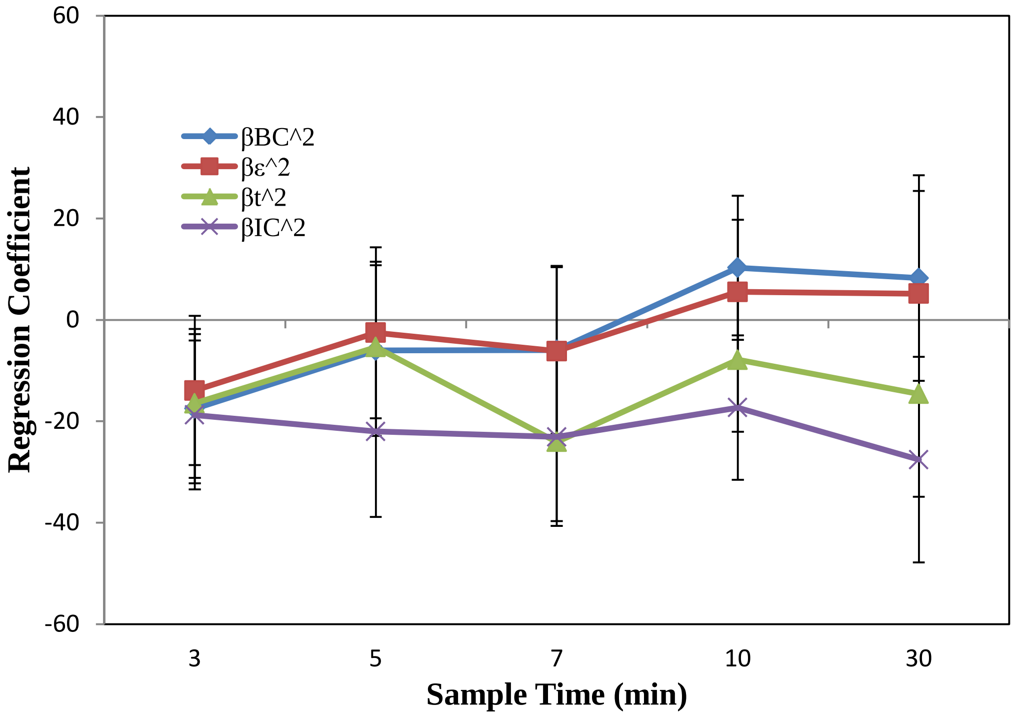

Figure 19: Quadratic Effects Regression Coefficients for Campaign 1; Sample time: (refer to **Table 6**)

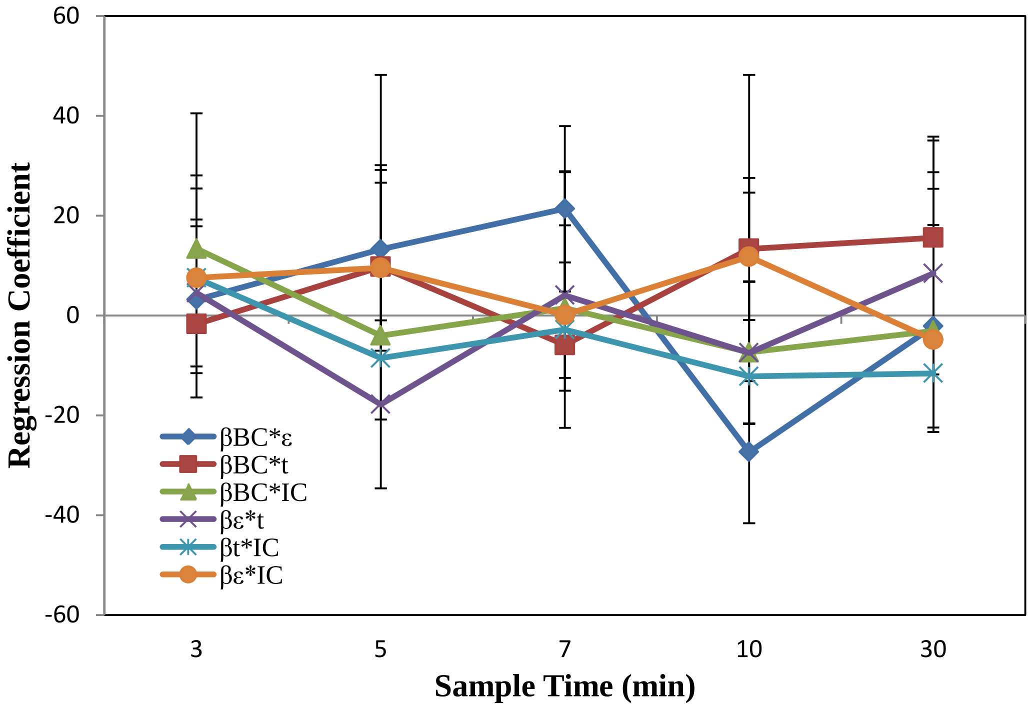

Figure 20: Interaction Effects Regression Coefficients for Campaign 1; Sample time: (refer to **Table 6**)

Figure 21, Figure 22 and Figure 23 show the average # of droplets per microscope slide taken at different sample points. Figure 21 shows the results from the central design runs. Every can of pre-mixed bitumen allows for two experiments to be carried out, these paired runs share the same value at sample point A and are color coded in pairs. As can be seen in Figure 21, the values for the average # of droplets/slide vary greatly from sample points C to 10, even for the paired experiments. This is due to the dynamic settling and coalescence rates. However, at the end of the experiment (30 minutes after settling), the values obtained from the same day's experiments are within their 95% confidence interval. This represents the reproducibility of the results obtained.

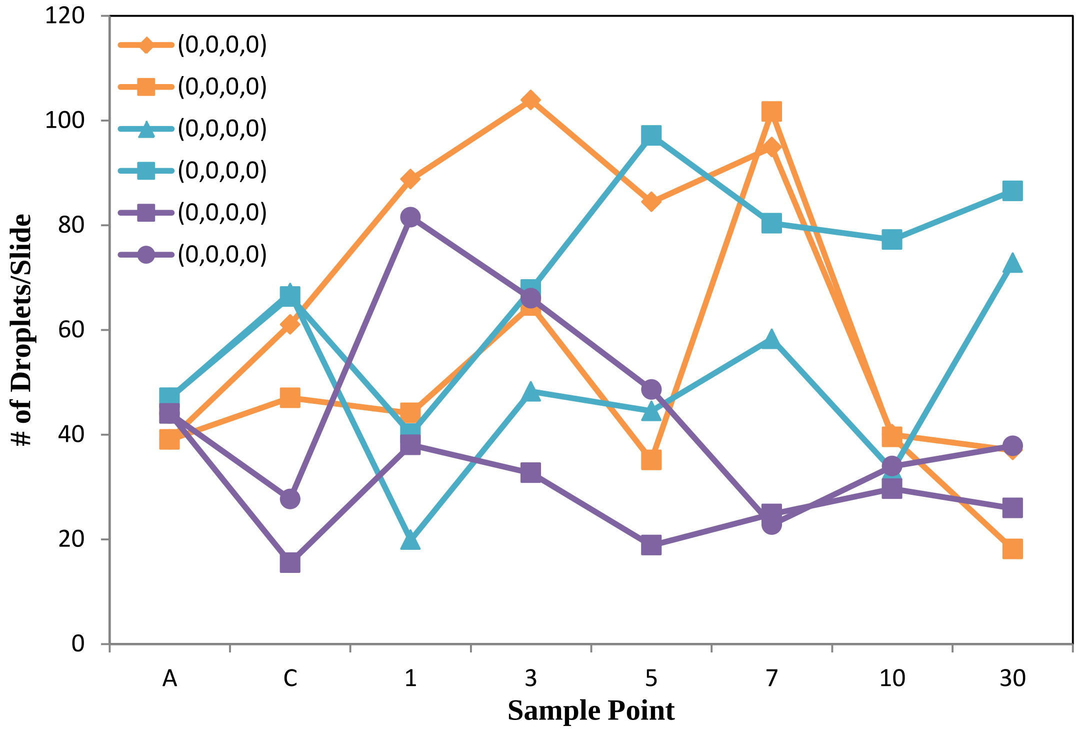

Figure 21: #of Droplets/Slide for Central Point Experimental Runs Variable order: (BC, ε, t, and IC) ; Sample time: (refer to **Table 6**)

Figure 22 shows the results from the experimental runs where a low injection concentration was used (X_{IC} = -1). All runs had an average # of droplets/slide value below 20 after 30 minutes of settling), with the best run (1,0,0,-1) having zero droplets/slide after 30 minutes. When doing the fractional factorial design of experiments, the experiment schedule was organized in such a way that each paired run would vary by only one variable. However, due to equipment limitations, the experiments for variables (0, 1, 0, -1) and (0, -1, 0,-1) were carried out on different days. This resulted in them having different values at sample point A.

As can be seen from Figure 22, for runs (0, 0, 1,-1) and (0, 0, -1, -1), a longer mixing time t resulted in a lower # of droplets/slide. For runs (-1, 0, 0, -1) and (1, 0, 0, -1), the run with a high bulk concentration BC also resulted in a much lower # of droplets/slide. This represents the effect of BC and t on the #of droplets/slide and in general, the amount of water droplets present in the system (based on the conclusion from Figure 17 that # of droplets/slide represents the water content present in the system). For runs (0, 1, 0, -1) and (0, -1, 0, -1), the run with the lower mixing ε had a lower # of droplets/slide. It can also be observed that the # of droplets/slide in all the experimental runs with a low IC decreased at a faster rate as compared to all other experimental runs. The differences in the # of droplets/slides in these six runs are relatively small compared to the differences between the other runs where IC was not set at the lower value. These results all agree with a separate study carried out by Chong (Chong, 2012).

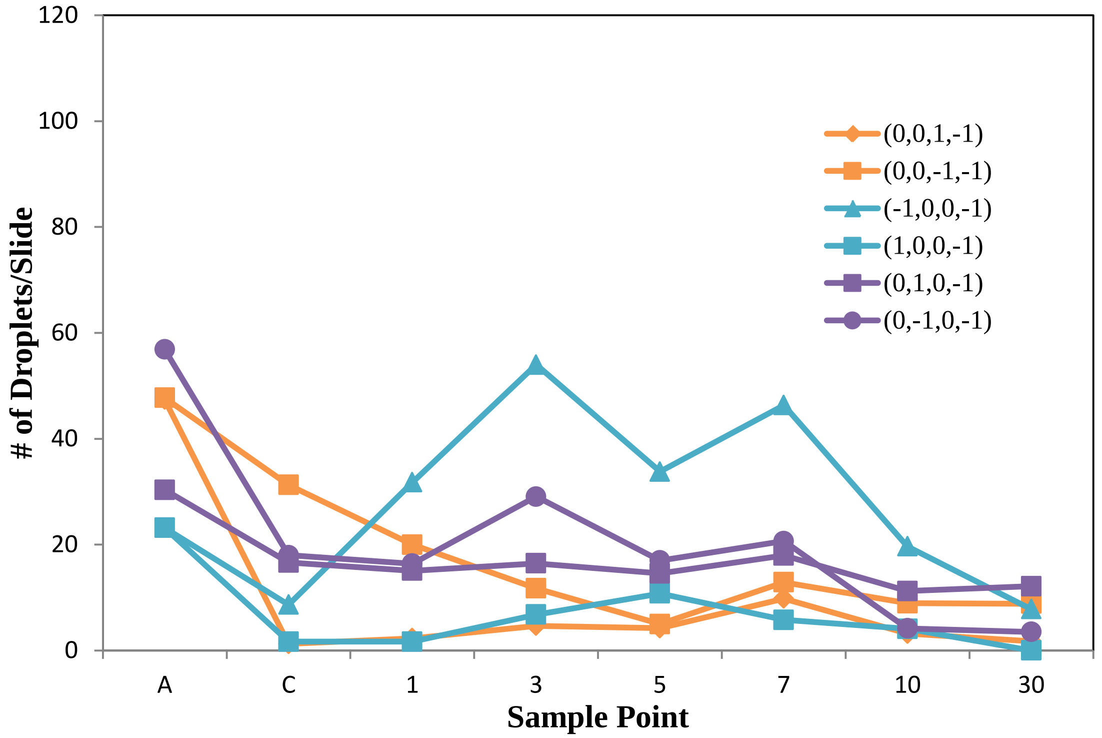

Figure 22: #of Droplets/Slide for Experimental Runs with Low Injection Concentration; Variable order: (BC, ε, t, and IC) ; Sample time: (refer to **Table 6**)

Figure 23 shows the # of droplets/slide for the experimental run with a high injection concentration IC. It can be seen that the best two runs, (0, 1, 0, 1) and (1, 0, 0, 1) were within the range of the low injection concentration runs. However, the data in general shows that a low injection concentration produces better results than a high injection concentration. This proves the fact that injection concentration has a very strong effect on the final water content of the system. It is also observed that mixing time has an effect on the # of droplets/slide. Runs (0, 0, 1, 1) and (0, 0, -1, 1) have a difference in their final water content.

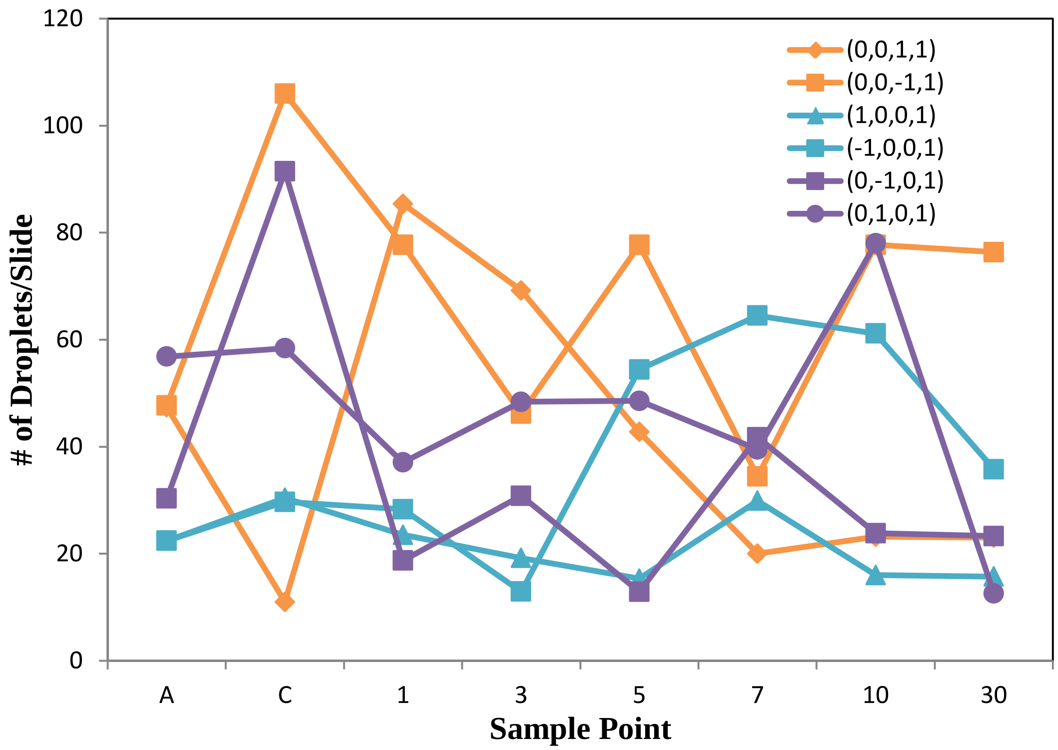

Figure 23: #of Droplets/Slide for Experimental Runs with High Injection Concentration; Variable order: (BC, ε, t, and IC) ; Sample time: (refer to **Table 6**)

From Figure 21 and Figure 22, it can also be observed that runs with a high bulk concentration BC ended up with a lower water droplet count when compared to their counterparts. From these figures, it can be concluded that IC and BC have the strongest effects on the final water content in the system. ε and t both have effects on the final water content as well, but are overshadowed by the effects of IC and BC when IC and BC are at the optimal values. As a result, a second experimental campaign was performed to determine the effects of ε and t when BC and IC are in the optimal range of values.

3.3.1 Solids Behavior

Other effects of having a low demulsifier injection concentration were observed. Figure 24 shows the micrographs of a central design run and a run with a low injection concentration (1, 0, 0, -1) taken 30 seconds before mixing ends (sample time C) at 100 times magnification. Figure 24 (a)-(b) represent the sample taken from the central design run and Figure 24 (c)-(d) represent the sample taken from the low injection concentration run. It can be observed that the solids in the sample from the low injection concentration run exhibited flocculating behavior, while the solids in the central design run were randomly dispersed. Figure 24 (a)-(b) are representative of all the runs that did not have a low injection concentration. This meant that injection concentration affects not only the water droplet behavior, but also the solids behavior as well. This behavior is observed in all runs that had a low injection concentration and Figure 24 (c)-(d) is representative of it.

Figure 25 shows the micrographs of the same two samples, taken at a later sampling time (5 minutes after settling). Figure 25 (a)-(b) represents the central design run while Figure 25 (c)-(d) represents the low injection concentration run. It is observed that Figure 25 (c)-(d) has fewer solids present when compared to Figure 25 (a)-(b) as the solid flocs would have settled out during this time. Flocs of water droplets can also be spotted in Figure 25 (d). This behavior of water flocculating is also observed in other experimental runs with a low injection concentration.

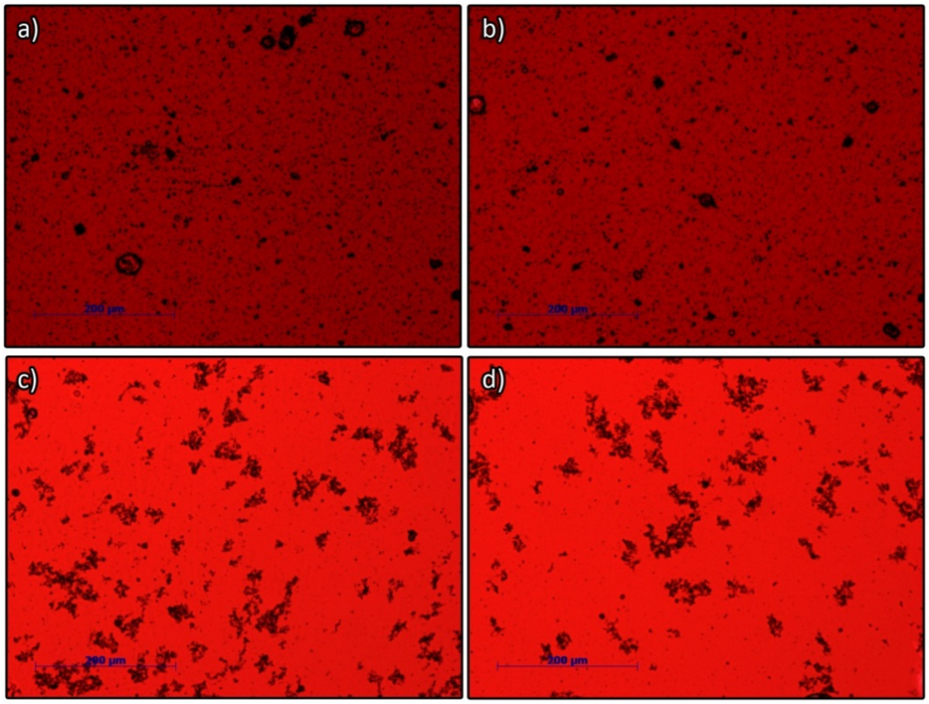

Figure 24: Micrographs taken 30 seconds before mixing ends at 100 times magnification; (a)-(b) Central Design Run, (c)-(d) Low Injection Concentration Run

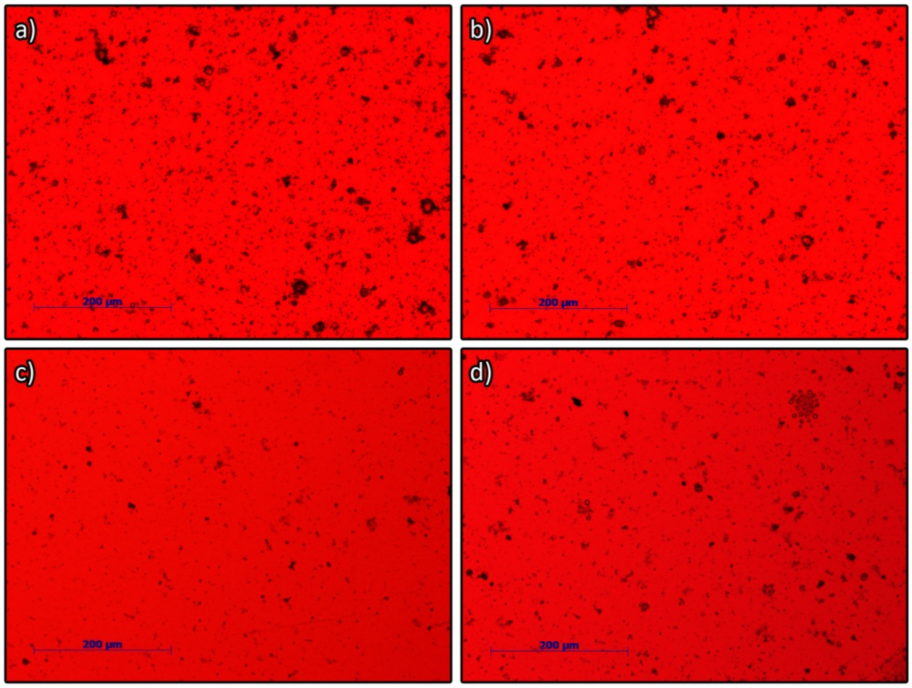

Figure 25: Micrographs taken 5 minutes into settling at 100 times magnification; (a)-(b) Central Design Run, (c)-(d) Low Injection Concentration Run

3.3.2 Flocculation of Water Droplets

It was mentioned earlier that flocs of water droplets were observed when the demulsifier injection concentration was low. Figure 26 and Figure 27 are micrographs of water droplet flocs from two different low injection concentration runs. These flocs were observed only in experimental runs that had a low demulsifier injection concentration. These flocs may explain why the water content in experimental runs with low injection concentrations decreases much more rapidly and reaches a lower water content value when compared to the other runs.

It can be concluded that the effects of demulsifier injection concentration are not limited to the water content, but also to the solids behavior and to water droplet flocculation.

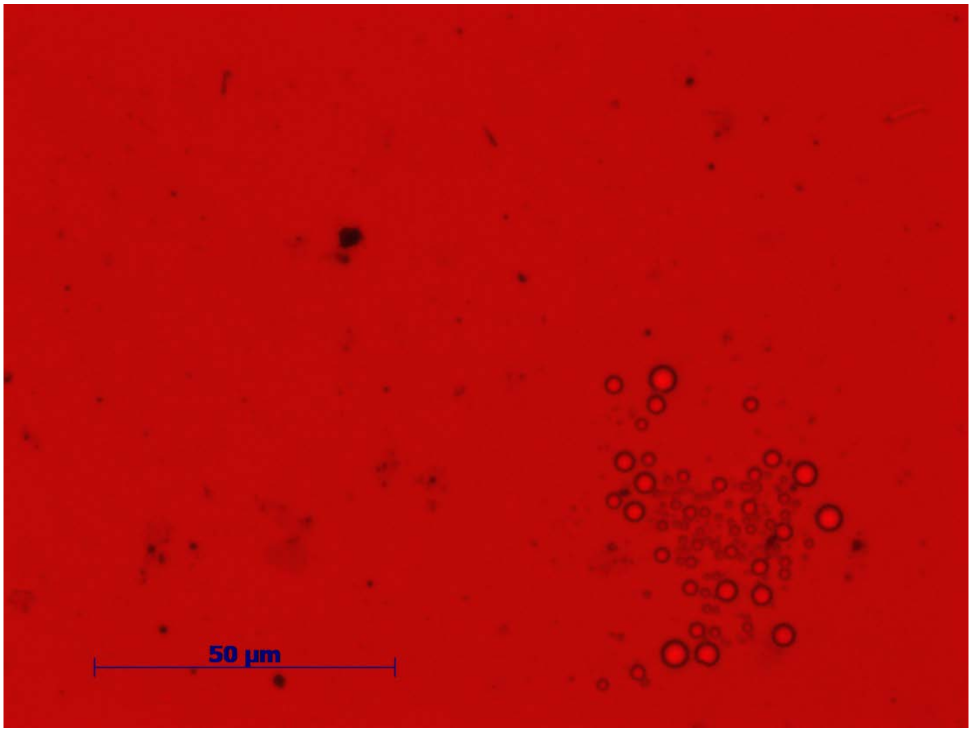

Figure 26: Micrograph of a water droplet floc taken at 40 times magnification (Low Injection Concentration)

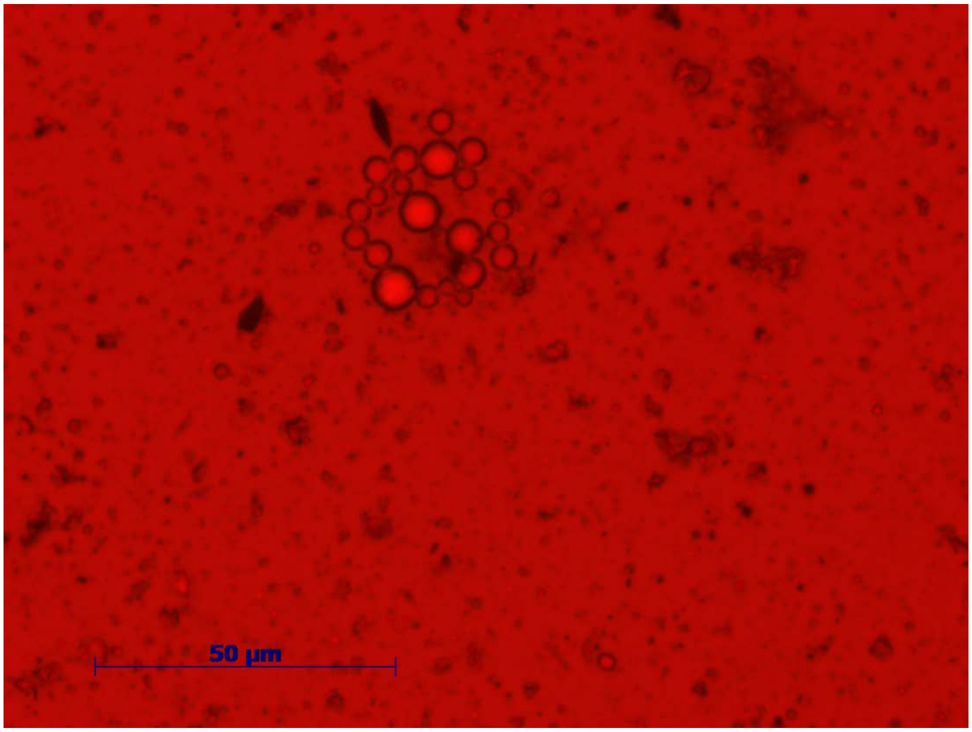

Figure 27: Micrograph of a water droplet floc taken at 40 times magnification (Low Injection Concentration)

3.3 Design of Experiments: Campaign 2

As mentioned earlier, the effects of ε and t were not clearly understood from the results in campaign 1. It is important to investigate the effects of ε and t when the system is operating under the optimal values of bulk concentration and injection concentration, which is the purpose of the second experimental campaign.

The experimental setup was identical to the first campaign, with the differences being the bitumen samples and the factorial design. The bitumen samples used in this campaign were of a different batch from Syncrude and had lower initial water content.

3.3.1 Two Level Factorial Design

It was concluded in campaign 1 that the quadratic effects were insignificant which allowed for a simple two-level factorial design of experiments. In order to reduce the number of experiments required, the mixing intensity ε and mixing time t were combined into one variable called the mixing energy:

$$J = \varepsilon \cdot t \tag{29}$$

where J is the mixing energy per mass (J/kg)

and ε and t are the mixing intensity (W/kg) and mixing time (s) respectively.

This new variable allowed for us to study the combined effects of mixing while reducing the amount of experiments required.

The range of values for the demulsifier bulk concentration and injection concentration were also modified to fit the optimal values obtained from campaign 1. Table 10 shows the values for the variables used in this two-level factorial design and Table 11 shows the details of the experimental runs. It was determined from the first campaign that a bulk concentration of 50 ppm was sufficient to reduce the final water content to optimal levels when the injection concentration was sufficiently low.

It was determined in campaign 1 that an injection concentration of 3 wt. % produced better results when compared to 21 wt. %. In order to narrow down the range in which the injection concentration can be classified as “low enough”, a new range of injection concentrations was selected in this campaign. The low limit of the injection concentration was kept at 3 wt. % and the midpoint between

3% and 21% was selected to be the new upper limit. This resulted in an injection concentration range of 3 to 12 wt. %.

As this is a two-level factorial design, each variable was varied at two levels. The different levels were coded according to equally spaced intervals using Equation (2). This formula results in two coded levels of -1 and +1 for each variable as see in Table 10.

Table 10: Variables for the Two-Level Factorial Design used in Campaign 2

Variable	-1	1
Demulsifier Bulk Concentration, X_{BC} (ppm)	27	50
Mixing Energy, J (J/kg)	120*	24000**
Injection Concentration, X_{IC} (wt. %)	3	12

*ε = 1 W/kg, t = 2 min

**ε = 40 W/kg, t = 10 min

Table 11: Two-Level Factorial Design Experimental Runs

Run #	Bulk Concentration X_{BC}	Mixing Energy X_J	Injection Concentration X_{IC}
1	−1	−1	-1
2	−1	-1	1
3	-1	1	-1
4	-1	1	1
5	1	1	1
6	1	1	-1
7	1	-1	1
8	1	-1	-1

3.3.2 Results and Discussion: Campaign 2

Figure 28 shows the droplet size distributions for Run #1. It can be seen that the same peak at the 4 μm diameter size is observed. This is consistent with the results observed from the first campaign, even though the bitumen samples were from different batches. The other seven runs produced droplet size distributions with similar size distributions.

Figure 29 shows the regression coefficients for the main effects in campaign 2 (β_{BC}, β_J and β_{IC}). These coefficients are obtained by subjecting the droplet data to the following 3-factor multiple linear regression analysis equation:

$$\mathrm{C}(t) = \beta_0 + \beta_{BC}X_{BC} + \beta_J X_J + \beta_{IC}X_{IC} \qquad (30)$$

$$+\beta_{BC\cdot J}X_{BC}X_J + \beta_{J\cdot IC}X_J X_{IC} + \beta_{BC\cdot IC}X_{BC}X_{IC}$$

where C(t) represents the number of average # of droplets/slide

β_A represents the regression coefficients for the variables BC, J and IC

and X_A represents the coded levels of the variables BC, J and IC

This regression equation is similar to the one used in campaign 1, with the a different number of variables and the absence of quadratic effects in this equation.

It can be seen from Figure 29 that injection concentration still has a strong positive effect on the final # of droplets/slide and that the mixing energy, J, has a strong negative effect on the final (30 minutes after settling) # of droplets/slide. A high positive coefficient meant that a low value of the variable will result in a low C(t) and a negative coefficient meant that a high value of the variable will also result in a low C(t) as based on Equation (30). The conclusion obtained from this figure agrees with campaign 1 in regards to the effect which IC has on the # of droplets/slide at the end of the experiment. This effect of mixing was not observed in campaign 1 where the range of the bulk concentration and injection concentration were not within the ideal range. This is different from the conclusion drawn in campaign 1, which concluded that the mixing variables (ε and t) had no significant effects. Another interesting result from this figure is that the effect of bulk concentration is negligible compared to that of injection concentration IC and mixing energy J. Once again, this differs from campaign 1 which suggested that the bulk concentration and injection concentration had the most significant effect on the final # of droplets/slide. This proves the earlier hypothesis that the lumped mixing energy variable, J, has a significant effect on the final # of droplets/slide when the value of the bulk concentration is within the optimal range.

Figure 30 shows the regression coefficients for the interaction effects ($\boldsymbol{\beta_{BC\cdot J}}$, $\boldsymbol{\beta_{J\cdot IC}}$ and $\boldsymbol{\beta_{BC\cdot IC}}$) in campaign 2. It can be seen from the figure that the interaction effect $X_{J\cdot IC}$ is almost zero negligible when compared to the values of the main coefficients. This means that having the mixing energy and injection concentration set at opposite ends (1 and -1) will not have any effect on the final # of droplet.

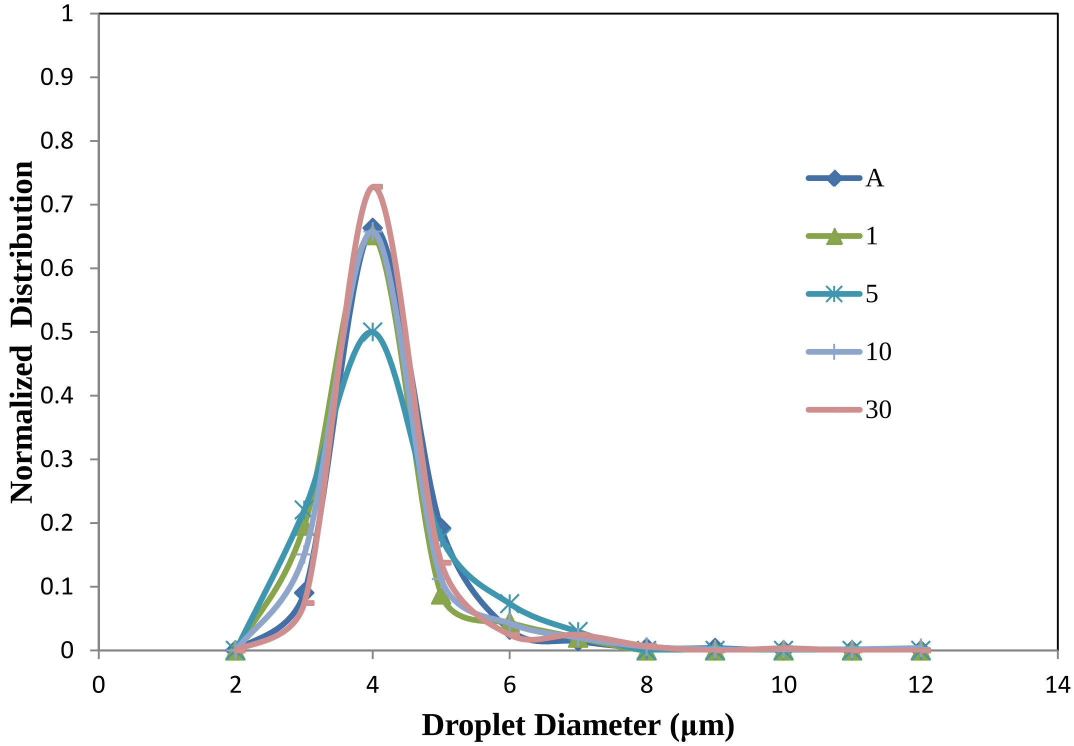

Figure 28: Normalized Droplet Size Distribution Plot for Campaign 2; Variable order: (BC, J and IC); Sample time: (refer to **Table 6**)

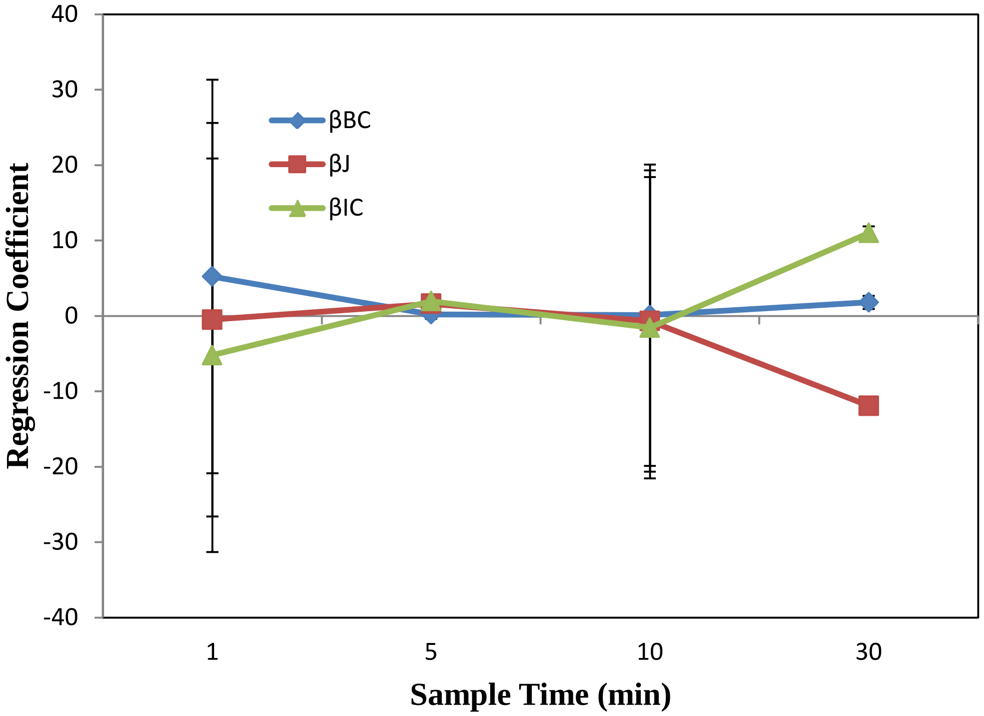

Figure 29: Main Effects Regression Coefficients for Campaign 2

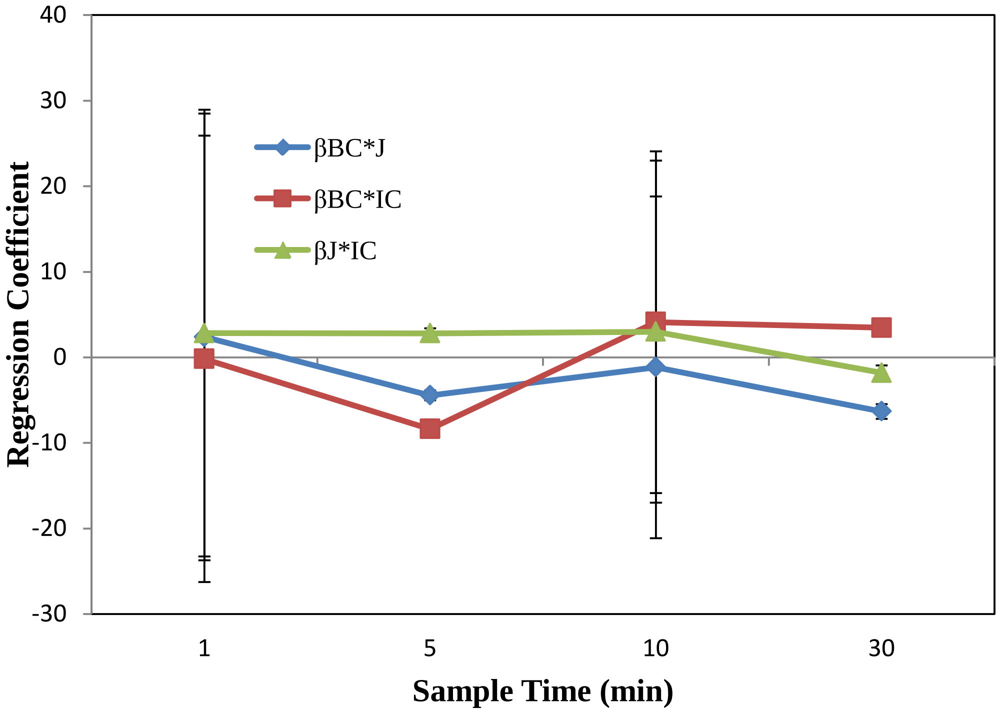

Figure 30: Interaction Effects Regression Coefficients for Campaign 1

Figure 31 shows the average # of droplets/slide for all eight runs. It can be observed that at the optimal bulk concentration and injection concentration range, the significance of the mixing energy, J, is much more prominent as compared to ε and t in campaign 1.

As in campaign 1, the experimental runs which were carried out using the same pre-mixing samples were color coded. It can be seen that the final water content was the lowest at perfect mixing conditions of (1, 1, -1) [purple circle]. The effect of J can also be observed as the run (-1, 1, 1) produced much better results when compared to the run (-1, -1, 1) [red pair]. Those two runs had the same variables with the only difference being their values for J. It can also be observed that the top four runs with the highest final # of droplets/slide all have a common factor, which is that J was at a -1 value. This supports the conclusions drawn from Figure 29, where the regression coefficients of the main effects were shown.

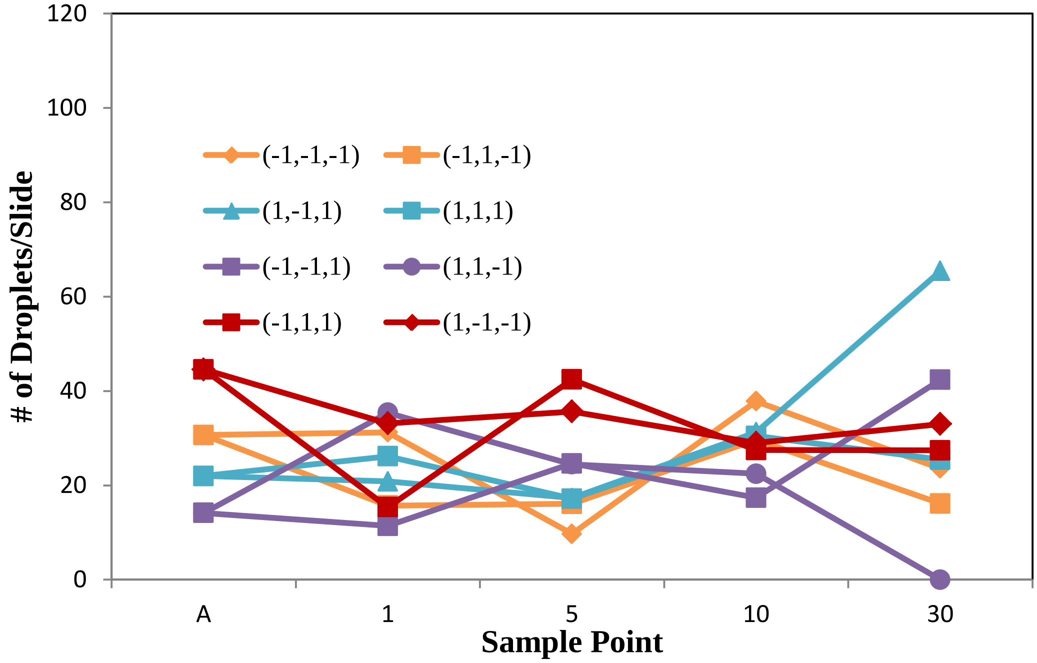

Figure 31: # of Droplets/Slide for Campaign 2; Variable Order: (BC, J, IC); Sample time: (refer to **Table 6**)

3.4 Conclusion

Two experimental campaigns were carried out to study the effects of mixing, demulsifier bulk concentration and demulsifier injection concentration on the water droplet dynamics in naphtha diluted bitumen clarification.

In the first campaign, it was observed that the demulsifier bulk concentration and injection concentration had a significant effect on the final # of droplets/slide in the bitumen system, with the mixing intensity and time having insignificant effect. It was also observed that all experiments had a constant peak in the droplet size distributions at 4 μm diameter. It would take approximately 3 minutes for a 4 μm droplet to settle from the surface and past the sample point. The competing rates of coalescence and settling explains the constant peak at 4 μm, with the rate of coalescence being faster than the rate of settling.

In the second campaign, the effect of mixing was further studied by optimizing the values for the demulsifier bulk concentration and injection concentration. It was concluded that mixing had a much more significant effect on the final # of droplets/slide when compared to Campaign 1, and that the effect of the demulsifier bulk concentration was negligible. The same droplet size distribution peak of 4 μm was also observed in Campaign 2.

When combining the results from Campaign 1 and Campaign 2, it can be concluded that demulsifier injection concentration (IC) has a significant effect on the final water content in the diluted bitumen. The “minimum” injection concentration recommended for optimal performance is 12 wt. %. Demulsifier bulk concentration also plays a significant role in determining the final water content. It was determined from Campaign 2 that a bulk concentration range of 27 to 50 ppm produced optimal results. When the diluted bitumen clarification is carried out with both the demulsifier bulk concentration and injection concentration being within the optimal range, it was observed that mixing effects (ε and t expressed as mixing energy, J) had a significant effect on the final water content of the system.

Table 12 shows the comparison between the results obtained using image analysis against the results obtained from the Karl-Fischer Titration results obtained by Chong (2013). The significance of the effects obtained from both studies were in agreement.

Table 12: Comparison of Results with Karl-Fischer Titration Results

Campaign 1 Range	**ε (W/kg)** 1 - 40	**t_m (min)** 2 - 10	**IC (wt. %)** 3 - 39	**BC (ppm)** 5 - 95
significant effect - # of droplets	✗	✗	✓	✓
significant effect - KF Water Content	✗	✗	✓	✓
Campaign 2 Range	**J (J/kJ)** 120 - 24000		**IC (wt. %)** 3 - 39	**BC (ppm)** 5 - 95
significant effect - # of droplets	✓		✓	✗
significant effect - KF Water Content	✓		✓	✗

✓ = *Variable has a significant effect*
✗ = *Variable has an insignificant effect*

Chapter 4: Effects of Mixing on Water Droplet Dynamics in Overdosing Situations in Diluted Bitumen Clarification

A third experimental campaign was carried out to study the effects of a high demulsifier bulk concentration (300 ppm) along with the mixing energy J and demulsifier injection concentration on demulsifier performance. The purpose of this study was to provide an understanding of a scenario in industry where the demulsifier does not perform as expected at high bulk concentrations. This is also referred to as overdosing of the system. Overdosing of demulsifier may result in the formations of micelles in the system and alter the demulsifier behavior. The results are a significant increase in water and solids content in the product. It was suspected that overdosing was a result of insufficient dispersion of the demulsifier which resulted in saturated local concentrations. This saturation of local concentration causes the formation of micelles which causes this overdosing effect.

4.1 Experimental Set-up

The experimental set-up used for this campaign was identical to that in the first and second campaign. The diluted bitumen was pre-heated in a heated bath and pre-mixed before being transferred into the two CISTs. The demulsifier was added directly above the upper impeller blade tip and mixing was carried out, after which the diluted bitumen sample was left to settle over 30 minutes. The sampling glassware used in this campaign was identical to those in campaigns 1 and 2. Sampling was performed 33 mm below the liquid interface. The diluted bitumen samples used in this campaign were from the same batch as those used in campaign 2.

4.2 Design of Experiments: Campaign 3

A two-level factorial design was performed to determine the impact of a high demulsifier bulk concentration on the final water content in the diluted bitumen clarification process. The demulsifier bulk concentration was kept at a constant value of 300 ppm throughout this campaign. The mixing intensity and mixing time were kept together as a lumped mixing variable J, which represents the mixing energy (J/kg), and the last variable is the demulsifier injection concentration, IC.

Table 13 shows the values of the variables used in the two-level factorial design. The range of values for the mixing energy, J, was kept the same as for Campaign 2 while the injection concentration was set at a lower value of 12 wt. % and a higher value of 39 wt. %. These values were chosen to represent both ends of the spectrum for a "high" and a "low" injection concentration. It was concluded in Chapter 3 that the difference between a 3 wt. % injection concentration and a 12 wt. % injection concentration was not significant enough to justify the extra cost required to dilute the demulsifier down to 3 wt. % in an industrial setting. This factorial design results in the following regression equation:

$$\mathrm{C}(t) = \beta_0 + \beta_J \cdot X_J + \beta_{IC} \cdot X_{IC} + \beta_{J,IC} \cdot X_J \cdot X_{IC} \tag{31}$$

where C(t) represents the number of average # of droplets/slide

β_A represents the regression coefficients for the variables J and IC

and X_A represents the coded levels of the variables J and IC

β_{BC} was not included in the regression equation as the bulk concentration was not varied throughout this study. The values for X_J and X_{IC} are the levels of the mixing power and injection concentration respectively.

Table 14 shows the details of the experimental runs performed in this campaign. Table 15 shows the details of the sampling time intervals. The different levels were coded according to equally spaced intervals using Equation (2). Sampling points were similar to that in the second campaign of experiments in Chapter 3.

Table 13: Variables in the 2-level Factorial Design for Campaign 3

Variable	-1	1
Bulk Concentration, BC (ppm)	300	300
Mixing Energy, J	Low*	High**
Injection Concentration, IC (wt. %)	12	39

*Low: ε = 1 W/kg, t = 2 min

**High: ε = 40 W/kg, t = 10 min

Table 14: Experimental Runs

Run #	Mixing Factor X_J	Injection Concentration X_{IC}
1	−1	1
2	1	-1
3	1	1
4	-1	-1

Table 15: Sampling Points

Sample Point	Time Interval
A	Initial Conditions, after pre-mixing
1, 5, 10, 30	Minutes into settling

4.2.1 Results and Discussion

4.2.1.1 Micrographs

Figure 32 to Figure **39** are sample micrographs taken at the end of settling for the four experiments carried out in this campaign. Figure 32 & Figure 33 represent Run #1, Figure 34 & Figure **35** represent Run #2, Figure 36 & Figure 37 represent Run #3 and Figure 38 &**Figure 39** represent Run #4. It can be observed that Runs #1, 3 & 4 (Figure 32, Figure 33, Figure 36-Figure **39**) had a large number of small water droplets present in the background while Run #2 (Figure 34 & Figure **35**) did not have the small water droplets present. These small droplets were not present in any of the samples from Campaigns 1 & 2. This is proposed to be an effect of overdosing of the demulsifier which resulted in the final water content in the system being above expected values as it was concluded from Campaign 1 that the demulsifier bulk concentration had a negative effect on the final water content (i.e. higher the bulk concentration, lower the final water content). This is due to the fact that the high dosage of the demulsifier was not efficiently dispersed throughout the system. This resulted in a high local concentration of demulsifier which stabilized the small water droplets, rather than destabilizing them and inducing coalescence and flocculation.

Run #1

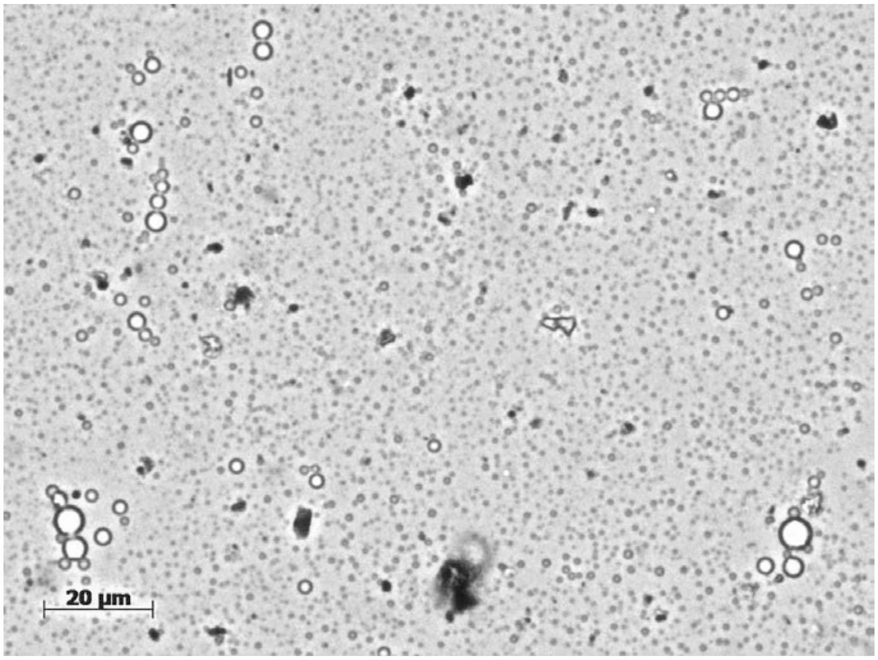

Figure 32: Micrograph after 30 minutes of Settling (-1, 1); *Variable order (J, IC)*

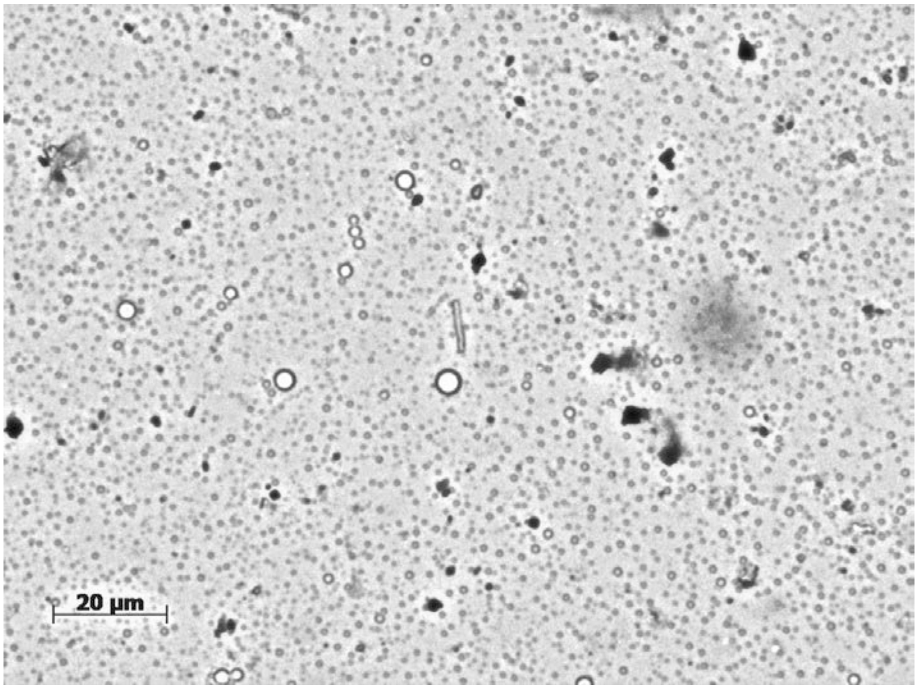

Figure 33: Micrograph after 30 minutes of Settling (-1, 1); *Variable order (J, IC)*

Run #2

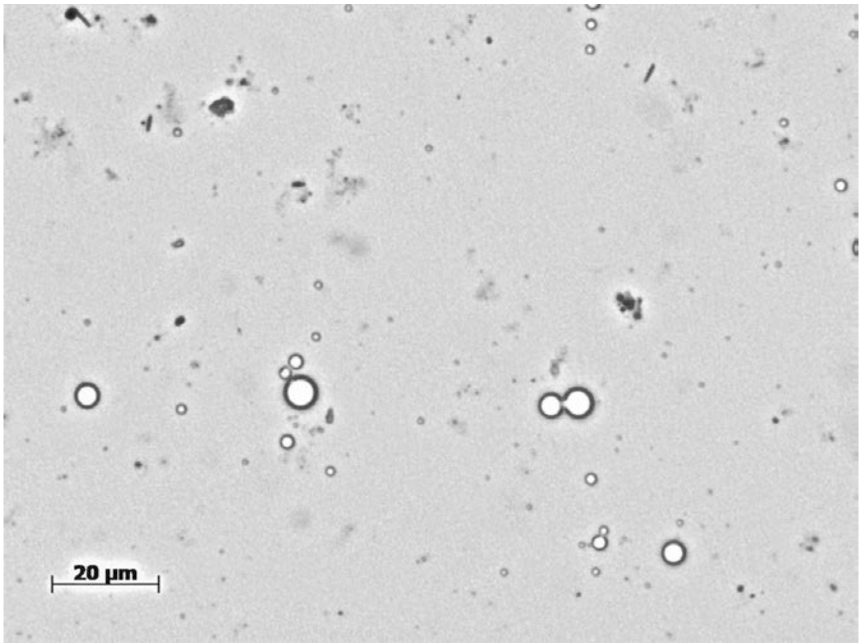

Figure 34: Micrograph after 30 minutes of settling (1, -1); *Variable order (J, IC)*

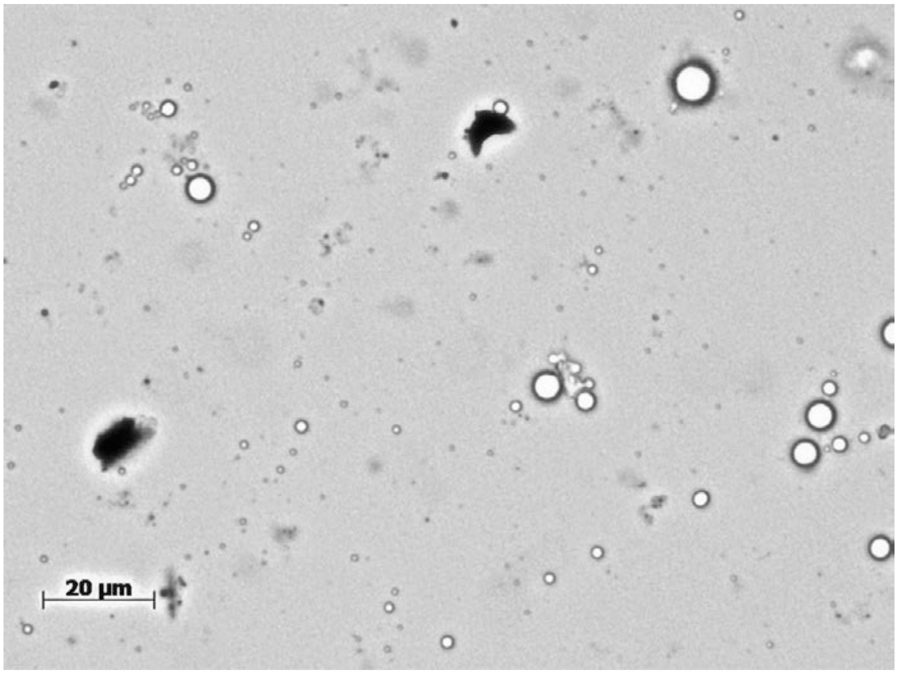

Figure 35: Micrograph after 30 minutes of settling (1, -1); *Variable order (J, IC)*

Run #3

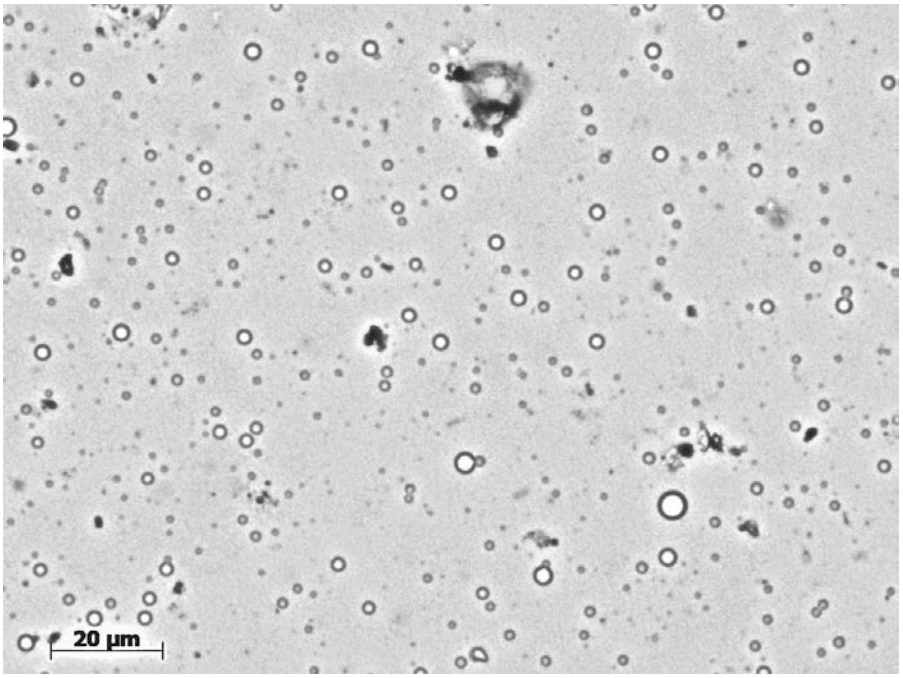

Figure 36: Micrograph after 30 minutes of settling (1, 1); *Variable order (J, IC)*

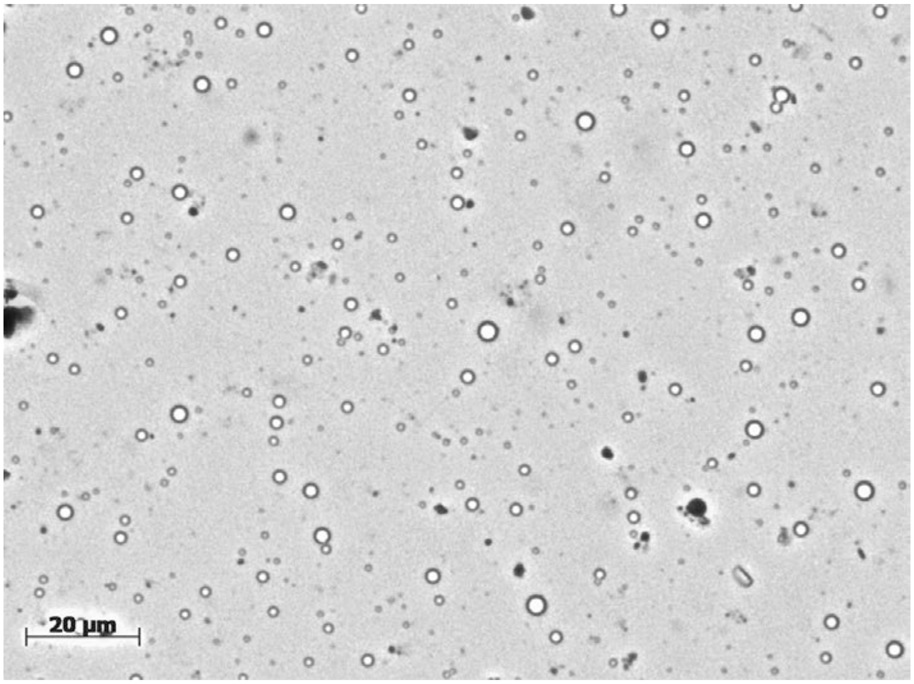

Figure 37: Micrograph after 30 minutes of settling (1, 1); *Variable order (J, IC)*

Run #4

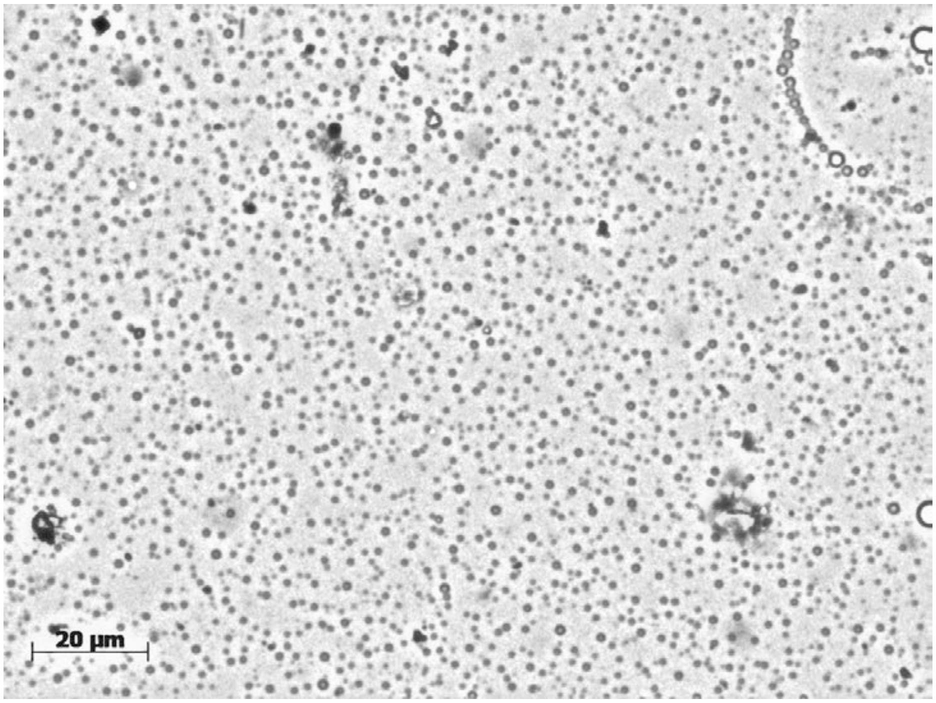

Figure 38: Micrograph after 30 minutes of settling (-1, -1); *Variable order (J, IC)*

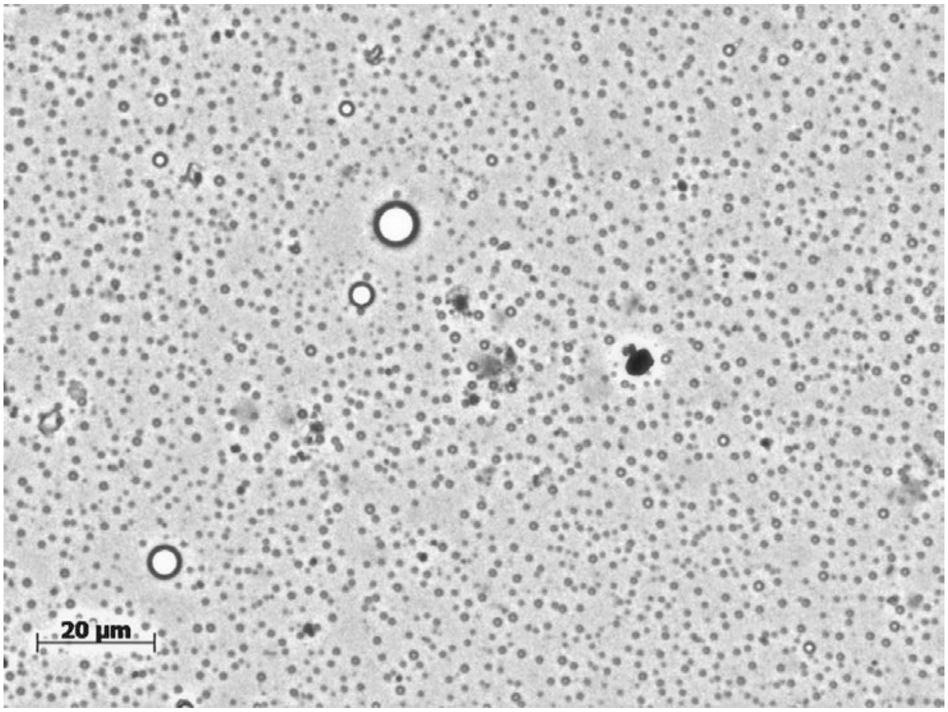

Figure 39: Micrograph after 30 minutes of settling (-1, -1); *Variable order (J, IC)*

The effects of the demulsifier injection concentration and the mixing energy can be observed from the above figures. Run #3 (Figure 36 & Figure 37; [-1 1]) had less water droplets present in the micrographs when compared to Runs #1 (Figure 32 & Figure 33; [1 1]). The only different variable between these two runs is the mixing energy J. It can be seen that a higher mixing energy J resulted in fewer small water droplets in the system. This means that the mixing energy is important in reducing the effects of overdosing. The expected effect of injection concentration observed in campaigns 1 & 2 was not observed when comparing Run #1 (Figure 32 & Figure 33; [-1 1]) and Run #4 (Figure 38 & Figure **39**; [-1 -1]). It can be seen from the figures that Run #4 contained a higher number of small water droplets as compared to Run #1. The only difference between these two runs was the injection concentration. However, the difference between Runs #1 & 3 is greater than the differences between Runs #1 & 4. These observations mean that the mixing energy has an effect to the degree of which overdosing will affect the system but the effect of injection concentration is not significant enough to overcome inadequate mixing (low mixing energy).

Run #2 (Figure 34 & Figure **35**; [1 -1]) had a high value for the mixing energy and a low injection concentration. According to the conclusion drawn from the previous paragraph and previous campaigns, Run #2 should produce the smallest amount of small water droplets. It was observed that the small water droplets that were present in Runs #1, 3 & 4 were not present in Run #2. This means that when both variables are within optimal values (a high mixing energy and a low injection concentration), the effect of overdosing is negated. This also meant that the effect of injection concentration is only significant when there is good mixing. This is similar to the conclusion drawn from Campaign 2 where it was determined that the effect of the mixing energy was significant only when the demulsifier bulk concentration is within an optimal range of values.

4.2.1.2 Droplet Size Distributions

Figure 40 to Figure 43 show the normalized droplet size distributions for Runs 1 to 4 respectively. It can be observed that Figure 40, Figure 42 and Figure 43 all have a shift from the 4 µm peak (as observed in Chapter 3) to the 2 µm peak 10 minutes after mixing ended. The shift from the 4 µm peak to the 2 µm peak meant that the majority of the water droplets present were smaller than the usual 4 µm, exhibiting the effect of overdosing. However, Figure 41 maintained the 4 µm peak throughout the experiment and did not show any signs of overdosing.

Figure 44 shows the regression coefficients for the main effects on the # of water droplets/slide for this campaign. It can be seen that the mixing energy, X_J, has a slightly more significant effect on the final # of droplets/slide when compared to the injection concentration. This agrees with the observations obtained from Chapter 3, as well as the conclusions obtained from Figure 32 to Figure 43. Figure 45 shows the interaction effects of the mixing energy X_J as well as the injection concentration X_{IC}. It can be seen that there is a significant interaction effect between X_J and X_{IC} as expected. A negative value for X_{IC} and a positive value for X_J is needed in order to lower the number of droplets/slide. The effect of this combination is greater than that of a positive X_{IC} and a negative X_J as it was shown earlier in Figure 44 that β_J was greater than β_{IC}.

Figure 46 shows the # of droplets/slide for all four experiments. It can be noted that the run with variables [1, -1] had a much lower final # of droplets/slide when compared to the other three runs. It can also be observed that the mixing energy has an effect on the final # of droplets/slide, with the run [1, 1] having a lower final # of droplets/slide compared to the run [-1. 1]. Figure 47 shows the average water droplet diameter for all four experiments. Once again, it can be observed that the experimental run with good mixing and a low injection concentration [1, -1] had an average water droplet diameter of 4 µm while the other three experimental runs had an average water droplet diameter of approximately 2 µm.

It can be concluded that overdosing occurs at high levels of bulk concentration. Injection concentration was not seen to have a significant effect on its own compared to mixing, however, when good mixing is coupled with a low injection concentration, the effects of overdosing were completely negated, allowing the demulsifier to perform as expected. This meant that the injection concentration was significant only when there is good mixing, in the case of overdosing. This is similar to the conclusions obtained from Chapter 3, where the effect of mixing is only observed when the demulsifier bulk concentration is within the optimal range.

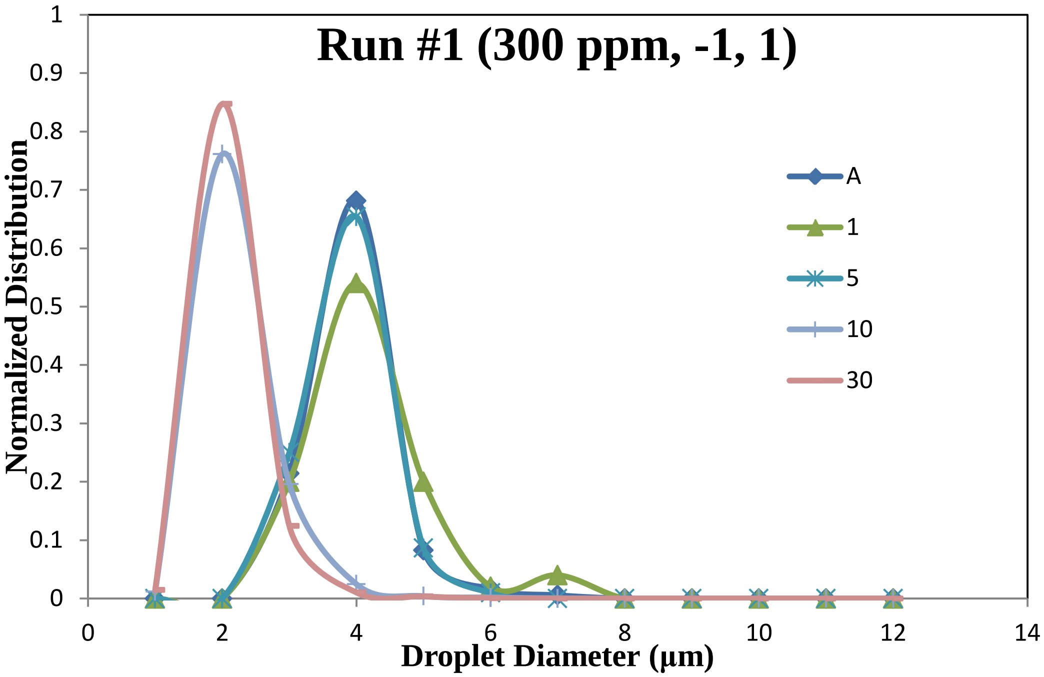

Figure 40: Droplet Size Distribution for low mixing and high injection concentration.
Variable Order: BC, J, IC

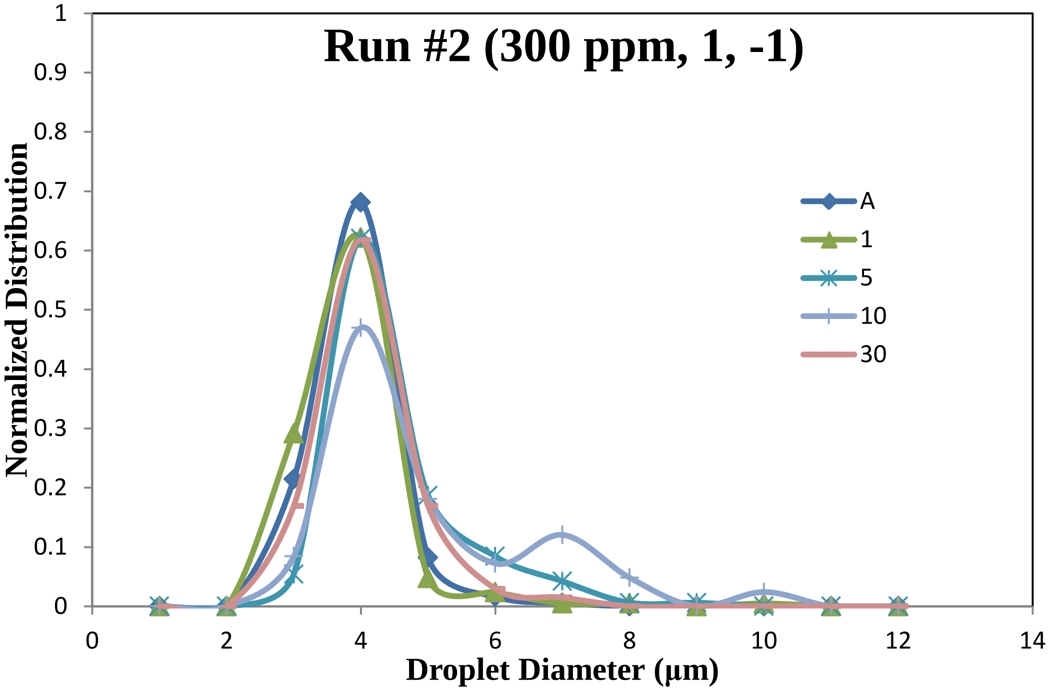

Figure 41: Droplet Size Distribution for high mixing and low injection concentration.
Variable Order: BC, J, IC

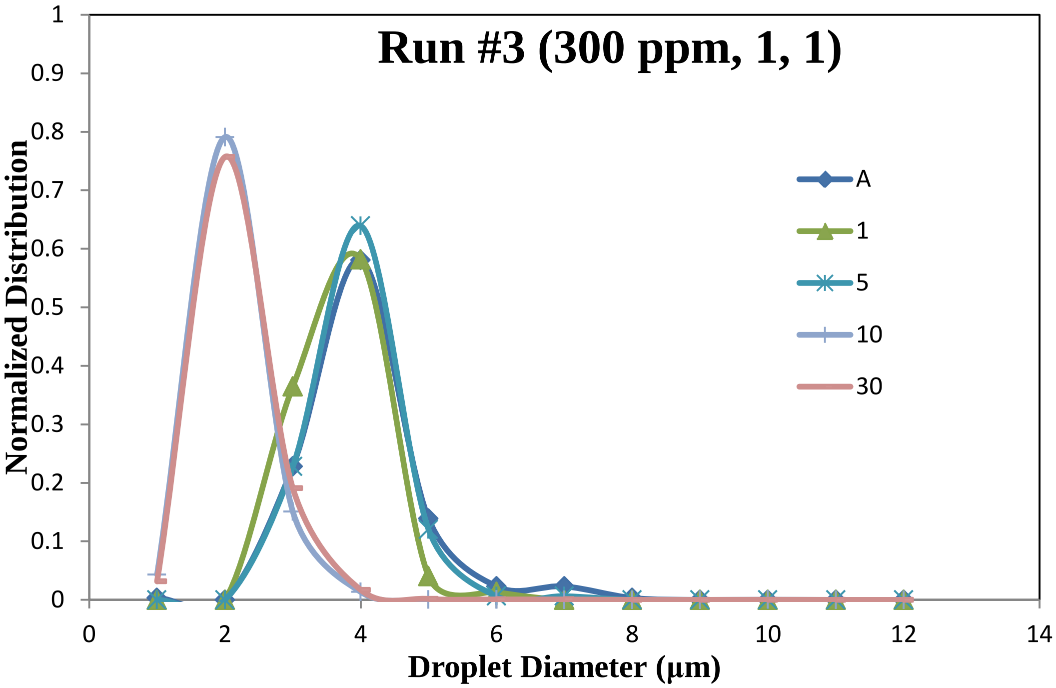

Figure 42: Droplet Size Distributions for high mixing and high injection concentration.
Variable Order: BC, J, IC

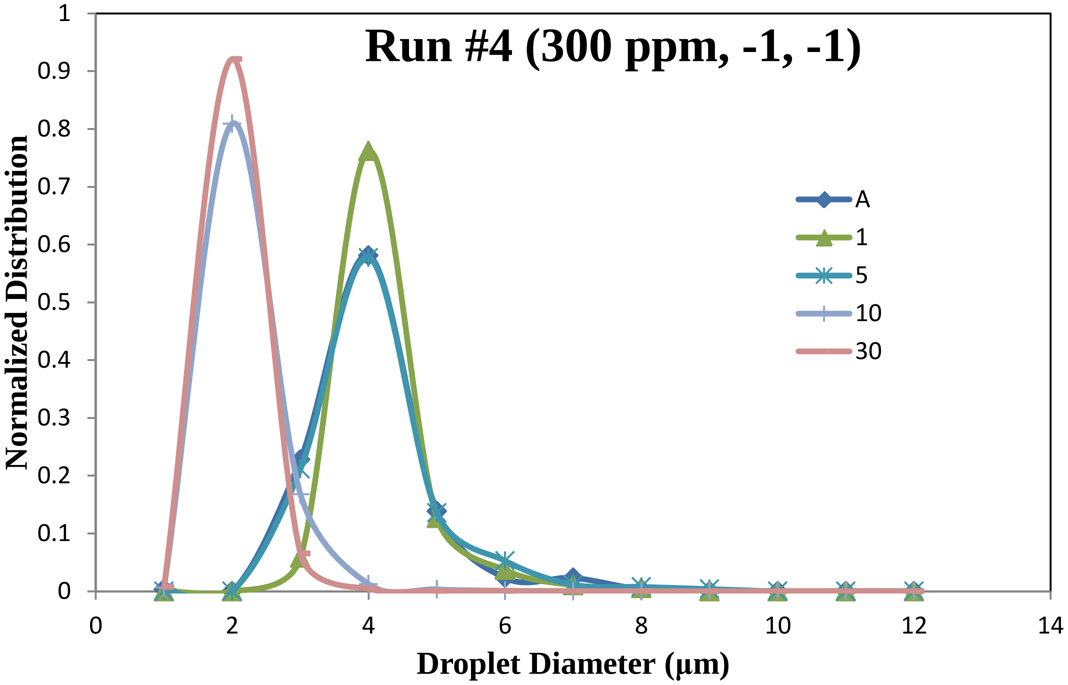

Figure 43: Droplet Size Distributions for low mixing and low injection concentration.
Variable Order: BC, J, IC

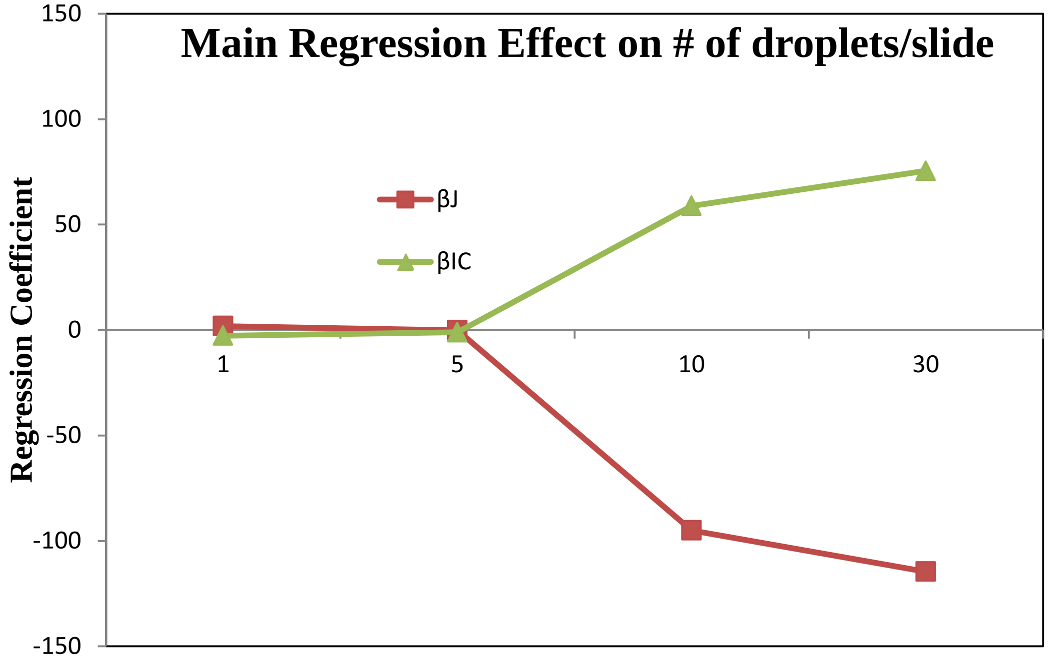

Figure 44: Main Effect Regression for Mixing Energy X_J and Injection Concentration X_{IC}

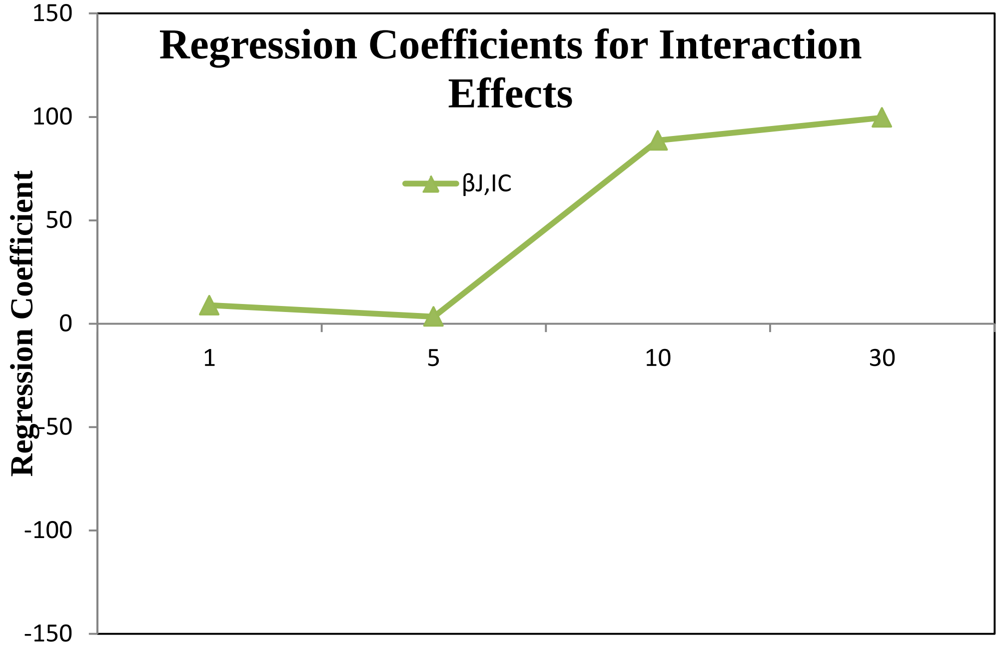

Figure 45: Interaction Effect Regression for Mixing Energy X_J and Injection Concentration X_{IC}

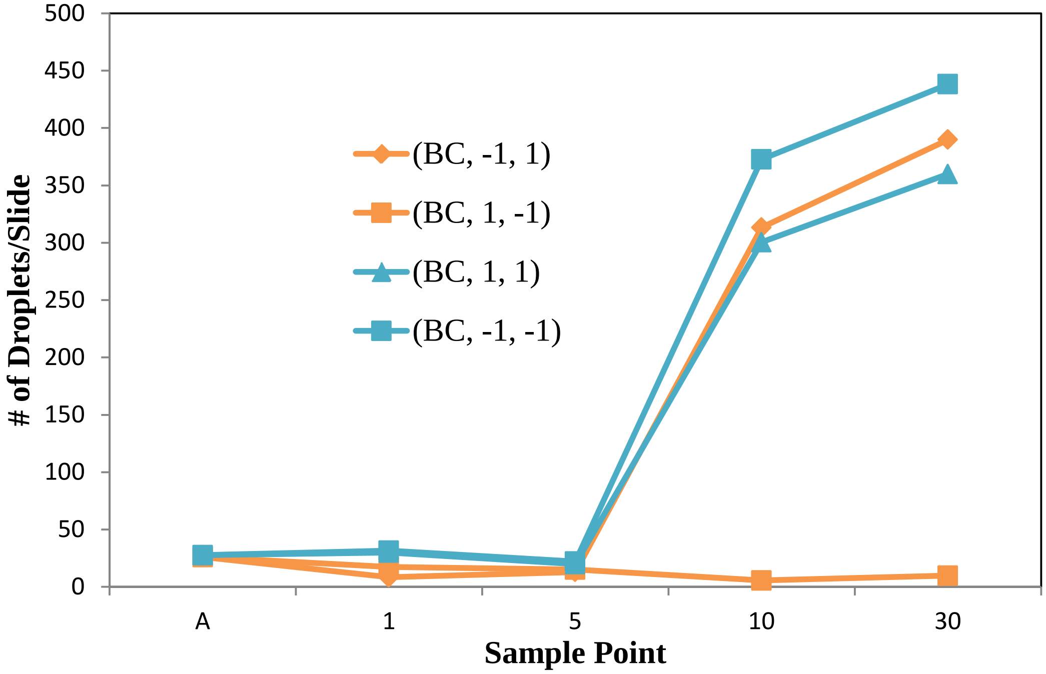

Figure 46: Number of droplets per slide. *Variable Order: BC, J, IC*

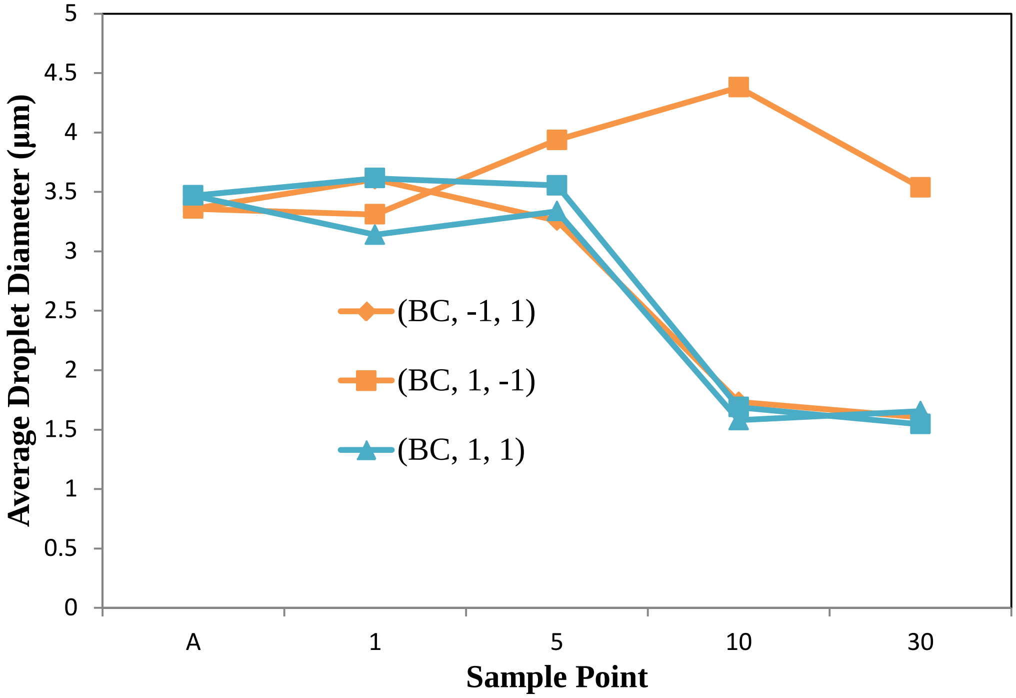

Figure 47: Average droplet diameter. *Variable Order: BC, J, IC*

4.3 Conclusions

Four experimental runs were carried out to study the effects of mixing and demulsifier injection concentration on the water droplets dynamics in bitumen clarification when demulsifier bulk concentration is set at an unusually high value. All experiments were carried out with a demulsifier bulk concentration of 300 ppm, while varying mixing and injection concentration. Overdosing effects were noticed, with some of the experiments having an average water droplet of 2 µm as opposed to the usual 4 µm obtained from Chapter 3. It was also observed that mixing had the most significant effect when it comes to the average size of the water droplets and the final # of droplets/slide. Injection concentration did not affect the results as expected from the conclusions obtained from Chapter 3. However, when good mixing is performed, injection concentration had an effect on the final # of droplets and average droplet diameter. This meant that the injection concentration had a significant effect on the process when mixing is optimized. This is similar to the conclusion obtained from Campaign 2.

It can be concluded that good mixing and a low injection concentration will be able to overcome the effect of overdosing by allowing for proper dispersion of demulsifier, preventing saturated local concentrations from occurring.

Chapter 5: Conclusions and Future Work

5.1 Conclusions

The effect of mixing and demulsifier concentration was studied in this thesis. It was discovered that the demulsifier bulk concentration and injection concentration had a strong effect on the demulsifier performance and that the effects of mixing time and mixing intensity were negligible due to the fact that their 95% confidence interval overlaps at y-axis. A low injection concentration and a high bulk concentration lead to the optimal performance of the demulsifier. Having a low injection concentration can also be linked to mixing as a low injection concentration represents a pre-mixed system of the demulsifier and a diluent. It was also discovered that the diluted bitumen system has a constant drop size distribution peak of 4 µm drops throughout the test. The time taken for a 4 µm drop to settle from the surface past the sampling point is approximately 3 minutes. However the constant drop size distribution peak throughout the experiment meant that 4 µm drops were still present even after 3 minutes. This meant that the rate of forming new 4 µm drops through coalescence was faster than the settling rate of a 4 µm drop.

When the demulsifier bulk concentration and injection concentration are at the optimal values, the effects of mixing could be observed. A high mixing energy (mixing time and mixing energy) results in better additive performance. This allows for further optimization of any process which requires the dispersion of additives. When the additive concentrations are at the right conditions, mixing is a factor which can be varied in order to optimize the process. By lowering the injection concentration of the demulsifier for the diluted bitumen clarification process, it allows for a reduction in chemical costs as well as in costs further down the process such as removal of the additives as waste.

The effect of mixing and demulsifier concentration on overdosing of systems was also studied. It was observed that when the diluted bitumen system is overdosed, the number of droplets greatly increase and the average droplet diameter greatly decreases. There was also a shift in the drop size distribution peak from 4 µm to 2 µm. These overdosing effects were neglected when the demulsifier injection concentration was at a low value and the mixing energy was at a high value. This signifies that good mixing is able to overcome the effect of overdosage.

5.2 Future Work

Future work should be done to further investigate the discoveries made in this thesis such as:

- Effects of mixing on the detailed coalescence and flocculation mechanisms.
- Shift in the drop size distribution peak at the 10 minute mark in overdosed scenarios

References

Bancroft, W.D., (1913). “Theory of Emulsification.” Journal of Physical Chemistry **17**:501-519

Bhardwaj, A. and S. Hartland (1993). "Study of demulsification of water-in-crude oil emulsion." Journal of Dispersion Science and Technology **14**(5): 541-557.

Bhardwaj, A. and S. Hartland (1994). "Dynamics of emulsification and demulsification of water in crude oil emulsions." Industrial & Engineering Chemistry Research **33**(5): 1271-1279.

Bhardwaj, A. and S. Hartland (1994). "Kinetics of coalescence of water droplets in water-in-crude oil emulsions." Journal of Dispersion Science and Technology **15**(2): 133-146.

Boxall, J.A., C.A. Koh, E.D. Sloan, A.K. Sum and D.T. Wu (2011). “Droplet Size Scaling of Water-in-Oil Emulsions under Turbulent Flow.” Langmuir **28**: 104-110

Desnoyer, C. O. Masbernat, C. Gourdon (2003). “Experimental study of drop size distributions at high phase ratio in liquid-liquid dispersions.” Chemical Engineering Science **58**: 1353-1363

Energy Resources Conservation Board (ERCB) (2008). “ST89: Alberta’s energy reserves 2007 and supply/demand outlook 2009-2017” Calgary

Everett, D.H. (1988). Basic Principles of Colloid Science. London, Royal Society of Chemistry

Feng, X., Z. Xu and J. Masliyah (2009). "Biodegradable polymer for demulsification of water-in-bitumen emulsions." Energy and Fuels **23**(1): 451-456.

Gu, G., Z. Xu, K. Nandakumar and J. H. Masliyah (2002). "Influence of water-soluble and water-insoluble natural surface active components on the stability of water-in-toluene-diluted bitumen emulsion." Fuel **81**(14): 1859-1869.

Gonzalez R., R. Woods (2001). Digitial Image Processing. Prentice Hall

Howarth, W.J. (1967). “Measurement of Coalescence Frequency in an Agitated Tank” AIChE Journal **13**(5): 1007-1013

Kim, Y. H. and D. T. Wasan (1996). "Effect of Demulsifier Partitioning on the Destabilization of Water-in-Oil Emulsions." Industrial and Engineering Chemistry Research **35**(4): 1141-1149.

Kusters, K., J. Wijers, and D. Thoenes (1996). “Aggregation kinetics of small particles in agitated vessels.” Chemical Engineering Science 52(1):107-121

Kukukova, A., J. Aubin and S. M. Kresta (2009). "A new definition of mixing and segregation: Three dimensions of a key process variable." Chemical Engineering Research and Design **87**(4): 633-647.

Laplante, P. (2011). On Mixing and Demulsifier Performance in Oil Sands Froth Treatment. Published MSc. Thesis, University of Alberta, Edmonton, Canada

Liao, Y., H.J. Subramani, E.I. Franses and O.A. Basaran (2004). “Effects of Soluble Surfactants on the Deformation and Breakup of Stretching Liquid Bridges.” Langmuir **20**: 9926-9930

Long, Y., T. Dabros and H. Hamza (2002). "Stability and settling characteristics of solvent-diluted bitumen emulsions." Fuel **81**(15): 1945-1952.

Long, Y., T. Dabros, H. Hamza (2004). “Structure of water/solids/asphaltenes aggregates and effect of mixing temperature on settling rate in solvent-diluted bitumen.” Fuel **83**: 822-832

Maaβ, S., J. Rojahn, R. Hansch, M. Kraume (2012). “Automated drop detection using image analysis for online particle size monitoring in multiphase systems.” Computers and Chemical Engineering **45**:27-37

Mason, S. L., K. May and S. Hartland (1995). "Drop size and concentration profile determination in petroleum emulsion separation." Colloids and Surfaces A: Physicochemical and Engineering Aspects **96**(1-2): 85-92.

Masliyah, J.H., Z. Xu, and Jan A. Czarnecki (2011). Handbook on Theory and Practice of Bitumen Recovery from Athabasca Oil Sands. Cochrane, Alta.: Kingsley Knowledge Pub.

Paul, E. L., V. A. Atiemo-Obeng and S. M. Kresta (2004). Handbook of Industrial Mixing : Science and Practice. Hoboken, New Jersey, John Wiley & Sons, Inc.

Peña, A. A., G. J. Hirasaki and C. A. Miller (2005). "Chemically induced destabilization of water-in-crude oil emulsions." Industrial and Engineering Chemistry Research **44**(5): 1139-1149.

Purwar, Y. (2011). Data based abnormality detection. Published MSc. Thesis, University of Alberta, Edmonton, Canada

Rosen, M.J. (2004). Surfactants and Interfacial Phenomena, Third Edition, pp 332-337. New Jersey, USA: WileyInterscience.

Walker, A., T. Dabros, J. Kan, and Y. Long (2008). “Process for Treating Heavy Oil Emulsions Using a Light Aliphatic Solvent-naphtha Mixture.” Suncor Energy, assignee. Patent 2435113.

Yan, N., M. R. Gray and J. H. Masliyah (2001). "On water-in-oil emulsions stabilized by fine solids." Colloids and Surfaces A: Physicochemical and Engineering Aspects **193**(1-3): 97-107.

Yeung, A., T. Dabros and J. Czarnecki (1999). "On the interfacial properties of micrometre-sized water droplets in crude oil." Proceedings of the Royal Society A: Mathematical, Physical and Engineering Sciences **455**(1990): 3709-3723.

Zhang, L.Y., Z. Xu, J.H. Masliyah (2003). “Langmuir and Langmuir-Blodgett Flims of Mixed Asphaltenes and a Demulsifier.” Langmuir **19**: 9740-9741

Zhou, G. and S. M. Kresta (1996). "Distribution of energy between convective and turbulent flow for three frequently used impellers." AIChE J. **74A**: 2476-2490.

Zhou, G. and S. M. Kresta (1998). "Evolution of drop size distribution in liquid-liquid dispersions for various impellers." Chem. Eng. Sci. **53**: 2099-2113.

Appendix A: Step by step procedure of Water Droplet Detection Image Analysis Protocol

This appendix outlines the step by step procedure for the water droplet detection image analysis protocol in Adobe Photoshop, Fovea Pro, and MATLAB.

6) Loads the colored RGB (Red, Green and Blue channel) image and converts it into a gray-scale image. This is done in Adobe Photoshop. The image is opened in Adobe Photoshop and the 'Image > Mode' was set to Lab Color and channels 'a' and 'Alpha 2' were deleted accordingly. The 'Image > Mode' was then converted to a gray-scale channel. This allows for the preservation of the color information of the image, processing only the brightness and luminance values of the image. This corresponds to Figure 6 (a)-(b).

7) A Fovea Pro 4.0 Filter Plug-in for Adobe Photoshop is applied to the gray-scale image in the following step. This is done by using the filter 'IP* Adjust > Auto-Level'. This enhances the contrast of the gray-scale image by using histogram equalization to 'level' the image. Figure 7 shows the effect of this process, corresponding to Figure 6 (b) – (c). This step corrects for exposure issues that may be present on a poor sample. Exposure issues are due to a difference in brightness values along certain parts of the image, producing peaks in the image brightness histogram. The different amplitudes of brightness in the image would result in inaccuracies when performing other image analysis functions, such as Forward Fourier Transform. This filter works by reassigning the brightness levels of the pixels, ensuring that the

pixels are as evenly spread out as possible at each possible brightness value, without altering the image too dramatically. This “levels” out the image brightness histogram distribution of the values as best as possible by attempting to fit a linear cumulative plot.

The micrograph in Figure 6 & Figure 7 *did not have any exposure issues and the effect of this step may not be fully appreciated.*

See Histogram Equalization (Section 2.3.1) for more information and examples.

8) After the image has been corrected for exposure differences, another Fovea Pro 4.0 Filter, ‘IP* Adjust > Homomorphic Range Compression’, is applied to the image. This filter, which performs using Fourier Transform, uses the magnitude of the power spectrum to design a custom filter for each individual image being processed. This filter separates the illumination and reflectance components in the image. It is used to remove periodic noise which is caused by environmental interferences such as illumination. This is done by suppressing the variation in illumination (that is suppressing gradual changes in brightness values) and increasing the variation in reflectance (emphasizing abrupt changes in brightness values). This reduces the overall brightness in the image but increases the contrast, sharpening the image as a result. The change in contrast affects the image brightness histogram and prepares the image for the next step in the protocol. This filter attempts to normalize the brightness values. Figure 8 shows the effect of this process on the brightness histogram, corresponding to Figure 6 (c) – (d).

See Fourier Transform (Section 2.3.2) for more information

9) The final step in the pre-processing stage is the conversion of the gray-scale image into a binary image. This corresponds to Figure 6 (d)–(e). A Fovea Pro 4.0 Filter, ‘IP*Threshold > Bi-level Thresholding’, is used on the image. This filter works by defining a range of brightness values and pixels with brightness values within this range will be assigned as the foreground of the image and the pixels with brightness values outside this range will be assigned to be the background of the image. This process, known as Thresholding, produces a binary image, using white as the background color and black as the foreground color. The sensitivity of this filter (range of brightness) is the key variable that limits batch processing and could be either manually adjusted in the interface menu of the Bi-Level Thresholding Filter or automatically adjusted by selecting one of the pre-programed algorithms that determines the ranges. Different micrographs will respond differently to different sensitivity settings. As a result, Steps 1 – 3 are important in standardizing the micrographs to have similar image brightness histograms so that automated batch processing can be done at this step, without having to vary the brightness range for each individual image, be it manually or using one of the pre-programed algorithms.

   See Bi-level Thresholding (Section 2.3.3) for more information

10) The final piece to this image analysis protocol is the Circle Detection Algorithm (Purwar, 2011). It is based on the image analysis tool called Hough Transform and operates in Hough Space. This algorithm identifies circles

based on a set of parameters set by the operator, such as the radii range of the circles, the sensitivity of the algorithm (% of how well the area of the object matches the area of a circle of similar size) and the presence of concentric circles. The algorithm works by fitting objects into a circular area and shrinking the area. If the object fits within a certain percentage of the circle's area (i.e. 80%), it is classified as a circle and its radius and the x & y coordinates of the circle origin are recorded down into an array. This percentage can be defined by the operator and can also be referred to as the sensitivity of the algorithm.

See <u>Hough Transform</u> (Section 2.3.4) for more information

Appendix B: Sample Run of Benchmark Test

The following four images demonstrate how the benchmark tests were run. These four images correspond to benchmark test run #5. Figure B1 represents the original micrographs taken at 400x magnification. Figure B2 represents the same micrograph after the pre-processing stage. Figure B3 represents the micrograph after the circle detection algorithm has been performed. Figure B4 shows the manual size measurement and droplet count performed on the micrograph.

The results obtained from this run was recorded and repeated with four other different images to obtain an average accuracy.

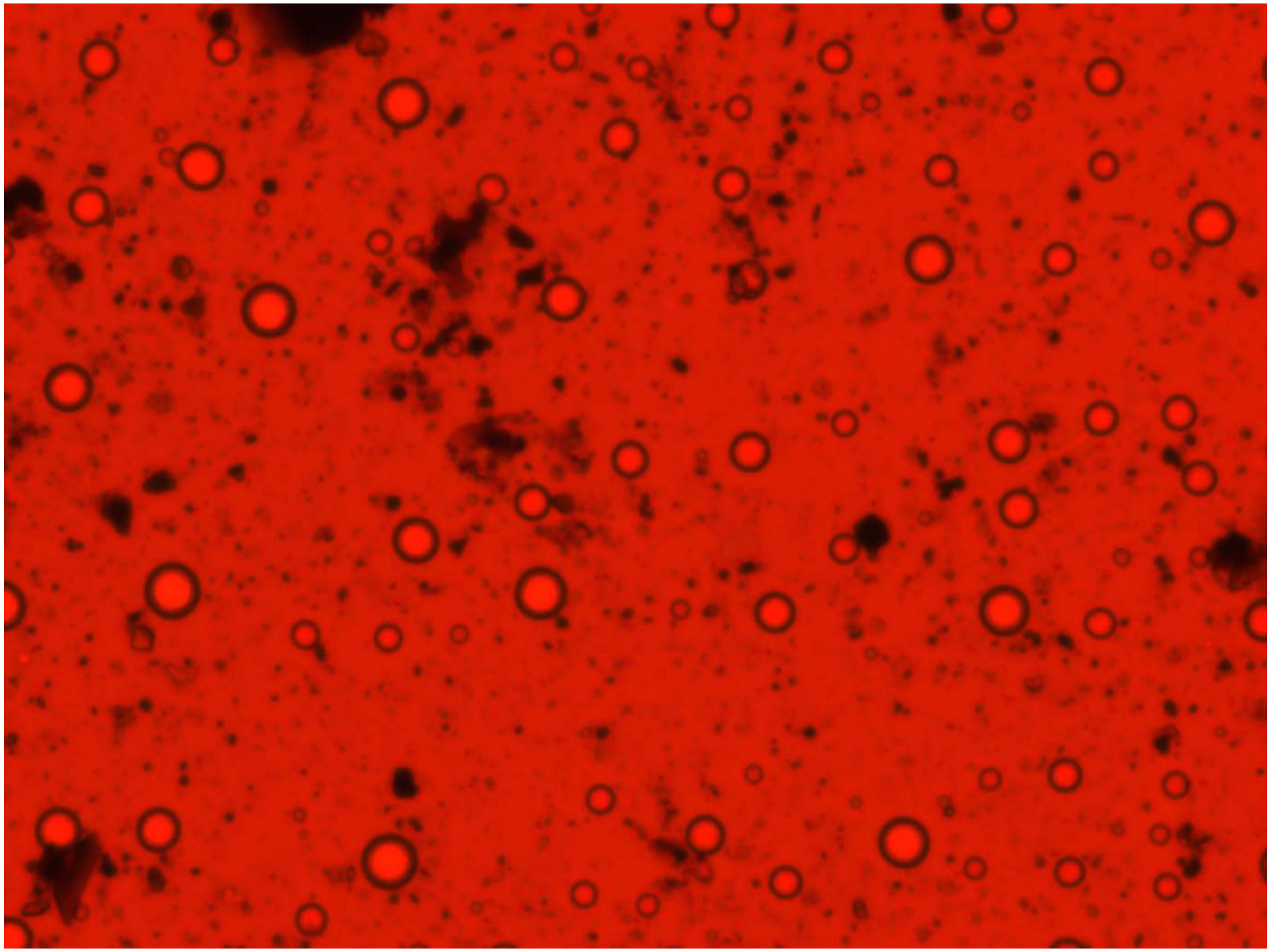

Figure B1: Original Micrograph

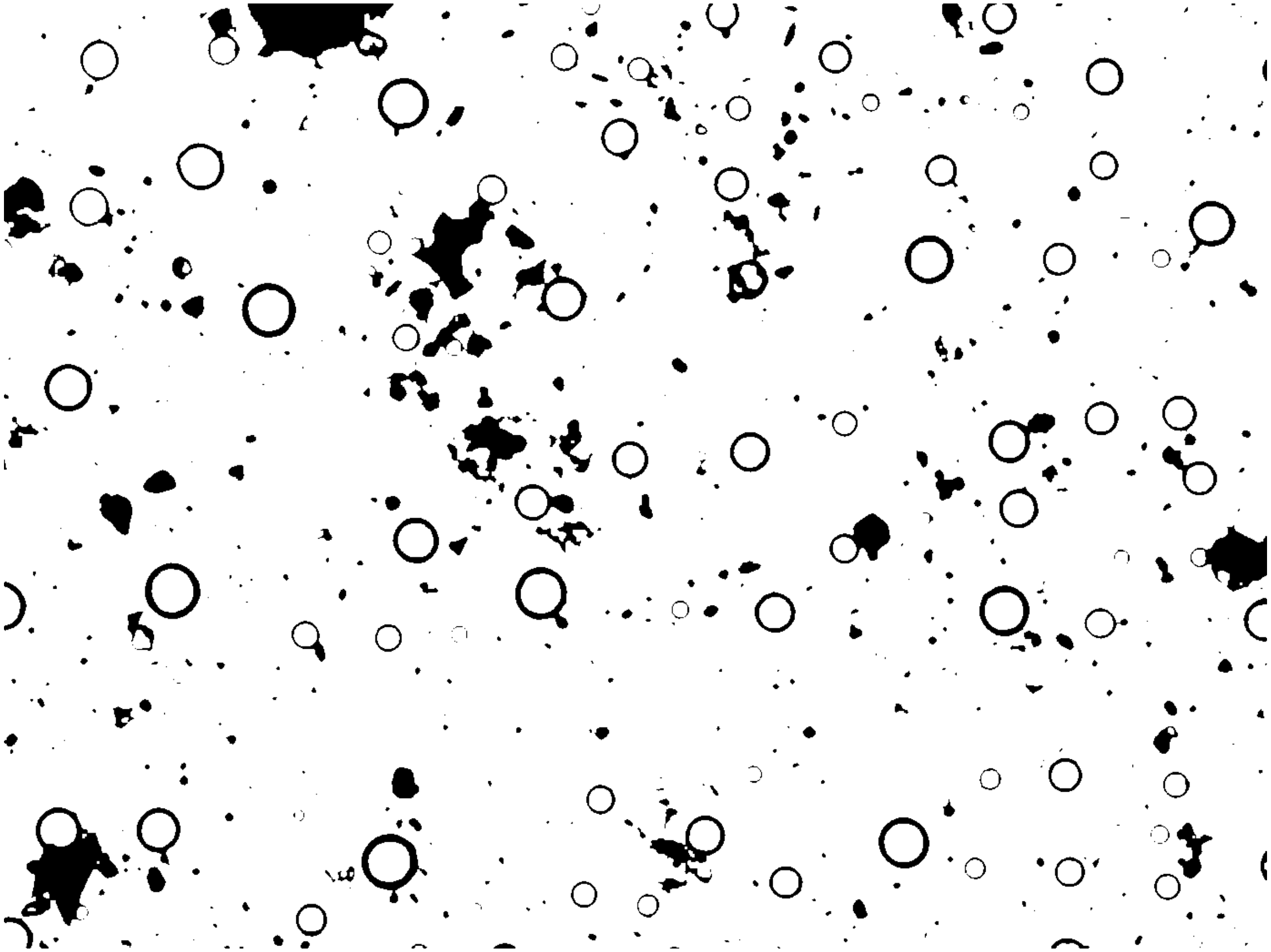

Figure B2: After the Pre-Processing Stage

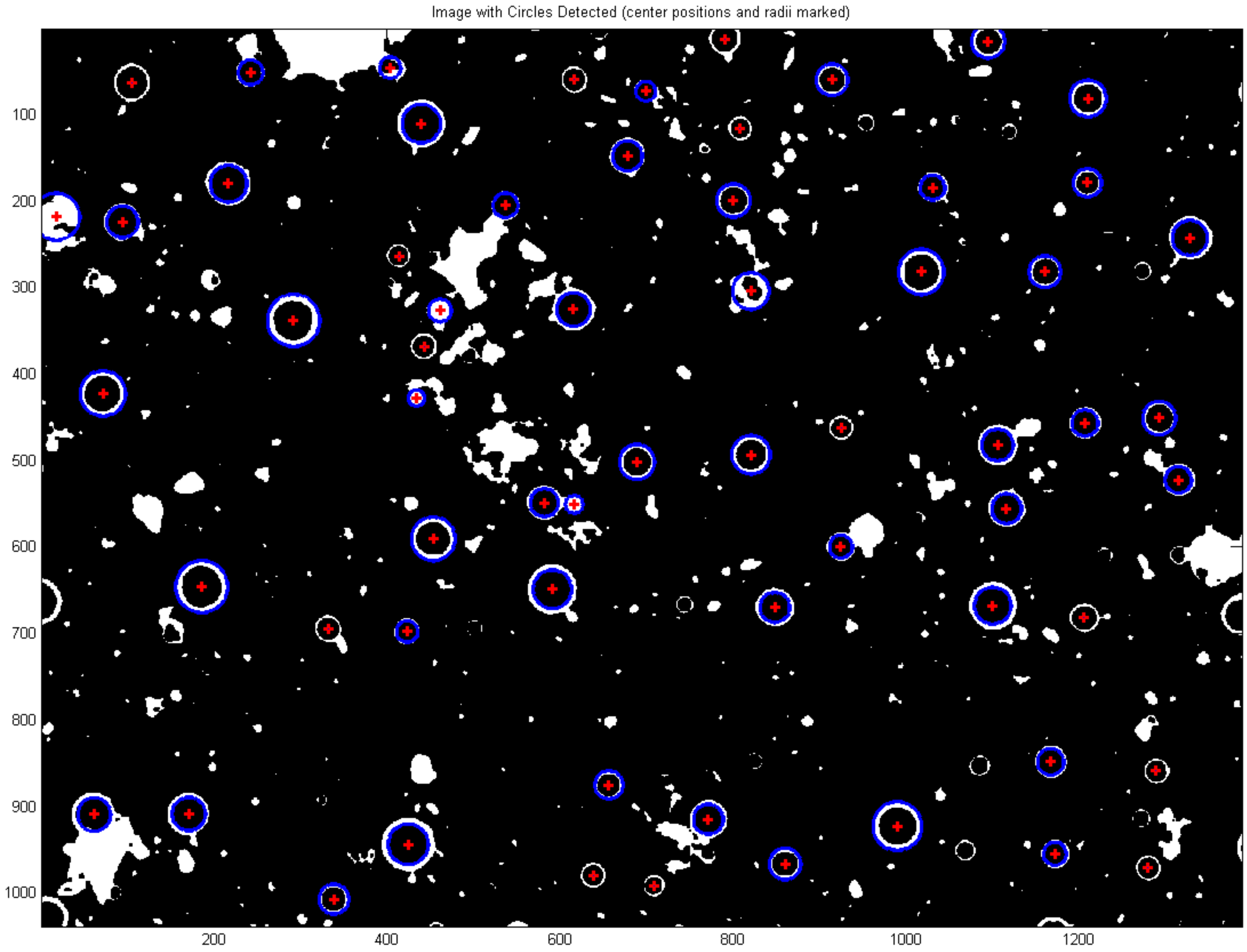

Figure B3: Circle Detection

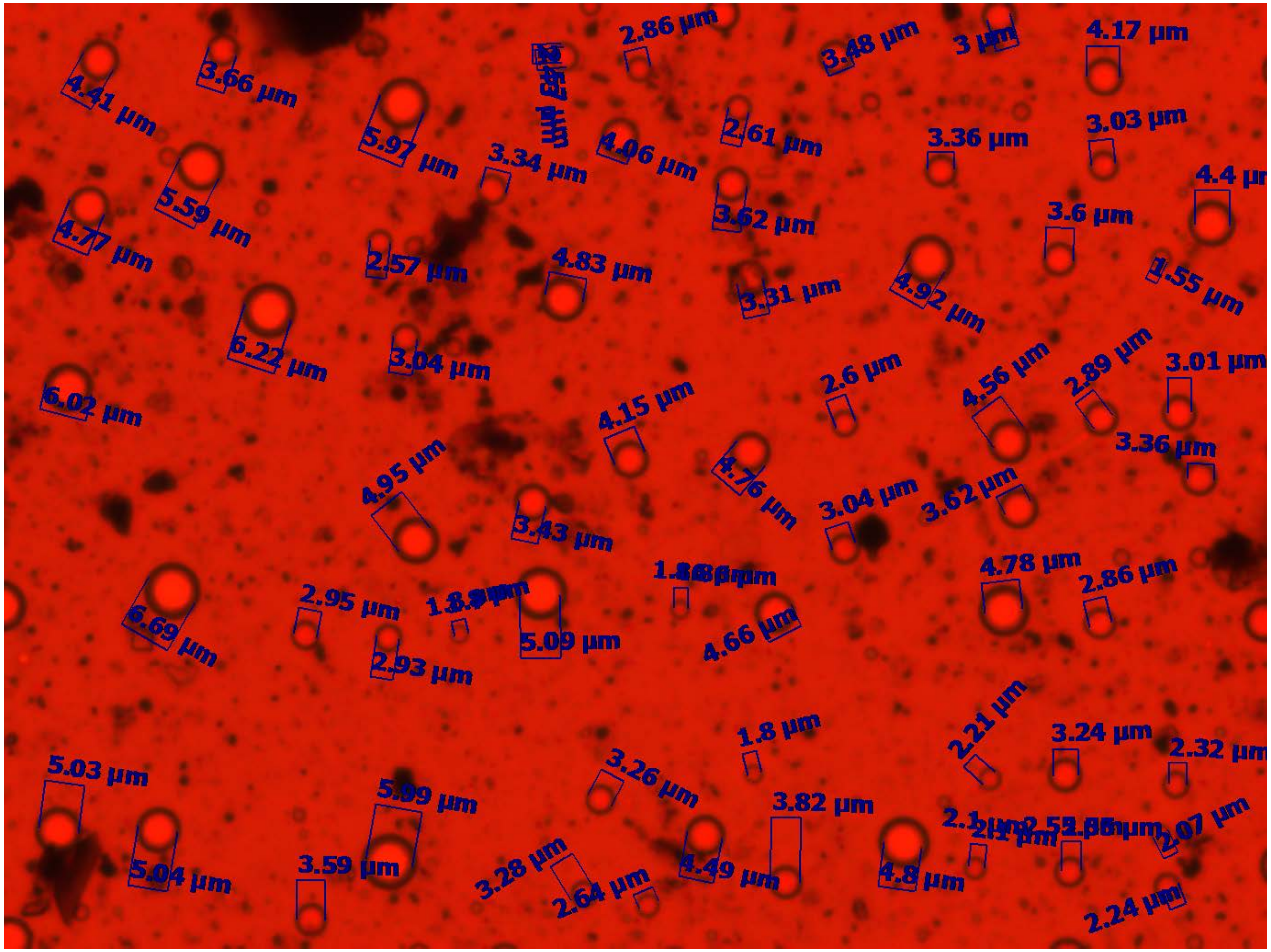

Figure B4: Image with manually measured drop size

Appendix C: Axioscope Operating Procedure

This document describes the operating procedure for the Axioscope microscope used in this study.

Microscope calibration (Video Tutorial)

1. Turn on the microscope
2. Check the field diaphragm
    a. Set microscope lenses to 10x
    b. Close the field diaphragm to the smallest diameter
    c. Center the diaphragm
    d. Focus the diaphragm by turning the focus knob (want to make the diaphragm take the shape of a red hexagon)
3. Adjust aperture to cover 70% of the area (differs with different magnifications)
    a. Markings are present on the microscope aperture for easy calibration
4. Open field diaphragm to desired size

Microscope startup

1. Open the live feed (F3)
2. Perform white balance with a white piece of paper on the sampling platform
3. Perform shading correction with an empty microscope slide

Microscope Care

Optimal size for microscope slide covers: 1.5 thickness

Check refractive index for immersion oil when purchasing new immersion oil

Clean microscope lenses with 70% Ethanol in water